

https://dspace.org/

57Fe Mossbauer investigations in GaAs and GaP following implantation of 57Mn*

Masenda, Hilary

2010-07-30T10:20:48Z
http://hdl.handle.net/10539/8331

Downloaded from a DSpace repository. https://dspace.org/

^{57}Fe Mössbauer investigations in GaAs and GaP following implantation of ^{57}Mn*

Hilary Masenda

A dissertation submitted to the Faculty of Science, University of the Witwatersrand, Johannesburg, in fulfillment of the academic requirements for the degree of Master of Science.

Johannesburg

March 2010

BLANK PAGE

ABSTRACT

The incorporation of extrinsic defects in semiconductors by ion implantation and appropriate annealing gives rise to instabilities that profoundly affect their electronic and optical properties. Consequently, the knowledge of site location and hence the chemical nature of these defects is vital for the understanding of new properties in doped compound semiconductors. These properties are important for possible applications in optoelectronic and high-frequency devices such as light emitting diodes (LEDs), laser diodes, and monolithic microwave integrated circuits (MMICs) and high power field effect transistors (FETs) for satellite and terrestrial communication.

Mössbauer studies to investigate site location and nature of Fe complexes formed in GaAs and GaP single crystals following ^{57}Mn* implantation at temperatures 77 – 700 K were carried out at the ISOLDE facility, CERN, Switzerland. The set of temperature dependent spectra for each sample was analyzed with a simultaneous fitting routine. Best fits to the data required four components, an asymmetric doublet due to radiation damage attributed to Fe atoms in small amorphous pockets, two single lines, one assigned to Fe on substitutional Ga sites and the other to Fe in interstitial sites, and a low intensity symmetric doublet assigned to impurity-vacancy complexes.

The isomer shift and quadrupole splitting values show the trivalent state of iron ($^{57}Fe^{3+}$), with a $3d^5$ electronic configuration, on substitutional Ga sites in cubic environments and, near $3d^5$ and $3d^6$ electronic configurations in distorted environments and interstitial sites, respectively. The impurity-vacancy complex is tentatively assigned to $3d^5$ configuration because of its complex nature.

The observed variations in the hyperfine parameters of the damage site in GaAs and GaP at temperatures above 400 K can be attributed to the changes in environment in the neighborhood of the Mössbauer atom and possibly in the Fe-defect bonding mechanism. Different annealing stages of the radiation damage in the two substrates were evident, with more pronounced healing observed in

GaAs (350 – 550 K) as compared to GaP (465 – 600 K). This is attributed to Fe forming stronger bonds with P than As. This observation is further supported by the higher Debye temperatures that were extracted for the different components in GaP relative to GaAs.

In the III-V semiconductors, Fe atoms on substitutional III sites are known to be deep acceptors and to have a tendency to interfere mainly with the optical functionality of the semiconductors. In this regard, recommendations to investigate optical properties and electrical conductivity of these materials are discussed.

DECLARATION

The measurements described in this dissertation were carried out at the Isotope Separator On-line DEvice facility, ISOLDE at CERN, Geneva, Switzerland. The experiments were conducted in collaboration with Aarhus University (Denmark), University of the Witwatersrand, University of KwaZulu-Natal, Laboratorio MDM-INFM (Italy), and the Helmholtz Zentrum Berlin (Germany), formerly known as the Hahn-Meitner Institute.

The data analysis and understanding of results is my original work and was carried under the guidance of Dr D. Naidoo (supervisor) and Professor K. Bharuth-Ram (co-supervisor).

The work of other scientists is duly acknowledged when they are used in this dissertation.

I declare that this dissertation has not been submitted before for any degree or diploma examination in any other tertiary institution.



Signed:_____

Hilary Masenda

March 31, 2010

In memory of my Parents:

Michael Masenda & Evelyn Masenda

1942-1993 *1947-2005*

I'm forever grateful,……Ndinotenda!

ACKNOWLEDGEMENTS

The success of any project is a result of many people who contribute in various ways. I wish to take this opportunity to acknowledge a number of people who have greatly contributed to the final form of this dissertation.

I am greatly indebted to my supervisor, Dr Deena Naidoo for bringing me into this international collaboration, for guiding my dissertation work, for taking time to read through the drafts of this dissertation with a critical eye, for his comments, suggestions, encouragements, and for time consuming consultations in spite of his awesome commitments. Thank you!

I wish to express my sincere thanks to my co-supervisor Professor Krish Bharuth-Ram for his mentorship and correspondence during my studies. You have done a commendable job that is worth of mention and recognition.

I am grateful to Professors H. P. Gunnlaugsson and G. Weyer (Aarhus University, Denmark) and the ^{57}Mn* Mössbauer collaboration for their assistance and advice during the experimental work. Many thanks to you all for stimulating discussions.

A special thanks to Dr D. Wamwangi for proof reading the draft version of my dissertation and for his valuable suggestions. Thanks to my fellow students and friends: Wisdom, Kuda, Mehluli, Pius, Leo, Chris, Julius, Lawrence, Cindy, Desmond, Clara, Philemon, Patrick, Stewart, Tino, and Noma and my family for all the support and encouragement during my studies.

I am grateful for the financial support from the National Research Foundation (NRF) through the grant-linked bursary scheme and the SA-CERN program.

I would like to thank all the staff in the School of Physics who have contributed to making my studies a success.

Above all, I therefore give credit to whom it is due. To one who never criticises but often suggests a different way of doing things; who makes a way where there seems no way. To God be Glory and Honour. [1 Chronicles 29:11]

NOMENCLATURE

ϕ	Dose, Fluence, or number of ions per unit area
$(V_{ZZ})_{Lat}$	Lattice contributions to the EFG
$(V_{ZZ})_{Val}$	Valence electron contributions to the EFG
$\langle x^2 \rangle$	Mean square displacement
$\lvert\psi(0)\rvert^2$	Probability density
ΔE_Q	Quadrupole splitting
$\Delta E_{Q,O}$	Quadrupole splitting at 0 K (fitting parameter)
ΔR_p	Straggle
A	Beam area
ADC	Analogue to Digital Converter
A_i	Area of a component or line i in fitted spectrum
A_o	Initial spectrum area
As	Arsenic
$\boldsymbol{B}_D$	Dipole field
$\boldsymbol{B}_{eff}$	Effective Magnetic field
$\boldsymbol{B}_F$	Fermi contact field
$\boldsymbol{B}_{hf}$	Hyperfine Magnetic field
$\boldsymbol{B}_L$	Orbital field
$\boldsymbol{B}_{loc}$	Local Magnetic field
C	Calibration constant
CB	Conduction Band
CEMS	Conversion electron Mössbauer spectroscopy
CERN	The European Organization for Nuclear Research
CHA	Channel advance
CMS	Conventional Mössbauer spectroscopy
Co	Cobalt
CRO	Cathode Ray Oscilloscope
dE	Energy lost by an ion by traversing in matter
DLTS	Deep Level Transient Spectroscopy
$\boldsymbol{D}_M$	Demagnetization
dx	Distanced traveled
E_A	Energy transition in absorber
EC	Emission Channeling

E_d	Threshold displacement energy
EFG	Electric Field Gradient
E_O	Transition Energy
EPR	Electron Paramagnetic Resonance
E_R	Recoil Energy
E_S	Energy transition in source
ESR	Electron Spin Resonance
E_γ	Gamma-ray energy
f	Recoil-free fraction, Debye-Waller factor or Mössbauer-Lamb factor
Fe	Iron
Fe_D	Iron in a damage site
Fe_I	Iron in an interstitial site
Fe_N	Iron in a substitutional- or impurity-vacancy complex
Fe_S	Iron in a substitutional site
FET	Field Effect Transistor
FG	Function Generator
FWHM	Full Width of spectral line at Half Maximum
GaAs	Gallium Arsenide
GaP	Gallium Phosphide
Ge	Germanium
GLM	General Low Mass
g_N	Nuclear Landé factor
HV	High Voltage
I	Nuclear spin quantum number
I_B	Beam current
IBMS	In-Beam Mössbauer Spectroscopy
IC	Integrated Circuit
In	Indium
InAs	Indium Arsenide
InP	Indium Phosphide
InSb	Indium Antimonide
ISOLDE	Isotope Separator On-Line Device
$\boldsymbol{k}$	Wave vector
K	Kelvin
k_B	Boltzmann constant

LED	Light Emitting Diode
LSS	Lindhard-Scharff-Schiott
m	Nuclear mass
$\boldsymbol{M}$	Lattice mass
MAS	Mössbauer Absorption Spectroscopy
MBE	Molecular Beam Epitaxy
MCA	Multichannel analyzer
MDU	Mössbauer Drive Unit
MEDC	Mössbauer Effect Data Center
MES	Mössbauer Emission spectroscopy
m_{I}	Nuclear magnetic spin quantum number
$\boldsymbol{M}_{\mathrm{m}}$	Magnetization
MMIC	Monolithic Microwave Integrated Circuit
Mn*	Radioactive Manganese
$\boldsymbol{N}$	Neutron number
N	Number of target atoms per unit volume
P	Phosphorus
PAC	Perturbed Angular Correlation
p_i	Site population of line i
PL	Photoluminescence
PPAC	Parallel plate avalanche counter
Q	Electric quadrupole moment
$\boldsymbol{R}$	Nuclear radius
R	Range
R_{p}	Projected range
Sb	Antimonide
SCA	Single channel analyzer
S_e	Electronic Stopping power
Si	Silicon
SiGe	Silicon germanium
S_n	Nuclear Stopping Power
Sn	Tin
t	implantation time
T	Temperature
$t_{1/2}$	Half-life of radioactive nucleus

T_K	A constant - Fitting parameter measured in Kelvin
UC_2	Uranium Carbide
UHV	Ultra High Vacuum
VB	Valence Band
V_{ZZ}	Principal axis component of the EFG
z	Zero velocity
Z	Proton or Atomic number
Γ	Natural linewidth
δ_C	Center shift
δ_{IS}	Isomer shift
δ_{SOD}	Second-order Doppler shift
η	Asymmetry parameter
θ_D	Debye temperature
θ_E	Einstein temperature
μ	Magnetic dipole moment
ρ	Electron density
τ_N	Mean lifetime of a nuclear level
χ^2	Chi-squared value
ω_D	Debye frequency
ω_E	Einstein frequency

TABLE OF CONTENTS

ABSTRACT ..... **i**

DECLARATION ..... **iii**

ACKNOWLEDGEMENTS ..... **v**

NOMENCLATURE ..... **vi**

TABLE OF CONTENTS ..... **x**

Introduction **1**

1.1 Point defects 3

1.2 Literature Review 5

1.2.1 Lattice site location 6

1.2.2 Electronic configuration – Charge states 8

1.3 Objectives of this study 9

1.4 Dissertation Outline 10

Mössbauer Spectroscopy **11**

2.1 Introduction 11

2.2 Mössbauer Effect: Resonant emission and absorption 11

2.3 Recoil-free fraction and Debye Temperature 13

2.4 Experimental Resonance Condition 15

2.4.1 Natural line width 16

2.4.2 Transition Energy 18

2.5 Factors influencing the Mössbauer Effect 18

2.5.1 Electric Monopole Interaction: Isomer shift 18

2.5.1.1 Observing resonance 19

2.5.1.2 Shielding effect 20

2.5.1.3 Second-order Doppler Shift 20

2.5.1.4 Isomer shift and *s*-electron density 21

2.5.2 Electric Quadrupole Interaction: Quadrupole Splitting 23

2.5.2.1 Sources of the Electric Field Gradient 25

2.5.2.2 Temperature dependence of the quadrupole splitting 25
2.5.3 Magnetic Dipole Interaction: Magnetic Splitting..... 26
2.5.3.1 Relative Line Intensities..... 27
2.5.3.2 Effective Magnetic Field..... 27
2.5.4 Combined magnetic and quadrupole interactions 29

Experimental Details.....30
3.1 Introduction..... 30
3.2 Principles of Ion Implantation..... 30
3.2.1 Ion stopping mechanisms..... 31
3.2.1.1 Electronic Stopping..... 31
3.2.1.2 Nuclear Stopping..... 31
3.2.2 Total stopping power..... 32
3.2.3 Range and Distribution Profile..... 33
3.2.4 SRIM2008 Simulation 35
3.2.5 Implantation parameters..... 36
3.2.5.1 Ion energy..... 37
3.2.5.2 Ion mass..... 37
3.2.5.3 Implantation temperature 37
3.2.5.4 Ion flux 37
3.2.5.5 Ion dose 38
3.2.6 Radiation damage..... 38
3.2.7 Annealing 39
3.3 Mössbauer emission spectroscopy at ISOLDE 40
3.3.1 Beam production at ISOLDE 40
3.3.2 Experimental set-up 41
3.3.3 Samples and measurements..... 45
3.3.4 The Mössbauer Spectrum..... 46
3.3.5 Advantages of $^{57}Mn^{*}$ Mössbauer Emission Spectroscopy (MES) ... 48
3.4 Calibration of Mössbauer Spectra..... 49
3.5 Data analysis 50

Results and Discussion 52

4.1 Data analysis and interpretation of Fe in GaAs 52

4.1.1 Assignments of fitted components in GaAs. 55

4.1.2 Debye Temperatures of lattice sites in GaAs 56

4.1.3 Annealing Behavior 59

4.1.4 Summary of results for GaAs 60

4.2 Data analysis and interpretation of Fe in GaP 61

4.2.1 Discussion of hyperfine parameters 63

4.2.2 Debye Temperatures of the lattice sites in GaP 65

4.2.3 Annealing Behavior in GaP 66

4.2.4 Summary of results for GaP 67

4.3 Comparison of results obtained for GaAs and GaP 68

4.3.1 Comparison of annealing behavior in GaAs and GaP 70

4.3.2 Isomer shift variation of Fe_D and Fe_S with bond length in GaAs and GaP 71

4.4 Discussion on 'charge states' 72

4.5 Comparison of $^{57}Mn^*$ and ^{119m}Sn, $^{119}In^+$ and $^{119}Sb^+$ implantations in GaP and GaAs 74

Conclusions and Recommendations 76

5.1 Recommendations 78

Appendix A: Summary of Fitting Models Applied 80

Appendix B: Fitting using Vinda 81

B.1 Single Spectrum Fitting 81

B.2 Simultaneous Fitting 82

B.3 Error analysis 84

REFERENCES 86

LIST OF FIGURES

Figure 1.1: Comparison between the valence band, conduction band and energy gap in insulators, semiconductors and metals. The color coding indicates the occupancy of the band. 2

Figure 1.2: A schematic diagram showing different types of point defects. 3

Figure 1.3: Zinc-blende structure of cubic III-V semiconductors. 5

Figure 2.1: Nuclear recoil after gamma emission. 11

Figure 2.2: Non-resonant absorption of γ radiation. 12

Figure 2.3: Resonant emission and absorption of γ radiation. 12

Figure 2.4: Intensity I(E) as a function of transition energy E. 17

Figure 2.5: Effect of mean lifetime on resonance. 17

Figure 2.6: Effects of electric monopole interaction: Isomer shift. 19

Figure 2.7: Effects of the electric quadrupole interaction: quadrupole splitting. 23

Figure 2.8: Effects of magnetic dipole interaction: magnetic splitting. 26

Figure 3.1: Electronic stopping mechanism, due to (a) inelastic collision and (b) drag force from the electrons. 31

Figure 3.2: Nuclear stopping mechanism. 32

Figure 3.3: Theoretical estimates of nuclear stopping power (S_n) and electronic stopping power (S_e) variation as a function of ion energy. 33

Figure 3.4: Ion depth and distribution profiles. 34

Figure 3.5: Ion ranges distribution profile for 60 keV ^{57}Mn* implanted at an angle of 60^o into (a) GaAs and (b) GaP. The sample-beam experimental arrangement is depicted below the graphs. 35

Figure 3.6: Damage profiles for 60 keV ^{57}Mn* implanted at an angle of 60^o into (a) GaAs and (b) GaP. 36

Figure 3.7: The ISOLDE Facility layout. 40

Figure 3.8: Beam production at ISOLDE. 41

Figure 3.9: (a) Single sample holder for low temperature measurements and (b) Four position sample holder equipped with annealing system for high temperature measurements. 42

Figure 3.10: Experimental set-up for Mössbauer Spectroscopy at ISOLDE. 43
Figure 3.11: Schematic diagram for experimental set-up and electronics..... 44
Figure 3.12: The ^{57}Mn* Decay scheme. 45
Figure 3.13: Development of a Mössbauer emission spectrum..... 46
Figure 3.14: A typical Mössbauer emission spectrum fitted with 3 components for the Mössbauer nucleus in different lattice locations..... 47
Figure 3.15: Source velocity as a function of channel number. 49
Figure 3.16: Unfolded spectrum of α-Fe. 49
Figure 3.17: Folded spectrum of α-Fe. 50
Figure 4.1: ^{57}Fe Mössbauer spectra obtained after ^{57}Mn* implantation into GaAs single crystal held at the temperatures indicated..... 53
Figure 4.2: Temperature dependence of isomer shifts observed in Mössbauer spectra for GaAs after ^{57}Mn* implantation, where the solid lines represent the calculated values and symbols represent the results extracted from the fits to the spectra. 58
Figure 4.3: Temperature dependence of the quadrupole splitting observed in the Mössbauer spectra for GaAs after ^{57}Mn* implantation, where the solid lines represent the calculated values and symbols represent the results extracted from the fits to the spectra..... 58
Figure 4.4: Areal fractions of components as a function of temperature, observed in the Mössbauer spectra for GaAs after ^{57}Mn* implantation..... 59
Figure 4.5: ^{57}Fe Mössbauer spectra obtained after ^{57}Mn* implantation into GaP held at the temperatures indicated. 62
Figure 4.6: Temperature dependence of isomer shifts observed in Mössbauer spectra for GaP after ^{57}Mn* implantation, where the solid lines represent the calculated values and symbols represent the results extracted from the fits to the spectra..... 64
Figure 4.7: Temperature dependence of the quadrupole splitting observed in the Mössbauer spectra for GaP after ^{57}Mn* implantation, where

the solid lines represent the calculated values and symbols represent the results extracted from the fits to the spectra. 65
Figure 4.8: Areal fractions of components as a function of temperature, observed in the Mössbauer spectra for GaP after ^{57}Mn* implantation. 66
Figure 4.9: Low and high temperature behavior of the quadrupole splitting for Fe_D in GaAs, where symbols represent the fitted data. 69
Figure 4.10: Low and high temperature behavior of the quadrupole splitting for Fe_D in GaP, where symbols represent the fitted data. 69
Figure 4.11: Comparison of areal fractions of the various components as a function of temperature between GaP and GaAs. 70
Figure 4.12: Isomer shifts of Fe_S and Fe_D in GaP and GaAs as a function of bond length. A comparison is made with other semiconductors. ... 71
Figure 4.13: Comparison between the extracted hyperfine parameters for Fe in GaAs and GaP with values from the Mössbauer Effect Data Center. 73
Figure 5.1: Vacancy in zinc-blende lattice. (a) Four bonds are broken in order to form a vacancy. (b) resulting dangling bond. 76
Figure 5.2: Difference between shallow and deep defects. 78
Figure B1: Dialog box for the solver parameters. 81
Figure B2: Dialog box for solver results. 82
Figure B3: Spectrum sheet after fitting. 82
Figure B4: Typical Prog sheet for simultaneous fitting. 83
Figure B5: Built-in sod function used for calculating the isomer shift. 84
Figure B6: Error Analysis dialog box. 85
Figure B7: Typical Error Analysis worksheet. 85

LIST OF TABLES

Table 1.1: Isomer shifts for Sn on III and V sites in semiconductors. 7
Table 1.2: Debye temperature for Sn on III and V site in In compound. 7
Table 1.3: Debye temperature for Sn on III and V site in Ga compound..... 7
Table 2.1: Angular distribution of the relative intensities for the six allowed transitions in ^{57}Fe. 27
Table 3.1: Projected range and straggle values for ^{57}Mn* implanted in GaAs and GaP. 36
Table 4.1: Hyperfine parameters obtained at room temperature for GaAs. 54
Table 4.2: Hyperfine parameters obtained at room temperature for diamond, Si and Ge. 54
Table 4.3: Summary of the fitting model. 57
Table 4.4: Hyperfine parameters obtained at room temperature for GaP. 63
Table 4.5: Fitting parameters for low and high temperature quadrupole splitting behavior in GaAs and GaP. 70
Table 4.6: Hyperfine parameters for GaAs and GaP at room temperature. 72
Table 4.7: Isomer shift values of different components for various Mössbauer probes in GaP. 74
Table 4.8: Isomer shift values of different components for various Mössbauer probes in GaAs. 74

Chapter 1

Introduction

The inter-atomic bonding mechanism and hence the atomic arrangement that arises from valence electrons influence the properties of materials, such as their electrical conductivity, optical properties, elasticity, hardness, and magnetic properties. Materials with a periodic repetition of their atomic structure are said to be *crystalline* materials, and, on the basis of their electrical and optical properties, they can be classified into three categories: metals, semiconductors and insulators. Metals such as iron (Fe) and copper (Cu) conduct electric current due to the presence of delocalized "free" electrons. In semiconductors, the conductivity is influenced by the temperature and the presence of minute amounts of impurities[1]. Examples of semiconductors that have been used for technological applications are silicon (Si) and gallium arsenide (GaAs). Insulators, on the other hand have no significant room temperature electrical conductivity, and are generally brittle and hard materials, for instance quartz (SiO_2) and salts (such as NaCl).

Semiconductors have been grouped into elemental and compound semiconductors which are located in groups IV and II-VI or III-V of the Periodic Table, respectively. For example, Si and Ge are found in group IV, while MgO and ZnO are group II-VI semiconductors, and GaAs and InP are III-V semiconductors. Ternary compounds such as InGaAs and GaAsN are also classified as group III-V semiconductors due to the substitution of the isoelectronic elements in the alloys.

Semiconductors form the basis of all modern electronics because of their application in devices such as transistors[1] (Bardeen, Brattain and Shockley received the Noble Prize in 1956 for creating the first transistor). The properties of

electronic devices embedded in integrated circuit (IC) chips depend on the classes of semiconductors used.

Materials are characterized by a gap of forbidden energy states above the highest occupied band, which is referred to as the *band gap* or *energy gap* (E_g). The band gap separates the completely occupied valence band (VB) from the higher energy conduction band (CB). In metals, the valence band is partially filled; hence the electrons are weakly bound to the atomic lattice and are relatively free to move from one atom to another within the crystal. Thus, the valence and conduction bands overlap, which makes metals good conductors of electric current. The valence electrons are tightly bound to the atomic lattice in insulators and are localized at atomic sites. Thus, large energies will be required to excite electrons from the valence band to the empty conduction band as evident by the large band gap. In semiconductors, the valence electrons in the crystal structure are not as strongly bound to the atomic lattice compared with insulators and if thermally excited, they may be promoted to the conduction band where they are mobile as in metals[2]. Figure 1.1 illustrates a comparison between energy level diagrams of a typical insulator, a semiconductor and a metal. The distinction between these materials is seen by the magnitude of the separation (band gap) between the VB and CB.

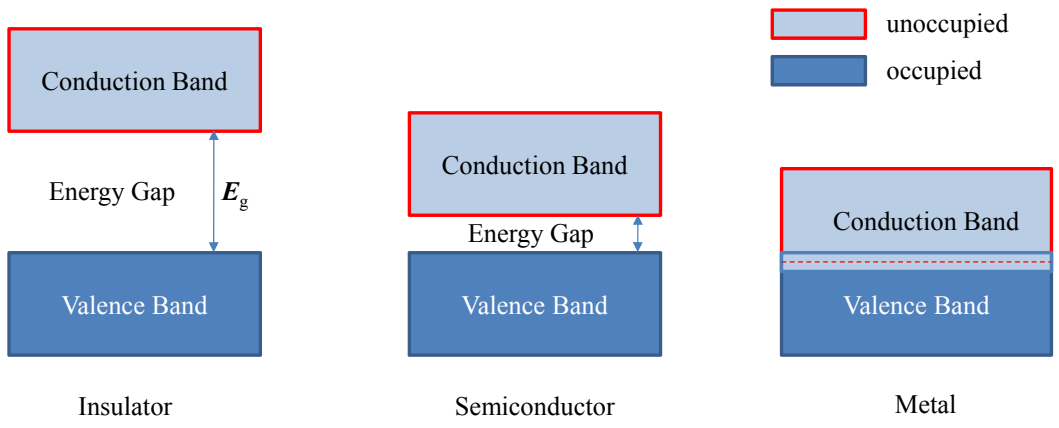


Figure 1.1: Comparison between the valence band, conduction band and energy gap in insulators, semiconductors and metals. The color coding indicates the occupancy of the band.

In semiconductors, the conduction of an electric current is determined by thermal or optical excitations of the valence electrons into the conduction band. The key feature in the success of semiconductors in modern electronics is the possibility to change their electrical and optical properties by orders of magnitude with the introduction of small quantities of impurity atoms.

1.1 Point defects

The class of crystal defects called *point defects* can be due to an atom missing from a regular lattice site (vacancy), atoms in incorrect lattice sites (antisite/substitutional impurity defects) or an atom in an open space between two ordinary lattice host atoms (interstitial defect). Impurity atoms can also be found embedded in defect structures such as substitutional or interstitial-vacancy complexes. The different types of point defects are shown in Figure 1.2. These imperfections have a large impact on the electrical and optical properties of semiconductors which are significantly altered even if only 1 out of 10^9 atoms is replaced by a defect[3]. The entire semiconductor industry relies on intentionally incorporating foreign atoms or impurities, commonly known as *doping* to tailor make new materials with novel properties and also to improve the existing ones.

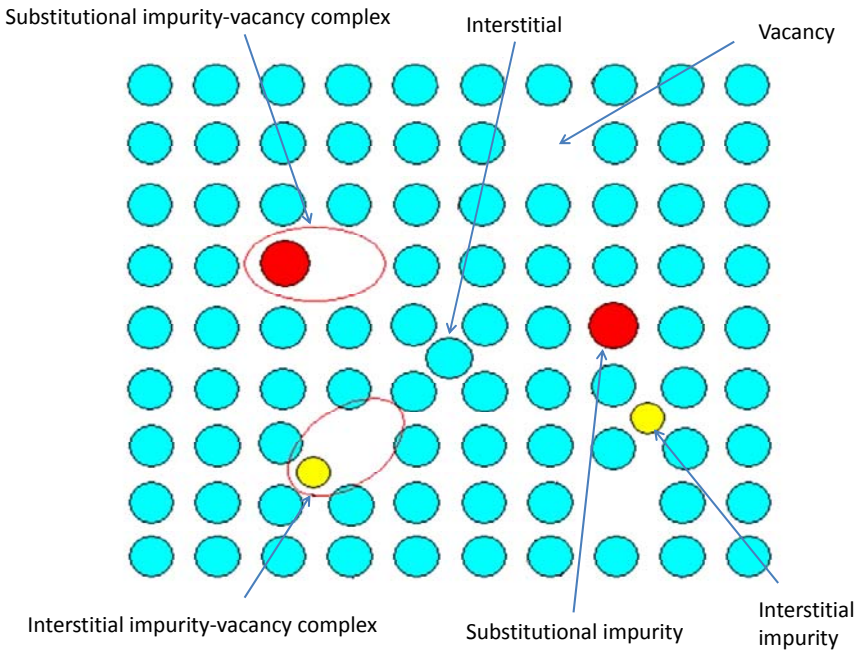


Figure 1.2: A schematic diagram showing different types of point defects.

Doping is used to control the concentration of the majority charge carriers, which can either be electrons or holes (the lack of an electron can behave like a positively charged particle). When doping results in high concentration of holes as charge carriers, the semiconductor is termed *p*-type and if doped with electrons as the majority charge carriers then it is called an *n*-type semiconductor. Pure semiconductors are of little practical application and must be doped with impurity atoms to obtain the desired optical and electrical properties. An impurity atom or dopant will change the electrical and optical properties of a semiconductor when it acts as a donor, contributing electrons to the conduction band or an acceptor, creating holes in the valence band. The semiconductor technology industry is driven by two main objectives viz., engineering new materials with unique electrical and optical properties, and device scalability which corresponds to the reduction of the size of individual constituents in integrated circuits[3,4]. These objectives require a detailed understanding of atomistic mechanisms of defect formation and control of the defects in semiconductors. A dopant or impurity atom serves as a donor or acceptor depending on its location in the crystal lattice structure. For example, a group IV atom substituting a group III atom in a III-V semiconductor will add an extra free electron into the conduction band and act as a donor. However, if the group IV atom is located on a group V lattice site, a hole will be created and thus act as an acceptor.

Doped semiconductors have a wide range of applications such as substrates for high speed electronic and optoelectronic integrated circuits, photorefractive sensor devices, or for radiation and particle detectors. The functionality in one field or the other is strongly determined by the energy levels introduced in the band gap related to the impurity atoms. GaAs has some exceptional electronic and optical properties that make it superior to silicon in some applications and these include the high electron mobility and low noise generation when operated at high frequencies.

This dissertation focuses on the cubic III-V semiconductors; GaAs and GaP, which have a zinc-blende (ZnS) structure. The arrangement of the atoms is identical to diamond but each atom of the III-V semiconductor is surrounded by

four atoms of the other element. In addition, these atoms are characterized by tetragonal covalent bonds in which each atom is four fold coordinated. Figure 1.3 depicts a typical configuration of atoms in a GaAs crystal unit cell showing 14 Ga atoms and 4 As atoms with atomic positions (1/4, 1/4, 1/4,) and (0, 0, 0), respectively.

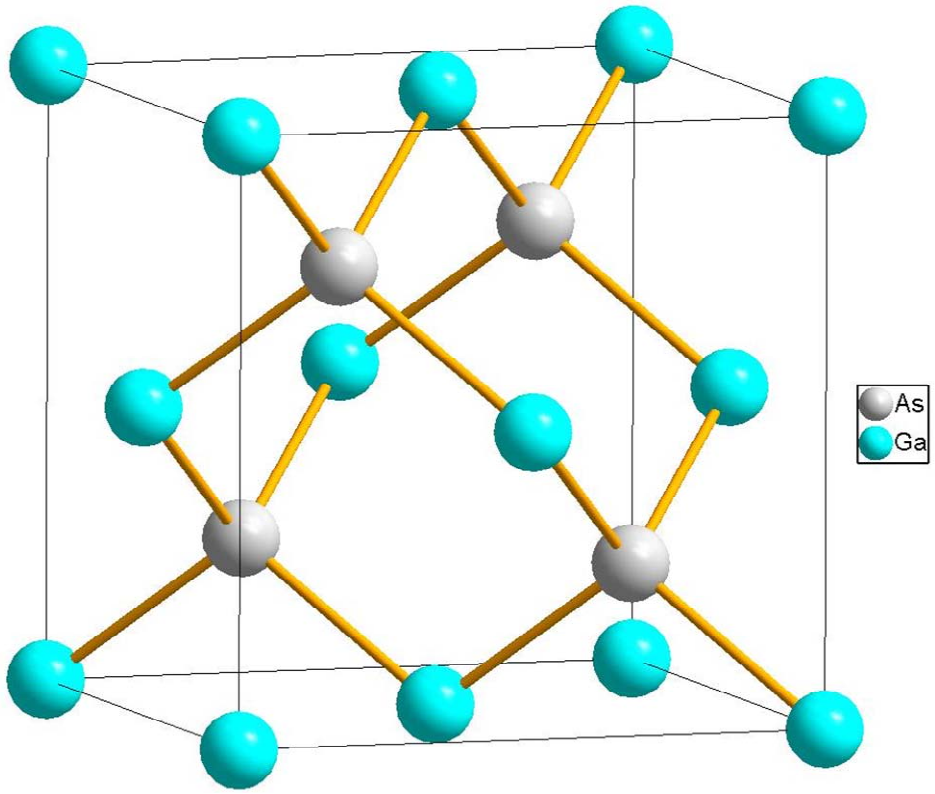


Figure 1.3: Zinc-blende structure of cubic III-V semiconductors.

GaAs being an efficient light emitter, enables high frequency operation and fast switching speeds hence it is used in microwave frequency ICs, infrared LEDs, laser diodes and solar cells for applications in satellite communication, mobile telephones, data storage and radar systems[5]. GaP has an indirect band gap of 2.26 eV and is mainly used in the manufacture of low-cost red, orange, and green LEDs with low to medium brightness[6,7].

1.2 Literature Review

The research of defects in semiconductors has been an area of interest since the beginning of the semiconductor research in the late 1940s. The properties of a semiconductor are not only determined by the chemical nature of a dopant but

also by its location in the crystal lattice[3]. As a consequence, throughout the last half century, strong efforts in basic and applied research using different experimental and theoretical tools have been employed not only to characterize the electrical and optical properties of defects in semiconductors, but also to determine the location of these defects[3,4]. Relevant Mössbauer emission spectroscopy studies of GaAs and GaP and other techniques are discussed below.

1.2.1 Lattice site location

Over the past few decades, Sn defects have been studied by Mössbauer emission spectroscopy in GaAs[8] using implantation of ^{119m}Sn with the majority of Sn atoms occupying substitutional Ga sites upon implantation and other Sn atoms are associated with possible impurity-vacancy complexes. Further studies on defect structures[9] upon implantation and annealing at 200 ^{o}C confirmed the location of Sn impurity atoms on Ga substitutional sites, the existence of Sn-vacancy complexes and possibly interstitially located impurity atoms. These impurity-vacancy complexes created by Sn implantations were evident only after annealing between 200 ^{o}C and 400 ^{o}C after which the Sn atoms were located on undisturbed Ga substitutional sites[9,10]. The annealing process showed a constant average total site population[8,9] over the measured temperature range (200 ^{o}C – 700 ^{o}C) which suggested that the annealing resulted from the dissociation of the impurity-vacancy complexes[10]. This served as unequivocal and independent evidence of the location for the different sites using Mössbauer spectroscopy[8].

Mössbauer studies of Sn impurity atoms in GaP[11,12] and other group III-V semiconductors such as InP, InAs, and InSb[13-17] using implantation of radioactive ^{119}In and ^{119m}Sn as precursor isotopes have shown similar results. Sn atoms occupied substitutional III sites upon implantation and thermal annealing. However, ^{119}Sb implantations showed Sn on substitutional V sites that dominated after annealing at 350 ^{o}C. These sites were then inherited by the ^{119}Sn Mössbauer daughter atoms which maintained the respective lattice locations due to the lower recoil energies imparted to the Sn atoms as compared to the displacement threshold energies (E_d)[17]. Site selective implantation[13] was observed by using different types of precursor isotopes which decayed to ^{119}Sn in the 24 keV

Mössbauer state. As an amphoteric dopant, Sn atoms that occupied substitutional III or V sites act as a donor or acceptor, respectively[16]. The electron densities and hence the isomer shift values were lower for the III sites compared to the V sites[13,15] as shown in Table 1.1.

Table 1.1: Isomer shifts for Sn on III and V sites in semiconductors[13,15].

Host	GaP		GaAs		InAs	
Sn site	Ga	P	Ga	As	In	As
δ (mm.s^{-1})	1.58 (3)	1.85 (5)	1.76 (3)	1.83 (4)	1.77 (4)	1.91 (3)

The assignment of these different lattice sites corroborated electrical activity data and channeling experiments[16]. The extracted isomer shifts of the different lattice sites compares well with theoretical values[18]. The calculated Debye temperatures[15,16] for the III sites were much higher than V sites in In compounds as shown in Table 1.2. However, for Ga based III-V materials slightly higher values for the V sites relative to the III sites were observed as presented in Table 1.3. The disparity in the Debye temperature values has been interpreted using the Einstein-Debye model to account for the different electronic natures to the charge states of the dopants[17].

Table 1.2: Debye temperature for Sn on III and V site in In compound[15,16].

Host	InP		InAs		InSb	
Sn site	In	P	In	As	In	Sb
θ_D (K)	202(6)	186(10)	180(4)	165(10)	165(4)	157(5)

Table 1.3: Debye temperature for Sn on III and V site in Ga compound[15,16].

Host	GaP		GaAs		GaSb	
Sn site	Ga	P	Ga	As	Ga	Sb
θ_D (K)	226(5)	233(10)	202(5)	200(7)	177(4)	187(10)

Mössbauer emission spectroscopy studies [19] of Fe impurities in GaAs and GaP using ^{57}Co (^{57m}Fe) radioactive isotopes introduced by diffusion doping showed

that Fe atoms substitute Ga atoms and form tetrahedral bonds with its nearest neighbors. A more recent study[20] identified Fe associated with lattice vacancies and substitutional impurity atoms in surface and bulk regions, respectively.

1.2.2 Electronic configuration – Charge states

The bonding which is totally covalent in group IV elemental semiconductors has some ionic character in III-V compound semiconductors where a sp^3 hybrid orbital is formed. The hybrid formation constitutes the 'donation' of an electron by an element in the group V to another in the group III. This allows both partners to form sp^3 hybrid orbitals resulting in a zinc-blende lattice structure. Fe has an outer shell configuration $3d^6\ 4s^2$ in its neutral state, however Electron Paramagnetic Resonance (EPR)[21] measurements of Fe doped GaAs ingots grown by gradient-freeze technique have evinced the presence of trivalent iron with a $3d^5$ configuration on a Ga substitutional site. This assignment is consistent with a Mössbauer study carried out[22] where diffusion of ^{57}Co in GaAs introduced at least two states of Fe with electronic configuration near to $3d^5$ but with different atomic environments. Further diffusion studies[20] showed isolated Fe substitutional impurity atoms with $3d^5$ electronic configuration in bulk regions while Fe which formed associations with lattice vacancies in the surface regions exhibited Fe^{3+} ($3d^5$) and Fe^{2+} ($3d^6$) character in *p*-type and *n*-type GaAs samples, respectively. Electron spin resonance (ESR) and Hall effect[23] studies of low temperature relaxation of solid solution of Fe in GaP confirmed Fe in substitutional position with $3d^5$ electronic configuration. However, a neutral Fe interstitial component with a different electronic configuration $3d^8$ was related to a diffusion result of Fe centers forming association with lattice vacancies.

The occupation of substitutional sites is governed by chemical effects rather than kinetic displacement mechanisms. The impurity atoms tend to form tetrahedrally coordinated sp^3 orbital with their valence electrons and this governs the selection of lattice sites. Thus, impurities are normally most stable at substitutional sites and introducing dopant atoms will increase the number of charge carriers.

1.3 Objectives of this study

The incorporation of foreign atoms within a lattice can be achieved either by diffusion or ion implantation. Ion implantation is favored as it offers precise control of depth profile and concentration of dopants in addition to its ability to circumvent diffusion and solubility limits. Thus, any ion can practically be accelerated and implanted. In this study, defects created by implantation of radioactive $^{57}Mn^{*}$ ions into GaAs and GaP single crystals held at ambient temperatures followed by annealing between 77 K and 700 K were studied using Mössbauer emission spectroscopy at the Isotope Separator On-Line DEvice (ISOLDE) Facility at CERN, Geneva, Switzerland. The aim of this study was to determine the location and chemical nature of Fe atoms in different lattice sites, namely substitutional, interstitial, and/or Fe embedded in defects structures such as impurity-vacancy complexes. The local environments of the impurity atoms and the different annealing stages of the radiation damage have been investigated as functions of temperature. Due to its extreme sensitivity, Mössbauer spectroscopy has been adopted as an investigative tool, to study the lattice location, charge states and local surroundings of the impurity atoms by monitoring the temperature dependence of the extracted hyperfine parameters and Debye temperatures of Fe at the different lattice sites.

The current study had the following objectives:

1. To identify substitutionally and interstitially incorporated Fe in host matrix, and any Fe impurity-vacancy complexes as well as to monitor any possible diffusion mechanisms as a function of temperature.
2. To determine the isomer shift and electric quadrupole splitting values, areal fraction of Fe at the different lattice sites and in complexes, and the corresponding Debye temperatures of the Fe atom at the different lattice sites.
3. To investigate the annealing behavior of the radiation damage in GaAs and GaP as a function temperature.
4. To establish systematic trends of the hyperfine parameters for the materials under study.

The approach to address the aforementioned objectives is presented in the dissertation outline in the subsequent section.

1.4 Dissertation Outline

The introduction, background, aim and objectives of the study are outlined in the current chapter. The theory of Mössbauer spectroscopy and the hyperfine interactions parameters are discussed in **chapter 2**. **Chapter 3** focuses on the experimental details including the principles of ion implantation and the production of ^{57}Mn* beams at ISOLDE. Chapter 3 also presents the layout of the Mössbauer equipment and descriptions of the measurements conducted on GaAs and GaP. The results are presented in **chapter 4** and finally, conclusions and outlook are presented in **chapter 5**, together with recommendations for exploring new areas of research based on these semiconductor materials.

Chapter 2

Mössbauer Spectroscopy

2.1 Introduction

The phenomenon of resonant recoil-free emission and absorption of gamma (γ) rays in nuclei without the loss of energy due to recoil and thermal broadening is known as the Mössbauer Effect[24]. This effect was discovered by R. L. Mössbauer in 1958 and provides a means of probing the local surroundings of particular atoms in amorphous or crystalline solids. The Mössbauer Effect can be used to study the properties of an emitting nucleus (Mössbauer Emission Spectroscopy – MES) and of an absorbing nucleus (Mössbauer Absorption Spectroscopy – MAS). Detailed information on the electronic, magnetic and geometric structure[25] of an impurity atom environment can be extracted from the parameters that characterize the Mössbauer spectrum of samples, i.e. hyperfine interactions namely the electric monopole, electric quadrupole and magnetic dipole interactions[26].

2.2 Mössbauer Effect: Resonant emission and absorption

When a nucleus (with $\boldsymbol{Z}$ protons and $\boldsymbol{N}$ neutrons) of mass m in an excited state decays to the ground state by emitting a γ-ray of energy, E_γ, the nucleus recoils with energy E_R.



Figure 2.1: Nuclear recoil after gamma emission.

Hence, the energy carried by the γ-ray is not the transition energy E_O, but $E_\gamma = E_O - E_R$. This prevents resonant absorption of the γ-ray by another nucleus of

the same kind (same ***Z*** and ***N***). Figure 2.2 illustrates the difference in the emission energy and the insufficient γ-ray energy resulting from the loss in energy due to recoil.

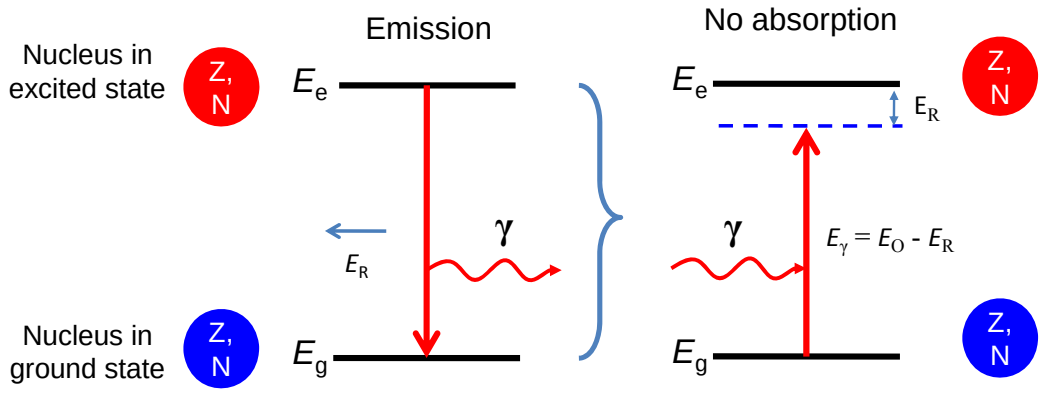


Figure 2.2: Non-resonant absorption of γ radiation.

However, when the nucleus is in an atom which is bound in a solid with mass ***M***, the loss in energy due to recoil becomes infinitesimally small due to the effective mass of the whole system being much greater than the nucleus ($\boldsymbol{M} \gg m$), making E_R very small relative to E_O resulting in a nearly *recoil-free emission* of the γ photon. This forms the bedrock of the Mössbauer Effect. Figure 2.3 depicts the resonant emission and absorption of γ-radiation between a nucleus in the excited state with energy, E_e and another nucleus in the ground state with energy, E_g.

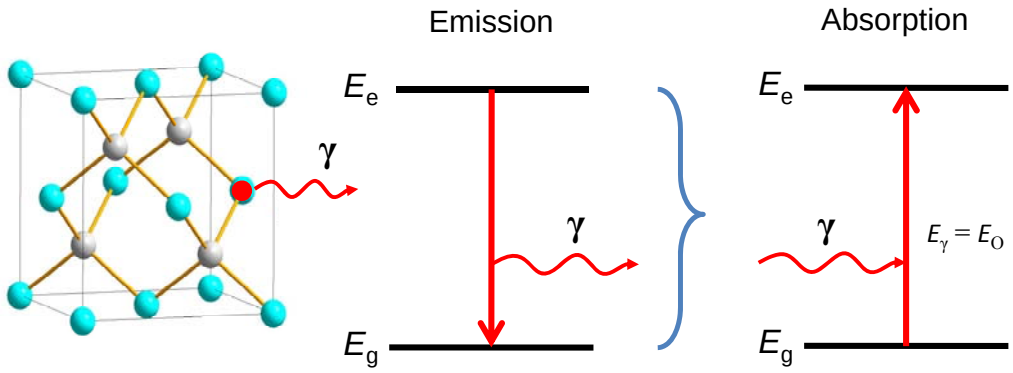


Figure 2.3: Resonant emission and absorption of γ radiation.

2.3 Recoil-free fraction and Debye Temperature

When the gamma emitting (or absorbing) nucleus is embedded in a crystal lattice, the recoil energy is transferred mostly to lattice vibrations, but since $\boldsymbol{M} >> m$, the linear momentum transferred to the nucleus by photon emission and absorption practically disappears. The vibrational energy is dissipated as heat into the near lattice environments[27]. In an Einstein solid, there are $3N$ vibrational modes (where N is the number of atoms) each having the same frequency $\boldsymbol{\omega_E}$. The emission and absorption of a γ-ray is accompanied by the transfer of integral multiples of quantized phonon energy ($0, \pm\hbar\omega_E, \pm 2\hbar\omega_{E,}.....$) to the lattice[24,28]. According to R. L. Mössbauer[24], when $\boldsymbol{E_R} << \boldsymbol{\hbar\omega_E}$, there exists a certain fraction, f of transitions which take place without lattice vibrations (*zero-phonon transition)*. f is called the *recoil-free fraction* and is related to the vibrational properties of the crystal lattice by the expression;

$$f = e^{-\boldsymbol{k}^2\langle x^2\rangle} \tag{2.1}$$

where $\langle x^2\rangle$ is the mean square displacement of a nucleus along the direction of the wave vector $\boldsymbol{k}$ of the emitted γ-ray. The wave vector is related to the momentum (p_γ) of the γ-ray by the expression;

$$p_\gamma = \frac{\boldsymbol{k}h}{2\pi} \tag{2.2}$$

where h is the Planck constant. However, the momentum of the γ-ray is related to its energy and the speed of light (c) by the equation;

$$p_\gamma = \frac{E_\gamma}{c}. \tag{2.3}$$

Thus from equation (2.2), the wave vector can be written in the following form;

$$\boldsymbol{k} = \frac{E_\gamma}{\hbar c} \tag{2.4}$$

with $\hbar = h/2\pi$. Consequently, the expression for the recoil-free fraction in equation (2.1) can be written as,

$$f = \exp\left(-\frac{E_\gamma^2}{\hbar^2 c^2}\langle x^2\rangle\right) \tag{2.5}$$

In an Einstein solid, the mean square displacement can be written as

$$\left\langle x^2 \right\rangle = \frac{\left\langle E \right\rangle}{m\omega_{\mathrm{E}}^2} \tag{2.6}$$

where the mean energy $\left\langle E \right\rangle$ of the oscillators is given by the quantum number of the oscillators as,

$$\left\langle E \right\rangle = h\omega_{\mathrm{E}}\left(\left\langle n \right\rangle + \frac{1}{2} \right) \tag{2.7}$$

where the thermal average of $\left\langle n \right\rangle$ can be written in terms of the Planck's distributions function as

$$\left\langle n \right\rangle = \frac{1}{\exp(\hbar\omega_{\mathrm{E}} / kT) - 1}. \tag{2.8}$$

Combining equations (2.5) – (2.8) gives the following expression for f:

$$f = \exp\left[-\frac{E_{\mathrm{R}}}{k\theta_{\mathrm{E}}} \coth\left(\frac{\theta_{\mathrm{E}}}{2T} \right) \right]. \tag{2.9}$$

The Debye model on the other hand abandons the idea of single vibrational frequency of the lattice atoms and embodies a continuum of oscillator frequencies ranging from zero up to a maximum ω_{D} which follows the distribution formula $N(\omega)$ = constant x ω^2. The Debye model leads to the expression:

$$\boldsymbol{k}^2 \left\langle x^2 \right\rangle = \frac{\hbar}{2M} \int_0^{\omega_{\mathrm{D}}} \frac{N(\omega)}{\omega} \coth\left(\frac{\hbar\omega}{2k_{\mathrm{B}}T} \right) \mathrm{d}\omega \tag{2.10}$$

which integrates to the more familiar equation

$$f = \exp\left\{ -\frac{3}{2} \frac{E_\gamma}{k_{\mathrm{B}}\theta_{\mathrm{D}}} \left[1 + 4\left(\frac{T}{\theta_{\mathrm{D}}} \right)^2 \int_0^{\theta_{\mathrm{D}}/\mathrm{T}} \frac{x}{e^x - 1} dx \right] \right\} \tag{2.11}$$

where k_{B} is Boltzmann constant and θ_{D} is the characteristic Debye temperature. f is also known as Debye-Waller factor or Mössbauer-Lamb factor. E_{R} is the recoil energy of the nucleus which is determined by the nuclear mass m and the γ-energy E_γ and can be written as:

$$E_R = \frac{E_\gamma}{2mc^2}. \tag{2.12}$$

The Debye temperature is given by:

$$\theta_D = \frac{h\omega_D}{k_B}. \tag{2.13}$$

For $T << \theta_D$, equation (2.11) reduces to:

$$f = \exp\left[-\frac{E_R}{k_B\theta_D}\left(\frac{3}{2} + \frac{\pi^2 T^2}{\theta_D}\right)\right] \tag{2.14}$$

and at absolute zero

$$f = \exp\left(-\frac{3E_R}{2k_B\theta_D}\right). \tag{2.15}$$

In the high temperature limit, for $T > \theta_D$, f approximates to:

$$f = \exp\left(-\frac{6E_R T}{k_B\theta_D}\right). \tag{2.16}$$

The high temperature approximation of f shows that the resonance area drops exponentially with the increase in temperature, with a gradient that can be used to determine the Debye temperature (θ_D). The low temperature approximation shows that at T = 0 K, f = 1 and it decreases with increasing recoil energy (i.e. photon energy) and temperature, and with decreasing Debye temperature. The *Debye temperature* is a measure of the strength of the bonds between the Mössbauer atom and the nearest neighbouring atoms in the lattice[27].

2.4 Experimental Resonance Condition

The observation of resonance in Mössbauer spectroscopy for a particular nuclide is governed by the mean lifetime (τ_N) of the excited state and the transition energy E_O. The effect of the mean lifetime and transition energy on resonance and possible range of operation are discussed in the section below.

2.4.1 Natural line width

According to Heisenberg Uncertainty Principle, a nuclear level with mean lifetime (τ_N) has an energy uncertainty (Γ) given by

$$\Gamma = \frac{\hbar}{\tau_N} \tag{2.17}$$

where τ_N is related to the half-life ($t_{1/2}$) of the radioactive nucleus by the relation

$$\tau_N = \ln 2.t_{1/2}. \tag{2.18}$$

^{57}Fe is the most frequently utilized Mössbauer nucleus and has a energy transition of 14.4 keV and a mean lifetime of 141 ns, so it has a linewidth of

$$\Gamma = \frac{\hbar}{\tau_N} = 4.7\times10^{-9}\,\text{eV}. \tag{2.19}$$

This gives an energy resolution of approximately 5×10^{-9} eV and an energy ratio given by $E_\gamma/\Gamma = 3.1 \times 10^{12}$. Mössbauer spectroscopy has undoubtedly the highest energy resolution amongst all spectroscopic methods[29,30] and changes in nuclear levels as small as 1 part in 10^{12} can be detected[25]. In order to modify the γ-ray energy, a simple Doppler movement can be utilized, and the convention in Mössbauer spectroscopy is to use Doppler velocity scale in mm.s^{-1} instead of energy.

The distribution of energies about E_O (= transition probability as a function of transition energy E) is given by the Breit-Wigner formula[27],

$$I(E) = \frac{(\Gamma/2)^2}{(E - E_o)^2 + (\Gamma/2)^2} \tag{2.20}$$

with a Lorentzian distribution as shown in Figure 2.4. $\Delta E = \Gamma$ is the energy width of the excited state (e) with a mean lifetime (τ_N) and also gives the Full Width of the transition spectral line at Half Maximum (FWHM).

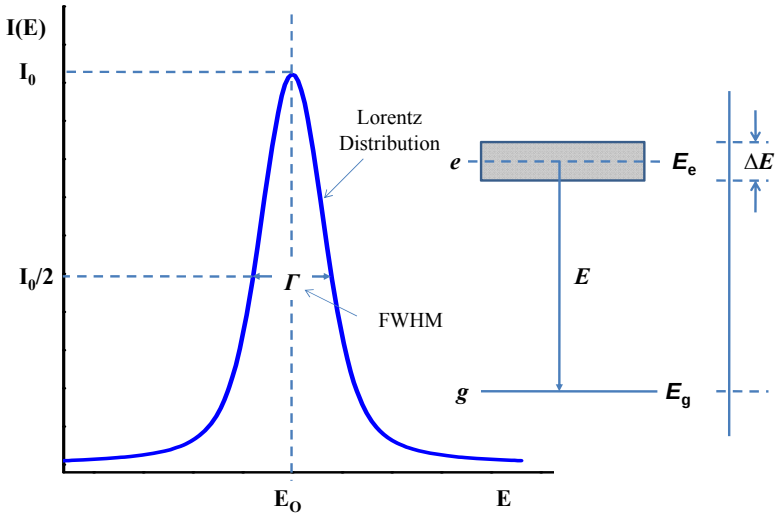


Figure 2.4: Intensity I(E) as a function of transition energy E.

The width of a relevant transition line is governed by the mean lifetime of the excited state. Nuclides suitable for Mössbauer spectroscopy should possess excited states with mean lifetimes in the range 10^{-6} s to 10^{-11} s. Longer lifetimes produce too narrow emission and absorption lines which would not overlap effectively. These longer lifetimes would require an extremely small Doppler velocity in the order of μm.s^{-1} which is challenging to achieve experimentally[27], while for shorter lifetimes the resonance overlap would be significantly spread out and thus no longer distinguishable from the spectrum base line. This effect of lifetime on resonance is depicted in Figure 2.5.

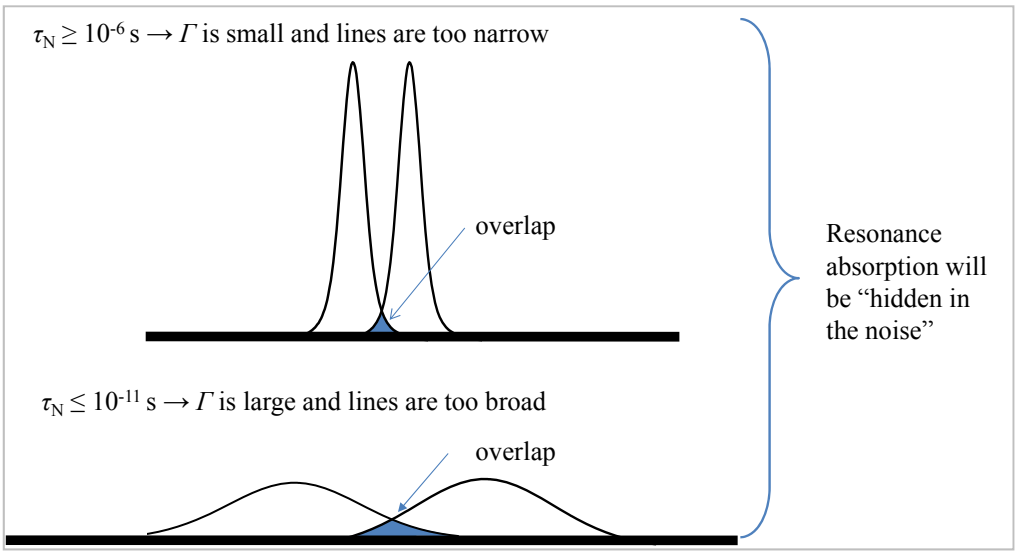


Figure 2.5: Effect of mean lifetime on resonance.

2.4.2 Transition Energy

The recoil energy (E_R) of a nucleus is related to the transition energy (E_O) or γ-ray energy (E_γ) by the expression,

$$E_R = \frac{E_\gamma^2}{2mc^2}. \tag{2.21}$$

The higher the transition energy the greater the recoil energy. High transition energies, $E_O > 180$ keV will cause very large recoil effects. This will destroy the resonance while γ-quanta with relatively small energies, $E_O < 5$ keV will be mostly absorbed in the source and absorber.

2.5 Factors influencing the Mössbauer Effect

The interactions between the nucleus and its surrounding electrons lead to changes in the nuclear energy levels of the order of 10^{-7} – 10^{-8} eV. These interactions are called *hyperfine interactions*. Mössbauer Spectroscopy serves a bridge linking the nucleus with its surroundings, through the hyperfine interactions, and is the only effect that gives a direct measure of these energy changes. The energy changes are sensitive to changes in the structure, whether crystalline or amorphous, lattice periodicity and probe nucleus-complexes. Moreover, changes in the magnetic ordering, oxidation state of the probe nucleus in a compound, coordination, and the effects of ligands, as well as the diffusion and vibrations of atoms in a solid can be investigated by Mössbauer spectroscopy[29].

2.5.1 Electric Monopole Interaction: Isomer shift

The isomer shift (δ) results from the electrostatic interaction between the charge distribution of the nucleus and those electrons which have a finite probability of being present in the region of the nucleus, the *s*-electrons. The interaction causes shifts in the nuclear energy levels of the absorber and the source nuclei, this in turn affect the nuclear ground state and excited state levels in different extents as illustrated in Figure 2.6(a). Equations (2.22) and (2.23) show the respective

energy transitions E_A and E_S between the excited state and the ground state in the absorber and the source, respectively.

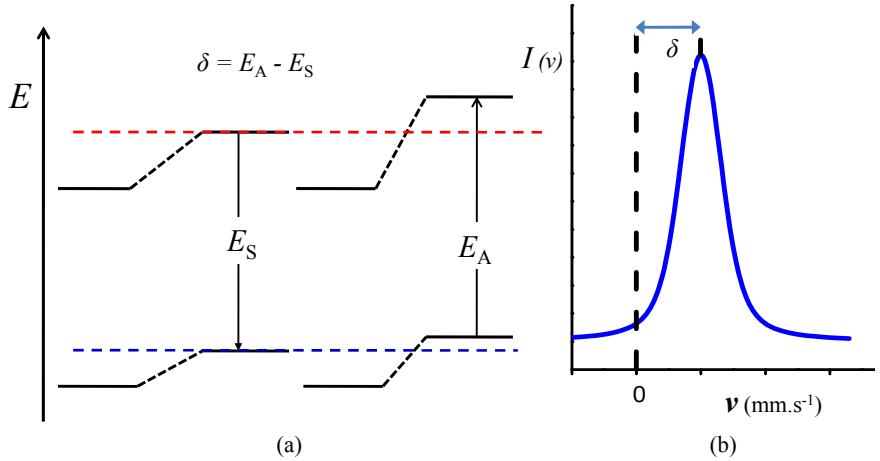


Figure 2.6: Effects of electric monopole interaction: Isomer shift.

The energy gaps E_A and E_S are given by

$$E_A = \frac{2}{3}\pi Z e^2 |\psi(0)|_A^2 \left[\left\langle r_e^2 \right\rangle - \left\langle r_g^2 \right\rangle\right] \tag{2.22}$$

and

$$E_S = \frac{2}{3}\pi Z e^2 |\psi(0)|_S^2 \left[\left\langle r_e^2 \right\rangle - \left\langle r_g^2 \right\rangle\right] \tag{2.23}$$

where $\left\langle r^2 \right\rangle$ is the expectation value for the square of the nucleus radius[27] and $|\psi(0)|^2$ is the corresponding probability density. Thus the Mössbauer transition energy between the absorber and the source will be slightly different, resulting in no resonant absorption of any emitted γ-radiation.

2.5.1.1 Observing resonance

If the nuclei in the source and absorber have the same environments, then their transition energy will be the same and hence Mössbauer resonance absorption will occur. This is due to the electric monopole interaction causing shifts in the nuclear energy levels of both the absorber and source nuclei to the same extent. However, if the electron density at the nuclei in the source is different from that in the absorber, then the Mössbauer transition energy will vary slightly in the two nuclei. Thus a γ-ray with variable energy within the limits of the shift of the nuclear

energy levels is required to observe resonant absorption. In conventional Mössbauer absorption spectroscopy, this is achieved by changing the energy of the γ-ray source along the direction of propagation by the Doppler Effect. In this way, the emitted γ-ray is absorbed and detected as a function of velocity. However, in Mössbauer emission spectroscopy at ISOLDE, because the sample acts as the source of γ-rays, the detector instead of the source is vibrated within the limits of the energy difference between the two nuclei for resonance to occur. This will appear as a shift (from the zero velocity) in the position of the absorption peak known as the *isomer shift*. This is illustrated in Figure 2.6(b) and is proportional to the difference in the electron densities at the two nuclear sites in the source and absorber. In terms of spectra, the isomer shift is the velocity at which maximum absorption occurs, while the difference in the relative energy levels between the source and the absorber, ΔE, is equal to the shift caused by the Doppler Effect at this particular velocity. In the former case, when the nuclei are in the same environments, resonance absorption will occur at zero velocity even when either the source or absorber is vibrating with respect to the other.

2.5.1.2 Shielding effect

The isomer shift is strictly a function of the *s*-electron density which is greatly modified by the presence of overlapping *p*, *d*, and *f* orbitals. The electron densities of these orbitals influence the spatial distribution of the *s*-electrons in the same atom, because they *'screen or shield'* the *s*-electrons from the nucleus[31] through inter-electronic repulsion. An increase in the 3*d* density increases the isomer shift; while an increase in the 4*s* density decreases the isomer shift. A gradual increase in the number of 3*d* electrons causes a reduction in the total *s*-electrons in the *s*-electron density, resulting in the isomer shift of Fe^{2+} ($3d^6$) shifting more to positive velocity than Fe^{3+} ($3d^5$). Thus Fe^{2+} ($3d^6$) ion has larger isomer shift than Fe^{3+} ($3d^5$) ion[31].

2.5.1.3 Second-order Doppler Shift

The total observed shift of the energy levels is not entirely due to the electric monopole interaction but may also arise from the thermal motion of the

Mössbauer atoms. These thermal vibrations result from the changes in temperature and this temperature dependent contribution which causes the shifting of the energy levels is called the *second-order Doppler shift* (δ_{SOD}). Thus the total observed shift of the entire Mössbauer spectrum is called the center shift *(*δ_C), which is given by the sum of the isomer shift (δ_{IS}) and the second-order Doppler shift (δ_{SOD}). The isomer shift is therefore given by:

$$\delta_{IS} = \delta_C - \delta_{SOD}. \tag{2.24}$$

The second-order Doppler shift, also known as the thermal shift is proportional to the mean square velocity of the probe nucleus[32,33] and can be written as:

$$\delta_{SOD} = \frac{\langle v^2 \rangle}{2c^2} E_\gamma \tag{2.25}$$

$$= \frac{\langle v^2 \rangle}{2c}. \tag{2.26}$$

The shift of the energy levels due to the second order Doppler Shift can be approximated in a Debye model as follows;

$$\delta_{SOD} = -\frac{3}{2}\frac{k_B \theta_D}{mc}\left[\frac{3}{8} + 3\left(\frac{T}{\theta_D}\right)^4 \int_0^{\theta_D/T} \frac{x^3}{e^x - 1} dx\right]. \tag{2.27}$$

2.5.1.4 Isomer shift and *s*-electron density

The isomer shift, in Doppler velocity units, can be written as

$$\delta_{IS} = E_A - E_S \tag{2.28}$$

which is given by the expression[27],

$$\delta_{IS} = \frac{2}{5}\pi Ze\left(\rho_a - \rho_s\right)\left(R_e^2 - R_g^2\right) \tag{2.29}$$

where Z is the atomic number, e is the electronic charge. R_e and R_g are the radii for the excited and ground state nuclei, respectively. The electron densities at the nucleus in the absorber and source material are ρ_a and ρ_s, respectively, given by:

$$\rho_a = -e\left|\psi(0)\right|_a^2 \text{ and } \rho_s = -e\left|\psi(0)\right|_s^2. \tag{2.30}$$

It can be seen from equation (2.29) that the isomer shift is directly proportional to the difference in the *s*-electron charge densities between the nuclei in the absorber and the source $\Delta\rho(0)$. Thus equation (2.28) can be written in the form,

$$\delta_{IS} = \alpha\Delta\rho(0) \tag{2.31}$$

where α is a proportionality constant known as the calibration constant dependent on nuclear parameters[17,29] such as nuclear radius (***R***) and proton number (***Z***).

In Mössbauer emission spectroscopy at ISOLDE, the same absorber (detector) is used for a series of temperature dependent measurements on samples which acts as sources for γ-radiation, and thus $\rho_a(0)$ is a constant. Therefore, the measured isomer shift is a linear function of the *s*-electron density at the nucleus of the source (sample):

$$\delta_{IS} = \alpha\left[\rho_a(0) - \rho_s(0)\right] \tag{2.32}$$

where ρ_a is generally known. Thus ρ_s can be determined directly from the isomer shift. In order to compare and discuss experimental results, an α-Fe foil is used for calibration as a reference for all measured isomer shift values. The isomer shift is usually very small, for example, δ = 0.3 mm.s^{-1} corresponds to an energy shift of $\approx 10^{-8}$ eV. This minute energy changes can only be detected in Mössbauer effect and the isomer shift is only accessible by this effect[29]. The electron densities are generally assumed not to depend measurably on temperature.

The isomer shift is therefore sensitive to the charge density distribution caused by the environments around the nucleus, that is, any factor that affects the number and/or distribution of valence electrons. This gives information on the oxidation state, coordination number, ligand type coordinated to iron cations, and spin state of iron atoms. At room temperature, Fe^{3+} in a crystalline lattice has an isomer shift value of 0.20 - 0.50 mm.s^{-1} relative to a Fe metal and a quadrupole splitting < 1.5 mm.s^{-1}. In a tetrahedral coordination, Fe^{2+} normally gives isomer shift value > 1 mm.s^{-1} and quadrupole splitting value > 2 mm.s^{-1} [31]. Isomer shift decreases as the coordination number of the Fe atom decreases and is primarily a function of the spatial arrangement of atoms and the nearest neighbor bonding.

2.5.2 Electric Quadrupole Interaction: Quadrupole Splitting

A nucleus with spin $I > \frac{1}{2}$ has a non-spherical nuclear charge distribution and therefore a non-zero electric quadrupole moment which may be expressed as

$$Q = \frac{1}{e}\int \rho(\boldsymbol{r})(3z^2 - \boldsymbol{r}^2)\mathrm{d}\boldsymbol{r} \qquad (2.33)$$

in the principal axis system[29]. The quadrupole moment interacts with the electric field gradient (EFG) around the nucleus, which is generated whenever the nuclear environment has a charge distribution lower than cubic. This situation exists in non cubic crystal lattices and in the presence of defects in the neighborhood of the probe atom. This interaction of the nuclear quadrupole moment and the electric field gradient splits the nuclear energy levels into sub-states with spin I, (I - 1), (I - 2)… - I without removing the degeneracy between the states having the same spin quantum number I [31,34]. The sub-states are equivalent to saying there exists a set of restrictions placed on the possible angular orientation of the nucleus with respect to the EFG, and these have different energies.

For instance, the ground state of ^{57}Fe has a spin $I = \pm\frac{1}{2}$, while the 14.4 keV excited state, a spin $I = \pm\frac{3}{2}$, and the presence of an EFG does not affect the ground state but splits the excited state into $m_I = \pm\frac{3}{2}$ and $m_I = \pm\frac{1}{2}$ sublevels. Thus two transitions from the ground state are possible, resulting in two lines in the Mössbauer spectrum as depicted in Figure 2.7.

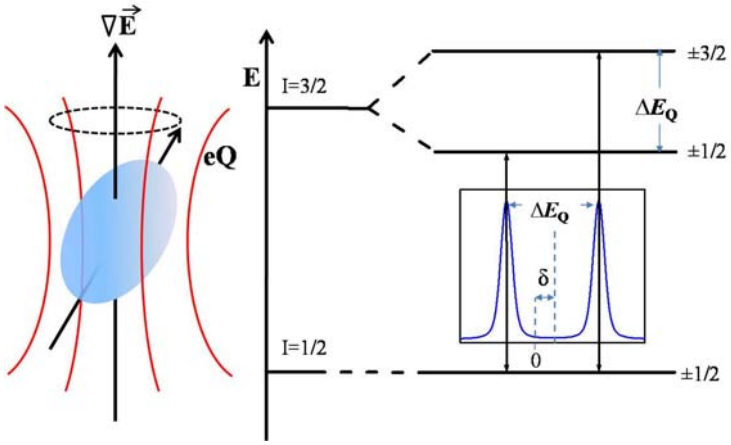


Figure 2.7: Effects of the electric quadrupole interaction: quadrupole splitting.

The degree of splitting of these lines is a measure of energy the difference between the excited states and depends on the nuclear quadrupole moment, the orientation and magnitude of the EFG. The quadrupole moment for a given nucleus is known, but the EFG may arise from charges on the neighboring ion or ligands surrounding the Mössbauer atom and charges in partially filled orbitals of the Mössbauer atom[29]. If lattice sites that have a point group symmetry less than cubic, then the line splitting will occur if the nuclear states have finite quadrupole moments. The energy difference between the two sublevels equals the separation between the two resonance lines and is known as the *quadrupole splitting* given by the expression,

$$\Delta E_{\mathrm{Q}} = \pm \frac{eQV_{ZZ}}{2}\left(1+\frac{\eta^2}{3}\right)^{\frac{1}{2}} \tag{2.34}$$

where e is the electron charge, Q is the nuclear quadrupole moment, V_{zz} is the principal axis component of the EFG interacting with the quadrupole and η is an asymmetry parameter of the electric field given by,

$$\eta = \frac{V_{\mathrm{XX}} - V_{\mathrm{YY}}}{V_{\mathrm{ZZ}}} \tag{2.35}$$

and must satisfy $0 \leq \eta \leq 1$.

The asymmetry parameter is a measure of the deviation of the EFG from axial symmetry and therefore in the presence of axial symmetry at a specific lattice site, $\eta = 0$. Thus, the lattice symmetry reflecting the effect of coordinating atoms, and the clustering of the atoms can be studied by measuring the quadrupole splitting.

For $\eta = 0$, the intensity ratio of the two transitions, $\pm 3/2 \rightarrow \pm 1/2$ and $\pm 1/2 \rightarrow \pm 1/2$ is given by the equation;

$$R = (1+\cos^2\theta)\left(\frac{2}{3}+\sin^2\theta\right)^{-1} \tag{2.36}$$

where θ is the angle between the γ-ray direction and the V_{zz} direction. The sign of the EFG[17,26] can be determined from the equation (2.36).

2.5.2.1 Sources of the Electric Field Gradient

The EFG is defined as the second spatial derivative of the electric potential, and therefore being a tensor, it contains information on the symmetry and orientation of the charge distribution with respect to the crystal lattice[27,29,32]. Therefore, the EFG tensor delivers information on the configuration of the defect causing the gradient of the electric field. The electric charges distributed around a Mössbauer nucleus can contribute to the EFG only when their symmetry is lower than cubic. However, there are two fundamental sources that contribute to the electric field gradient, in principal axis system and with $\eta = 0$, is given by [27,29]:

$$\left(V_{ZZ}\right)_{\text{total}} = \left(V_{ZZ}\right)_{\text{Lat}} + \left(V_{ZZ}\right)_{\text{Val}}. \tag{2.37}$$

The lattice (ligand) contribution $(V_{ZZ})_{\text{Lat}}$ results from the charges on the neighboring ions or ligands surrounding the Mössbauer atom. The second source is known as the valence electron contribution $(V_{ZZ})_{\text{Val}}$ which arises as a result of the charges in the partially filled valence orbitals of the Mössbauer atom.

2.5.2.2 Temperature dependence of the quadrupole splitting

The quadrupole splitting increases with decreasing temperature and is related by a $T^{3/2}$ dependence. This arises from the temperature dependence of the electric field gradient created by both the surrounding lattice and valence electrons. The temperature dependence of both the lattice and electronic fields is mainly due to the thermal expansion of the crystal lattice and the influence of the created phonons on the conduction electrons[30,33]. The temperature dependent form of equation (2.34), gives the quadrupole splitting at a particular temperature T by the expression[35],

$$\Delta E_{\text{Q}} = \Delta E_{\text{Q,O}} \left[1 - \left(\frac{T}{T_{\text{K}}} \right)^{\frac{3}{2}} \right] \tag{2.38}$$

where $\Delta E_{\text{Q,O}}$ is the quadrupole splitting at 0 K, and T_{K} a constant. Both are fitting parameters.

2.5.3 Magnetic Dipole Interaction: Magnetic Splitting

A magnetic dipole interaction is observed if the nuclear states involves a magnetic dipole moment (μ) and a magnetic field ($\boldsymbol{B}$) is present at the nucleus, either produced by the surrounding electrons or ions present, or applied externally. This interaction leads to a precession of the magnetic moment about the field direction, which leads to a splitting of an energy level into $2I+1$ sub-states characterized by the magnetic spin quantum number m_I. A nuclear state with $I \geq \frac{1}{2}$ possesses a magnetic dipole moment and for ^{57}Fe, there exists magnetic dipole moments for both the ground state $I = \frac{1}{2}$, and the first excited state $I = \frac{3}{2}$. This effect leads to complete removal of the degeneracy of the nuclear levels, and thus the ground state with $I = \frac{1}{2}$ splits into two sub-states and the excited state with $I = \frac{3}{2}$ into four sub-states as depicted in Figure 2.8.

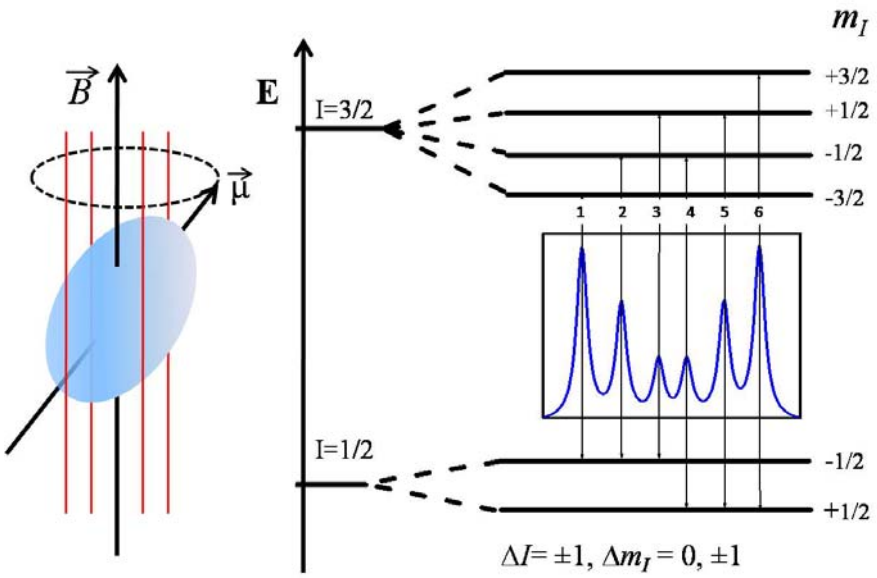


Figure 2.8: Effects of magnetic dipole interaction: magnetic splitting.

The splitting of the nuclear energy levels, equivalent in principle to the Zeeman Effect in atoms in optical spectroscopy is known as *magnetic splitting* or *nuclear Zeeman Effect*. The selection rules for magnetic dipole transition ($\Delta m_I = 0, \pm 1$) allowed for γ transitions between the sublevels leads to six possible transitions resulting in a sextet (six absorption lines) in the Mössbauer spectrum. The energies of the sublevels are given by the first order perturbation theory by,

$$E_M(m_I) = -g_N \mu_N \boldsymbol{B} m_I \tag{2.39}$$

where g_N is the nuclear Landé factor and μ_N is the nuclear Bohr magneton.

2.5.3.1 Relative Line Intensities

The linewidth of the six lines are in principle equal, but their intensities are very different. The intensity ratio of each line is found as the matrix element represented by the Clebsch-Gordon coefficients multiplied by the appropriate angular dependence between the direction of the γ-radiation and that of the magnetic hyperfine field[26,36]. For $I = \frac{1}{2} \rightarrow \frac{3}{2}$ in ^{57}Fe the intensity ratios are given in Table 2.1.

Table 2.1: Angular distribution of the relative intensities for the six allowed transitions in ^{57}Fe[15].

Line	Transition	Relative Intensity	Poly-Crystalline	$\boldsymbol{B} \parallel \gamma$	$\boldsymbol{B} \perp \gamma$
1 (6)	$\pm 1/2 \rightarrow \pm 3/2$	$3\left(1+\cos^2\theta\right)$	3	3	3
2 (5)	$\pm 1/2 \rightarrow \pm 1/2$	$4\sin^2\theta$	2	0	4
3 (4)	$\pm 1/2 \rightarrow \mp 1/2$	$1+\cos^2\theta$	1	1	1

For a thin absorber, the recoil-free fraction f is isotropic, and when the angle between $\boldsymbol{B}$ and the γ-ray is $\theta = 0$, the relative intensities of the six lines are in the ratio of 3:0:1:1:0:3. When $\theta = 90^o$, the ratio is 3:4:1:1:4:3. However, if the magnetic field vectors at the nuclei are randomly oriented, then the intensity ratio is 3:2:1:1:2:3.

2.5.3.2 Effective Magnetic Field

The magnetic hyperfine splitting allows for the determination of the size and direction of the effective magnetic field ($\boldsymbol{B}_{eff}$) acting at the nucleus. The effective magnetic field is given by the sum of the local magnetic field $\boldsymbol{B}_{loc}$ at the Mössbauer nucleus by the lattice and the hyperfine magnetic field $\boldsymbol{B}_{hf}$ of the Mössbauer atom's own electrons:

$$\boldsymbol{B}_{\text{eff}} = \boldsymbol{B}_{\text{loc}} + \boldsymbol{B}_{\text{hf}} . \tag{2.40}$$

The local field by the lattice may be attributed to the material's own magnetic ordering, and/or by an externally applied field or both. This local field may have the following contributions:

$$\boldsymbol{B}_{\text{loc}} = \boldsymbol{B}_{\text{ext}} - \boldsymbol{D}_{\mathbf{M}} + \frac{4\pi}{3}\boldsymbol{M}_{\text{m}} \tag{2.41}$$

where $\boldsymbol{B}_{\text{ext}}$ is an external field, $\boldsymbol{M}_{\text{m}}$ is the magnetization, $\boldsymbol{D}_{\mathbf{M}}$ represents the demagnetization field, and the $\frac{4\pi}{3}\boldsymbol{M}_{\text{m}}$ represents the Lorentz field.

Many materials can also create their own magnetic hyperfine field ($\boldsymbol{B}_{\text{hf}}$) and it has three contributions[27,29];

$$\boldsymbol{B}_{\text{hf}} = \boldsymbol{B}_{\text{F}} + \boldsymbol{B}_{\text{L}} + \boldsymbol{B}_{\text{D}} \tag{2.42}$$

where $\boldsymbol{B}_{\text{F}}$ is Fermi contact field, produced by the *s*-electron spin density and may be written as,

$$\boldsymbol{B}_{\text{F}} = -\frac{2\mu_{\text{o}}}{3}\mu_{\text{B}}\sum_{\text{n}}\left[\left|\psi_{ns\uparrow}(0)\right|^2 - \left|\psi_{ns\downarrow}(0)\right|^2\right] \tag{2.43}$$

where μ_{B} is the Bohr magneton and $\left|\psi_{ns\uparrow}(0)\right|^2$ and $\left|\psi_{ns\downarrow}(0)\right|^2$ represent the spin-up and spin-down electron densities at the nucleus, respectively. The difference arises as a result of the unpaired *d* electrons.

$\boldsymbol{B}_{\text{L}}$ is called the orbital field due to the orbital motion of unpaired electrons around the nucleus. This motion constitutes a circular current, which in turn produces a magnetic field at the nucleus:

$$\boldsymbol{B}_{\text{L}} = -\frac{\mu_{\text{o}}}{2\pi}\mu_{\text{B}}\left\langle r^{-3}\right\rangle\left\langle L_{\text{Z}}\right\rangle \tag{2.44}$$

where L_z is the *z*-component of the orbital angular momentum.

Finally, the third term $\boldsymbol{B}_{\mathrm{D}}$ is the dipole field at the nucleus produced by the total spin magnetic moment of the valence electrons and is given by the equation;

$$\boldsymbol{B}_{\mathrm{D}} = \frac{\mu_{\mathrm{o}}}{8\pi}\mu_{\mathrm{B}}\left\langle r^{-3}\right\rangle\left\langle 3\cos^2\theta - 1\right\rangle\left\langle S_Z\right\rangle \tag{2.45}$$

where S_z is the z-component of the spin angular momentum. It is obvious that $\boldsymbol{B}_{\mathrm{D}}$ is zero for a charge distribution with cubic symmetry. In general, the local magnetic field is much smaller than the hyperfine field.

2.5.4 Combined magnetic and quadrupole interactions

Often both the magnetic and the quadrupole splitting are present, resulting in a combined effect. The shape of the Mössbauer spectrum depends not only on the relative strengths of the two interactions but also the relative orientation of the EFG principal axis, the magnetic field and the incident γ-ray[27,29,36,37]. In most semiconductors, there is no internal magnetic field but an external one may be applied to understand some questions regarding the quadrupole interaction. However, when both interactions are present, closed form solutions for the splittings are possible when one interaction is weaker than the other[26].

Chapter 3

Experimental Details

3.1 Introduction

Over the past few decades, ion implantation[38-41] has shown to be a promising doping technique for semiconductor materials because of its ability to by-pass solubility and diffusion limits which exist in the conventional diffusion method. In addition, ion implantation offers some advantages already known from silicon technology[40], for example, nearly all elements of the periodic table can be introduced as dopants with precise control of depth distribution and concentration by varying the ion beam energy and fluence. In addition, the use of radioactive isotopes with short lifetimes as probe atoms in solids have significantly broadened the scope of solid state physics accessibility to Mössbauer spectroscopy.

This chapter introduces the principles of ion implantation and the production and use of radioactive ion beams at the ISOLDE Facility, CERN. The last part of this chapter focuses on the experimental details of Mössbauer emission spectroscopy which is utilized as a characterization technique for studying Fe impurity defects in GaAs and GaP.

3.2 Principles of Ion Implantation

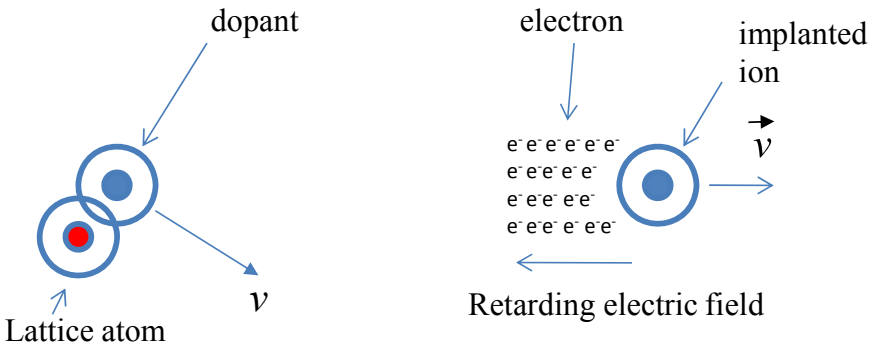
The introduction of impurity atoms or dopants into the near surface region of a substrate by direct bombardment of high energy impurity or dopant atoms is known as *ion implantation*. As these energetic ions travel in the material they lose energy or momentum through interactions with the target atoms (and their electrons) and finally come to rest. This section focuses on energy loss processes, and relevant parameters that influence damage formation and the final location of the dopants.

3.2.1 Ion stopping mechanisms

An energetic ion that enters a semiconductor surface begins to transfer energy to the bound electrons in the electron clouds of the host atoms (*electronic stopping*) and also lose energy or momentum mainly by elastic collisions with the target's lattice atoms (*nuclear stopping*)[39-46]

3.2.1.1 Electronic Stopping

The energy loss of a recoiling ion due to electronic processes arises from collisions between the electrons of the target atoms and the implanted ion as shown in Figure 3.1(a), resulting in excitation and possibly ionization of the target atoms[41]. The drag force due to the 'sea' of free electrons[42] also contributes to the slowing down of the implanted ion as depicted in Figure 3.1(b). These collisions are inelastic in nature and results in small energy losses in which the electrons are excited or ejected from their shells and dissipate their energy through thermal vibrations of the target. Electronic stopping dominates as the ions enter the semiconductor surface when the ion energy is relatively high.



(a) Elastic collision (b) Effect of drag force

Figure 3.1: Electronic stopping mechanism, due to (a) inelastic collision and (b) drag force from the electrons.

3.2.1.2 Nuclear Stopping

The nuclear stopping mechanism involves elastic collisions between lattice atoms and the recoiling dopant atom. Large amounts of energy are transferred during collisions resulting in significant angular displacements of dopants from their

trajectory and subsequent relocations of lattice atoms from their original sites, as illustrated in Figure 3.2. At very high energies, the nuclear energy loss is small due to the fast particles having less interaction time with scattering nucleus. Thus the nuclear stopping tends to dominate at the end of the range when the ions have lost most of their energy and spends more time in the vicinity of the lattice nuclei. Nuclear stopping is responsible for the formation of disruptions in the crystal lattice.

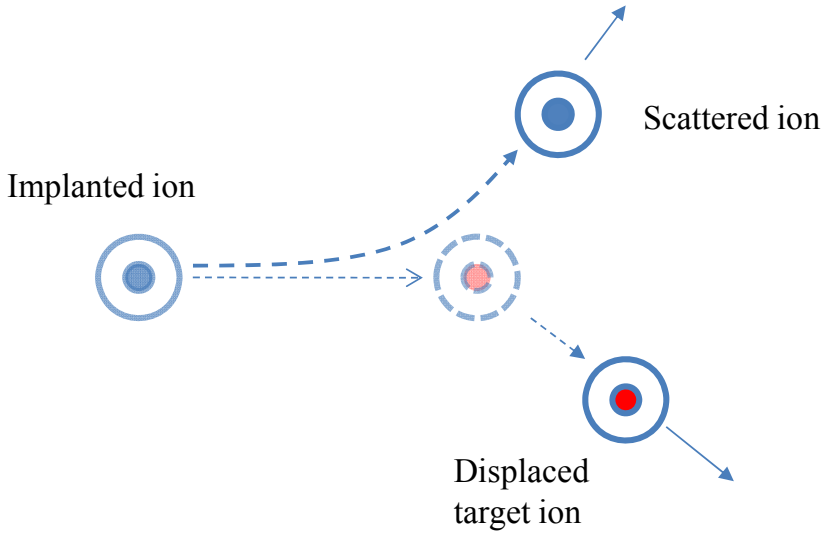


Figure 3.2: Nuclear stopping mechanism.

3.2.2 Total stopping power

The total energy loss of the dopant ion is given by the sum of the nuclear and electronic energy losses, a good approximation of which is given by the Lindhard-Scharff-Schiott (LSS) theory[41,43]. The total stopping power of the target is defined as the loss of energy per unit distance and given by the equation,

$$-\frac{dE}{dx}=N\left[S_n(E)+S_e(E)\right] \qquad (3.1)$$

where, N is number of target atoms per unit volume or the density of the atoms in the target materials, S_n is the nuclear stopping power and S_e is the electronic stopping power. In general, the nuclear stopping dominates at low energies while the electronic loss dominates at high energies. Figure 3.3 shows the dominance of the energy loss processes as a function of ion energy. S_n^o is an approximation for

the nuclear stopping potential and the ion energy when the electronic stopping contribution coincides with the nuclear stopping approximations; E_c is the *critical energy* which determines the dominance of the two major energy loss mechanisms with respect to the ion energy. When the ion energy is greater than E_c then the electronic stopping is the main energy loss mechanism while nuclear stopping dominates when the ion energy is less than the critical energy.

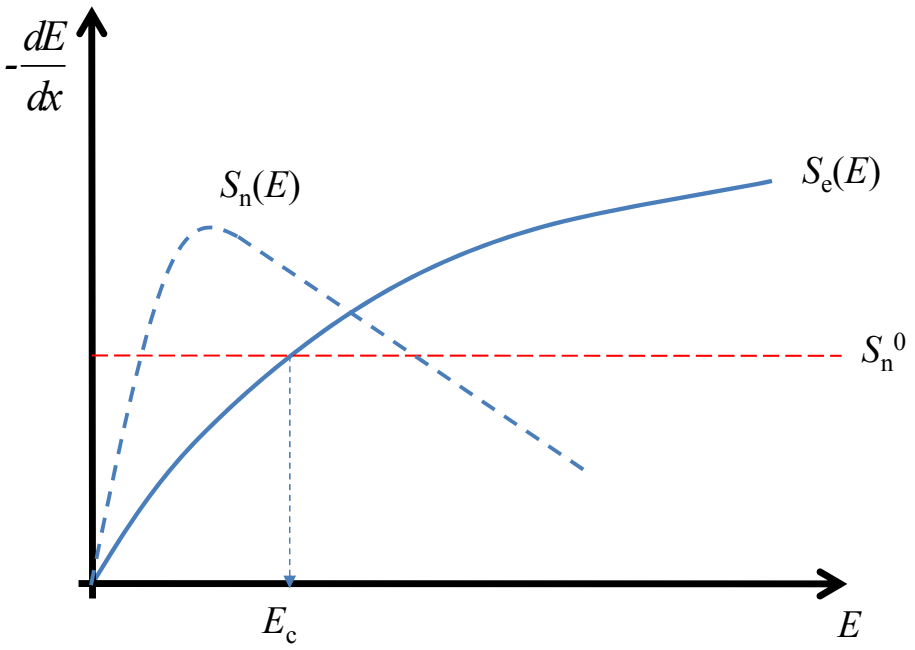


Figure 3.3: Theoretical estimates of nuclear stopping power (S_n) and electronic stopping power (S_e) variation as a function of ion energy.

3.2.3 Range and Distribution Profile

When ions enter the substrate they continuously lose energy and change direction due to collisions with target atoms. The random nature of the collisions implies that the total distance travelled (*range*) and its projection in the direction of the incident ion beam (*projected range*) are random variables as shown in Figure 3.4 (a). Some ions will stop at a depth smaller than the projected range and others at a depth larger than the projected range. Thus, there exists a distribution of ions about the projected range as illustrated in Figure 3.4 (b).

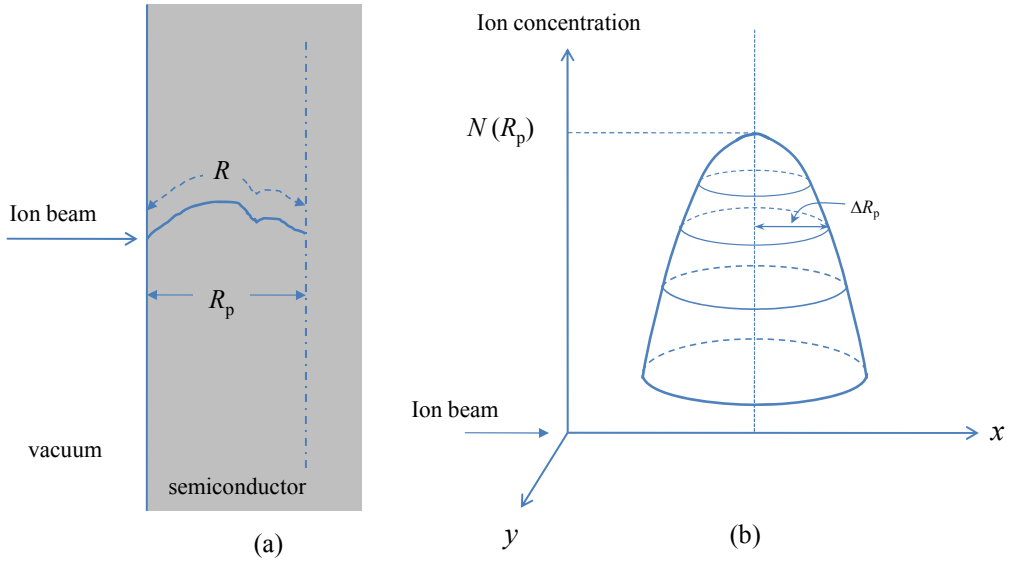


Figure 3.4: Ion depth and distribution profiles.

The implantation profile (projected ranges of a large number of ions) given by the LSS theory for an amorphous material can be approximated by a Gaussian distribution[9] due to the statistical nature of the ion stopping process as follows;

$$N(x) \approx N(R_p) \exp\left[-\frac{(x - R_p)^2}{\sqrt{2}\Delta R_p}\right] \tag{3.2}$$

where the peak doping concentration $N(R_p)$ is related to the dose (ϕ) by the expression:

$$N(R_p) = \frac{\phi}{\sqrt{2}\Delta R_p} \tag{3.3}$$

where the dose is controlled by the beam current, R_p is the projected range and ΔR_p is the straggle, which gives the variations in the projected ranges for different ions and thus describes the standard deviation in statistical terms. From equation (3.1) the range of the ions can be determined as follows;

$$R = \int_0^R dx = \frac{1}{N}\int_0^{E_0} \frac{dE}{S_n(E) + S_e(E)}. \tag{3.4}$$

3.2.4 SRIM2008 Simulation

Monte Carlo calculations were carried out to predict the final implantation depth and collision events for the implanted ions using the code SRIM2008[47]. This information was used to select the ion energy and sample thickness, and assists in understanding the nature of the created defects.

The distribution profiles of ^{57}Mn* implanted in GaAs and GaP are shown Figures 3.5 (a) and 3.5 (b) respectively. The calculations were conducted for a sample held at an angle of 60^{o} with respect to the beam line which resembles the actual experimental orientation. Figures 3.6 (a) and 3.6 (b) shows the target displacements, vacancies, and replacement collisions produced as result of the simulated implantation.

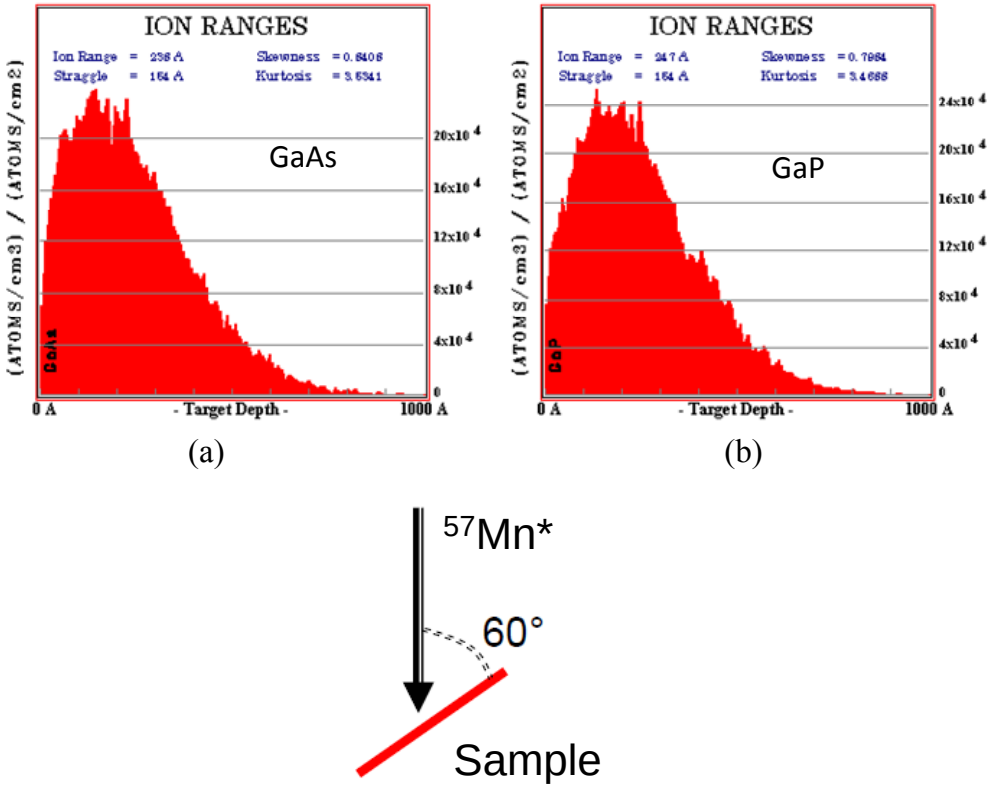
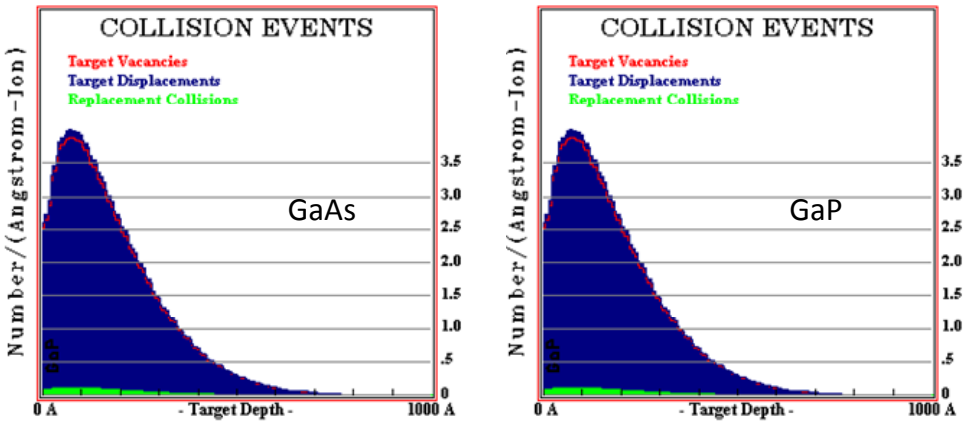


Figure 3.5: **Ion ranges distribution profile for 60 keV ^{57}Mn* implanted at an angle of 60^{o} into (a) GaAs and (b) GaP. The sample-beam experimental arrangement is depicted below the graphs.**



(a) (b)

Figure 3.6: Damage profiles for 60 keV ^{57}Mn* implanted at an angle of 60^{o} into (a) GaAs and (b) GaP.

The calculated projected range and straggle values for GaAs and GaP are displayed in Table 3.1.

Table 3.1: Projected range and straggle values for ^{57}Mn* implanted in GaAs and GaP.

	GaAs		GaP	
Projection	**Range (Å)**	**Straggle (Å)**	**Range (Å)**	**Straggle (Å)**
Longitudinal	238	154	247	154
Lateral	327	378	368	414
Radial	374	188	407	189

3.2.5 Implantation parameters

The damage produced as a result of the interaction between the implanted dopants, the local environment, and the final location of the dopants depends on a number of parameters and these include the ion energy, ion mass, implantation temperature, ion flux and fluence. The effects of these parameters are outlined below.

3.2.5.1 Ion energy

The ion energy determines the energy transferred to the crystal lattice through electronic and nuclear stopping. The larger the ion energy the greater damage is produced by nuclear energy loss which results in collision cascades. The density of these collision cascades depend on the ion mass.

3.2.5.2 Ion mass

The energy imparted to the crystal lattice is strongly determined by the mass of the implanted ion. When a light ion is incident on a substrate, small amount of energy is transferred to the lattice atoms during collisions. Moreover, because of its small mass, it is deflected by a large scattering angle by the relatively large lattice atoms. This results in an extended region with relatively less damage. However, for a heavy ion, at every collision a relatively large amount of energy is transferred to the lattice atoms resulting in displacements. The ion is deflected by a small scattering angle resulting in the majority of the damage confined to a small volume.

3.2.5.3 Implantation temperature

Intrinsic defects (vacancies or interstitials) may become mobile with increasing temperature, which allows for defect recombination within the primary collision cascades that reduces the damage after implantation. Moreover, the implantation at elevated temperatures is also connected to the change in defects types[44]. At high temperatures for low ion fluences, mainly point defects and point defect complexes are to be expected. However, for high fluence implantations, these may transform to complex structures resulting in a mixture of defect clusters and extended defects.

3.2.5.4 Ion flux

The number of ions implanted per unit area and time is known as ion flux. The ion flux determines the time between the two subsequent ion implants. This time is available for annealing of produced damage by the previous ion. The high ion flux may also locally raise the temperature of the material under study. Thus the effect

of ion flux on the formation of radiation damage is closely related to the implantation temperature and it is often hard to distinguish between the contributions of these effects[44]. The damage concentration increases with increasing number of ions impinging on a semiconductor surface per unit area and time.

3.2.5.5 Ion dose

The dose (or fluence), ϕ is the number of implanted ions per unit area (usually given by ions/cm^2). It is related to the beam current I_B by the formula:

$$\phi = \frac{I_B t}{q_i A} \tag{3.5}$$

where t denotes the implantation time, A the beam area and q_i is the charge per ion. Thus by controlling the beam current, the concentration profile of the implanted ions can be controlled. High fluences can lead to amorphization of the materials under investigations, however low fluences (below 10^{12} ion/cm^2) are applied to avoid non-overlapping damage cascades. The dose is given by the product of the ion flux and total implantation time.

3.2.6 Radiation damage

As the nuclear stopping dominates, a series of elastic collisions between the target atoms and the dopants occur before the dopants come to rest. When the energy of the implanted ion is higher that the lattice displacement energies, then the lattice atoms are displaced from their original site, leaving behind vacancies and formation of interstitial defects. Below room temperature, the atoms are unable to move far through the lattice so local relaxation occurs to accommodate them. At high temperatures, the displaced atoms can diffuse into empty lattice sites and repair the damage or coalesce together to form extended defects[44]. However, with radioactive implantations, if the daughter atom has recoil energy greater than the displacement energy, further collisions will occur resulting in more relocations and lattice dislocations. This disturbance of the periodic order of the lattice atoms in crystalline materials due to the implantation is known as *radiation damage*.

3.2.7 Annealing

Ion implantation has several advantages over diffusion as discussed, however it is a destructive method because of the radiation damage. Dopants come to rest on interstitial positions or form substitutional and/or impurity-vacancy complexes where they will not be charge carriers. Sometimes, if the damage is extreme then amorphization of the semiconductor surface may occur[48]. *Annealing* usually follows the implantation process to remove the defects either partially or completely. This is a high temperature treatment process of the implanted semiconductor surface for the dopants to diffuse to a substitutional site where they become electrically active. Annealing also promotes crystallization of the amorphous materials. However, if the implantation is done at elevated temperatures, the formation of amorphous layers is inhibited and high substitutional fractions may be observed in many cases[38,44]. Continuous stepwise annealing at different temperatures prevents the build-up of high levels of radiation damage.

3.3 Mössbauer emission spectroscopy at ISOLDE

Mössbauer emission spectroscopy using radioactive probe atoms presents a novel method of utilizing the sample under study as the source of γ-rays. Mössbauer emission spectroscopy utilizing radioactive precursor isotope ^{57}Mn* ($T_{1/2}$ = 1.5 min) produced at the ISOLDE Facility as implantation probe atoms, which β^- decays to ^{57}Fe are used for studying defects in GaP and GaAs. Figure 3.7 shows the layout of the ISOLDE Facility and the ^{57}Mn* Mössbauer spectroscopy experimental site at the General Low Mass (GLM) beam line.

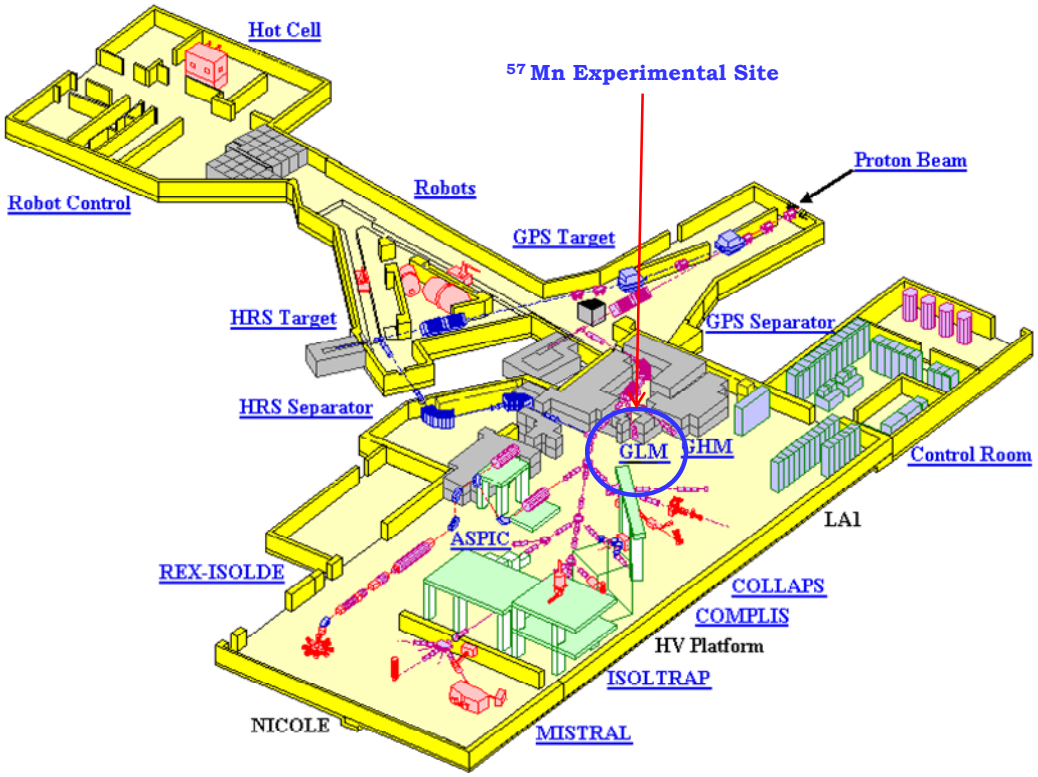


Figure 3.7: The ISOLDE Facility layout[4].

3.3.1 Beam production at ISOLDE

^{57}Mn* radioactive ion beams are produced at the ISOLDE Facility, using a 1.4 GeV proton-induced nuclear fission in a uranium carbide (UC_2) target. ^{57}Mn atoms are subsequently ionized by a multi-frequency element specific laser irradiation system[4,26,49] (see Figure 3.8) and at the same time ^{57}Fe contaminants of up to 10^{10} ions/s in the beam[50] are removed. The singly charged ions are then

accelerated to an energy of 60 keV before they are mass separated by magnets to produce pure radioactive ^{57}Mn* ion beams with intensities $\geq 10^{8}$ s^{-1}, and are then directed to the implantation chamber. A beam spot area of 0.3 cm^{2} corresponds to a flux of 6.2×10^{8} ^{57}Mn*/(cm^{2}s).

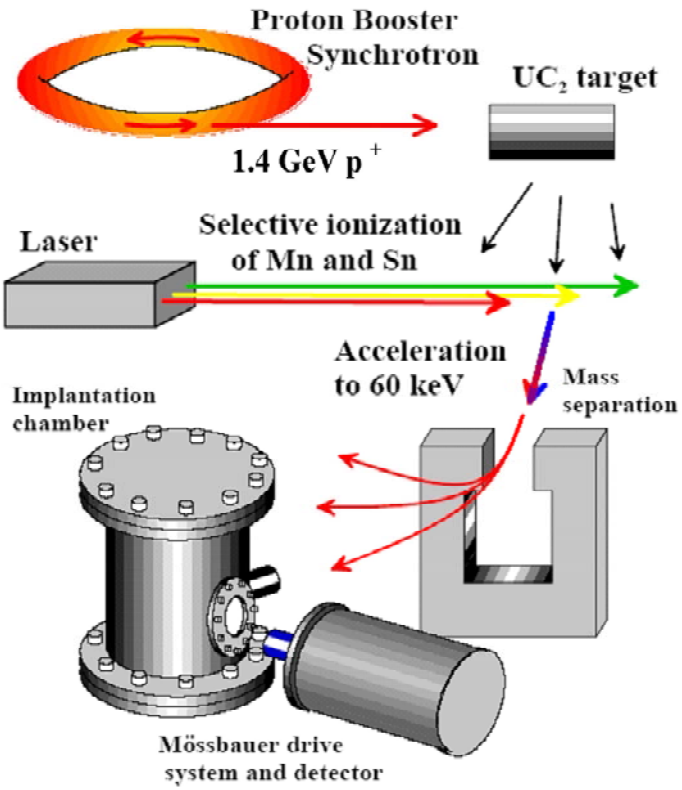


Figure 3.8: Beam production at ISOLDE[51].

3.3.2 Experimental set-up

The ultra-high vacuum (UHV) implantation chamber is connected by soft bellows to the ^{57}Mn* beam-line system and is pumped to 10^{-6} mbar. For low temperatures (77-300 K) a liquid N_2 cryostat system is connected to the chamber[17]. A single sample holder is used for low temperature measurements as shown in Figure 3.9 (a). For high temperatures (300 – 700 K) a sample holder consisting of 4 sample positions (see Figure 3.9 (b)) is used to enable a series of measurements without breaking the vacuum. In the initial measurements, two sample holders positions were dedicated for beam alignment and calibration purposes. For example, in Figure 3.9 (a), an empty sample position 3 is used for beam

alignment. A beam of ^{57}Mn* is directed through position 3 towards a Faraday cup to optimize the beam current which is achieved by varying the beam steering parameters on the ISOLDE console. The Faraday cup is designed to collect charged particles in vacuum, hence the number of ^{57}Mn* ions striking the cup can be used to determine the beam current.

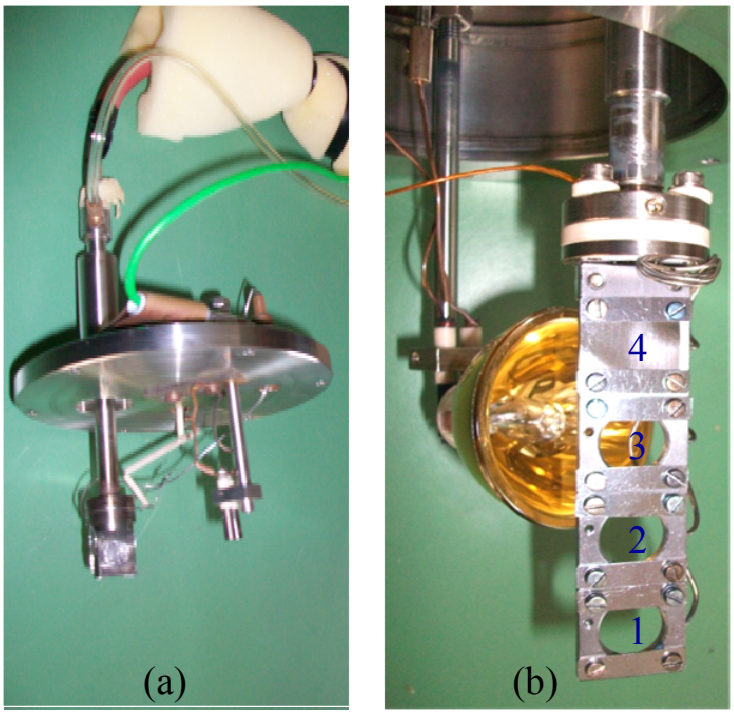


Figure 3.9: **(a) Single sample holder for low temperature measurements and (b) Four position sample holder equipped with annealing system for high temperature measurements.**

The sample position 4 is used for calibration. All hyperfine parameters are determined relative to α-Fe spectrum measured at room temperature. An Osram halogen photo-optic lamp (15 V, 150 W) incorporated in the implantation chamber provides a rapid thermal annealing system with a temperature range up to 800 K. Figure 3.10 shows a picture of the experimental Mössbauer emission spectroscopy set-up at the ISOLDE beam line. A beryllium window is placed on the UHV implantation chamber facing a detector and acts as a filter for any radiation other than the 14.4 keV γ-rays. The parallel-plate avalanche counter[52] (PPAC) detector is mounted on an electromagnetic drive system providing the Doppler velocity to record Mössbauer spectra of the emitted γ-radiation. The

beam current of ^{57}Mn* is relatively low compared to stable beams, hence efficient PPAC detectors are used in data acquisition. They are fast and insensitive to γ or X-ray background radiation, i.e. the signal to background ratio is high[17]. In addition, they have a relatively high time resolution in the order of nanoseconds (10^{-9} s) and thus high count rates can be tolerated. The detector is an acetone gas-filled (pressure of 40 mbar) resonance counter equipped with enriched stainless steel on beryllium disks which acts as electrodes.

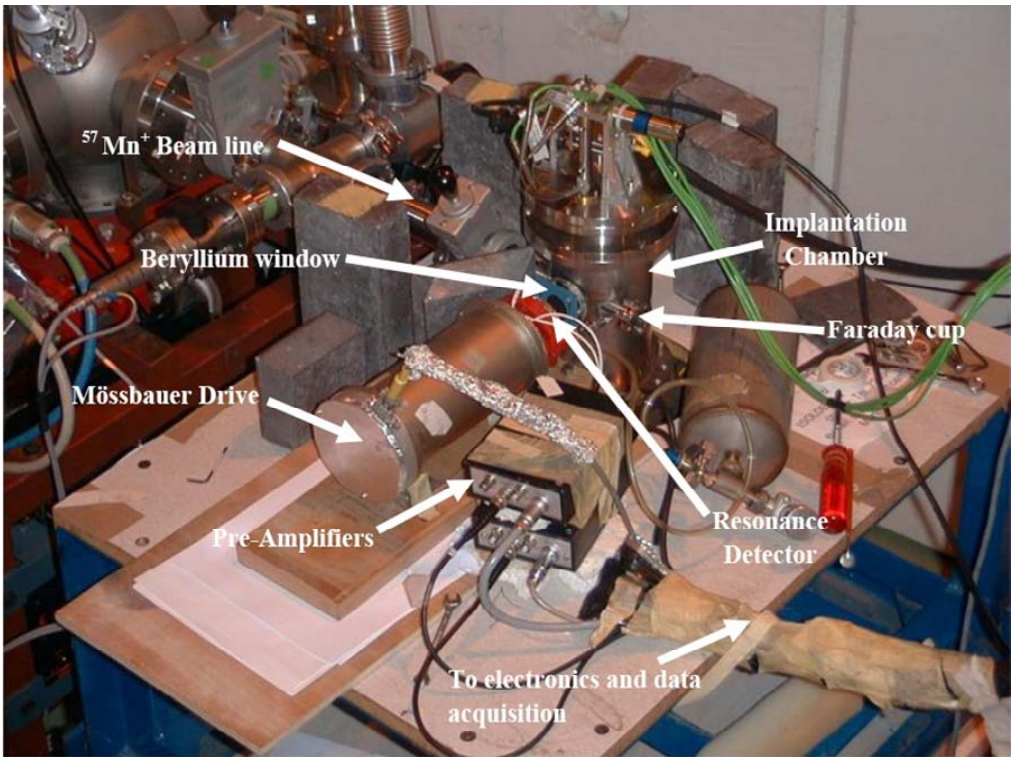


Figure 3.10: Experimental set-up for Mössbauer Spectroscopy at ISOLDE.

The pulses from the detector are pre-amplified, then amplified and then passed through a single channel analyzer (SCA) or discriminator where most of the non-resonant background radiation is not detected. The discriminated pulses are finally fed into a multichannel analyzer (MCA) where several hundreds of channels are synchronized with the velocity of the Mössbauer drive unit (MDU) making use of the feedback control system through the function generator (FG). The FG supplies a reference signal which determines the waveform of the source. Apart from the analogue signal, the FG also provides two digital control pulses

(*Start* and *Channel Advance – CHA*), which are used to synchronize the MCA. The *Start* pulse resets the MCA and opens the first data register to receive the counts. Any pulses from the SCA which arrive while the register is open are added to the current contents. When each successive *CHA* pulse arrives, the current register is closed, and the next one opens[36]. In this way, the arriving pulses are placed in a register that corresponds to a specific drive velocity. When the complete waveform has been generated (usually 512 channels), a new *Start* pulse is sent and the cycle repeats. The MCA is typically a card incorporated inside a computer, which provides data storage and spectra display. The experimental set-up and the electronics for Mössbauer spectroscopy at ISOLDE are shown in Figure 3.11.

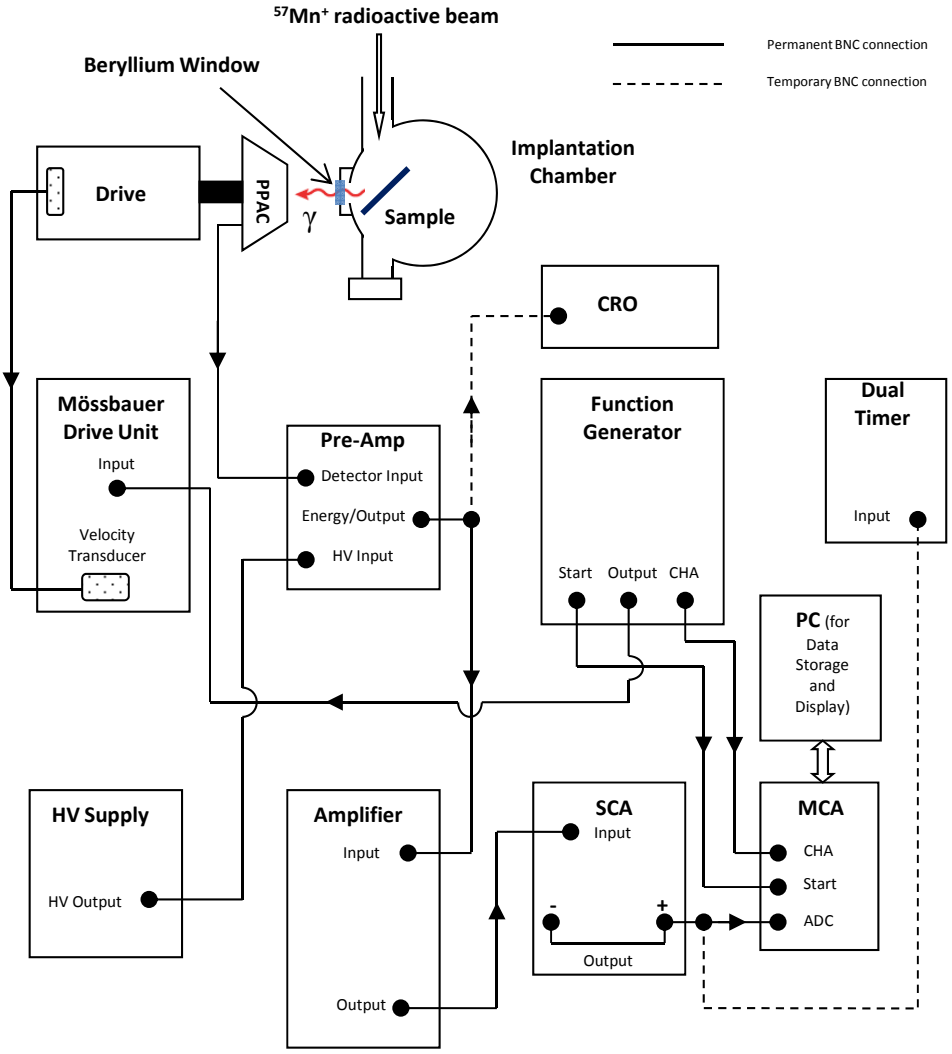


Figure 3.11: Schematic diagram for experimental set-up and electronics.

3.3.3 Samples and measurements

The host materials, used in this project were undoped GaAs and GaP single crystals which were grown by Molecular Beam Epitaxy (MBE). The dimensions of each sample were 0.3 x 10 x 10 mm^3. The sample holder is placed at an angle of 60^o with respect to the beam line. The 60 keV ^{57}Mn* ions were implanted at ambient temperatures with fluences less than 10^{12} ions/cm^2 into the materials under study. Following implantation, low temperature (77 K) measurements and measurements during an annealing sequence (300 – 700 K) were then performed. The low fluences were employed to ensure that graphitization effects and overlapping damage cascades are effectively ruled out. The half-life of $^{57}Mn^*$ (1.5 min) is sufficient to allow for the annealing of the implantation radiation damage to occur at increasing temperatures, before Mn decay and subsequent measurement of the ^{57}Fe Mössbauer spectra. The excited $^{57}Mn^*$ state β^- decays directly to the 14.4 keV state of ^{57}Fe with 80% probability by emitting an electron. A mean recoil energy of 40 eV is imparted to the ^{57}Fe atoms[49]. Figure 3.12 shows the decay scheme of ^{57}Mn*.

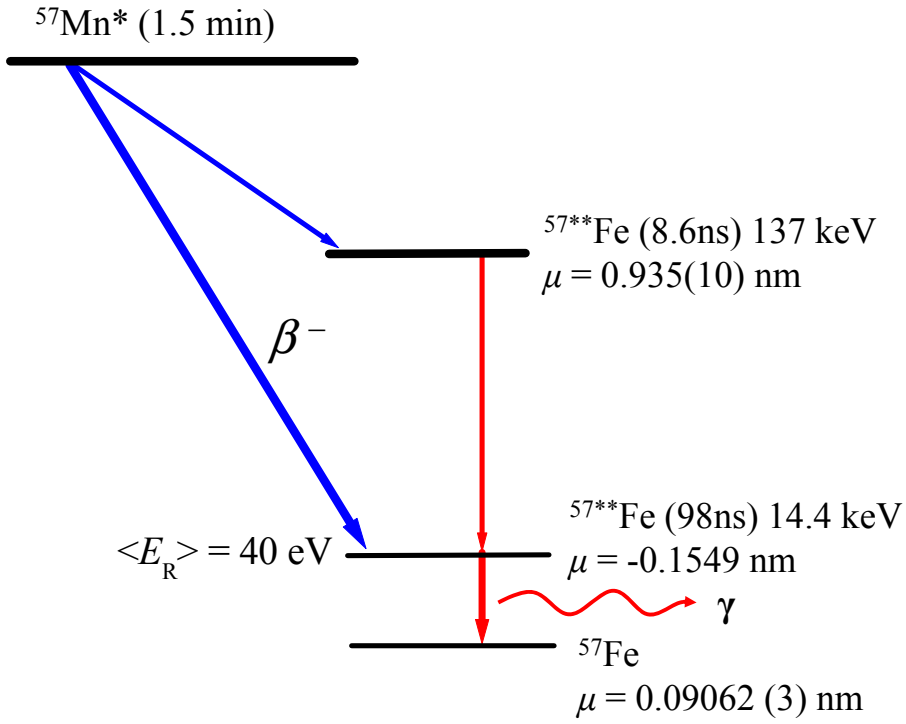


Figure 3.12: The ^{57}Mn* Decay scheme[49].

3.3.4 The Mössbauer Spectrum

A Mössbauer emission spectrum is measured by detecting the resonant absorption of the γ-radiation emitted in the transition to the groundstate of the radioactive probe nucleus in the sample material (source) by a stable nucleus of the isotope in a suitable absorber material[26]. In back-scatter geometry, the resonance absorption is detected by an increase in the count rate at the resonant velocities. Hyperfine interactions will shift the nuclear energy levels and/or split them into sublevels. In order to observe resonance between the source and the absorber, a γ-ray with variable energy is required. This is achieved by moving the absorber (detector) relative to a stationary source (sample) thus modulating the γ-ray energy by the Doppler Effect. The level of resonant absorption at each velocity is determined by the how much of the shifted absorption energy profile overlaps with the relatively stationary energy profile spectrum. The greater the overlap, the higher the intensity of the resonant absorption line as illustrated in Figure 3.13 which shows the development of a Mössbauer spectrum.

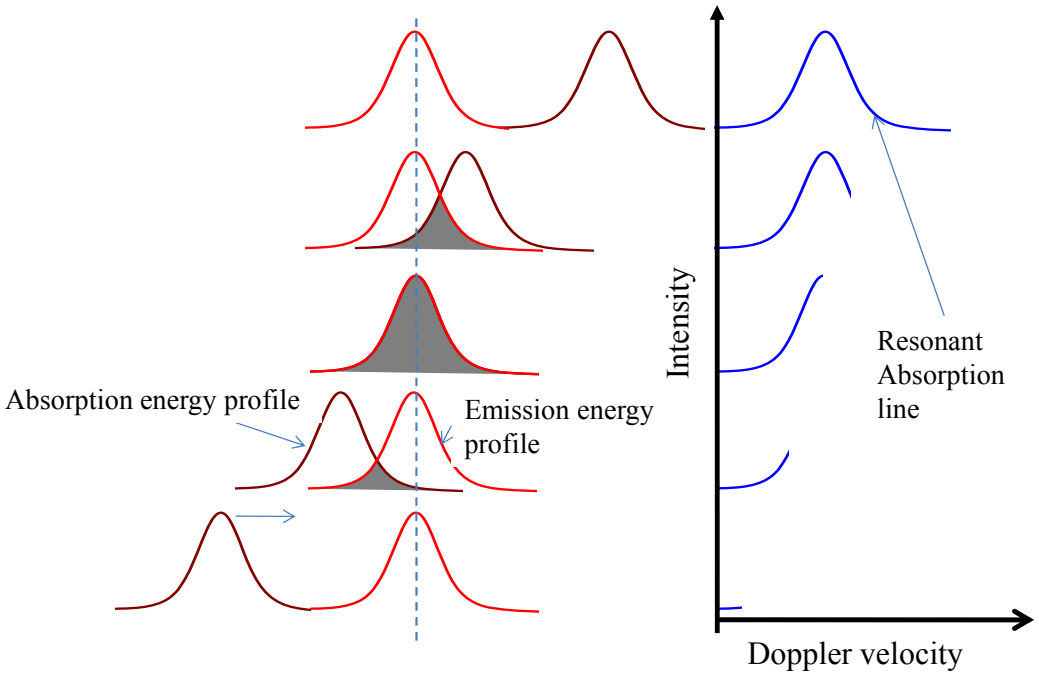


Figure 3.13: Development of a Mössbauer emission spectrum.

The velocities for resonant absorption and the overall shape of the spectrum are determined by the combined effect of the hyperfine interactions which depends on

the environments of the Mössbauer atoms. The area under a particular spectral line in an analyzed Mössbauer spectrum gives the intensity of the line [31]. This is proportional to the *f* factor and to the population of the lattice site belonging to the particular line. The area under a given line *i* is given by:

$$A_i(T) = A_o p_i(T) f(T, \theta_D) \tag{3.6}$$

where A_o is the initial spectrum area. This spectral area is dependent on the set up parameters such as the thickness of the beryllium window, the recoil-free fraction, and the population, p_i of a particular lattice site assigned to the line *i*. The sum of the population of sites,

$$\sum_{i=1}^{n} p_i = 1 \tag{3.7}$$

must hold during the annealing series, where *n* is the number of spectral lines. Figure 3.14 shows a typical Mössbauer emission spectrum with fitted components for different lattice sites.

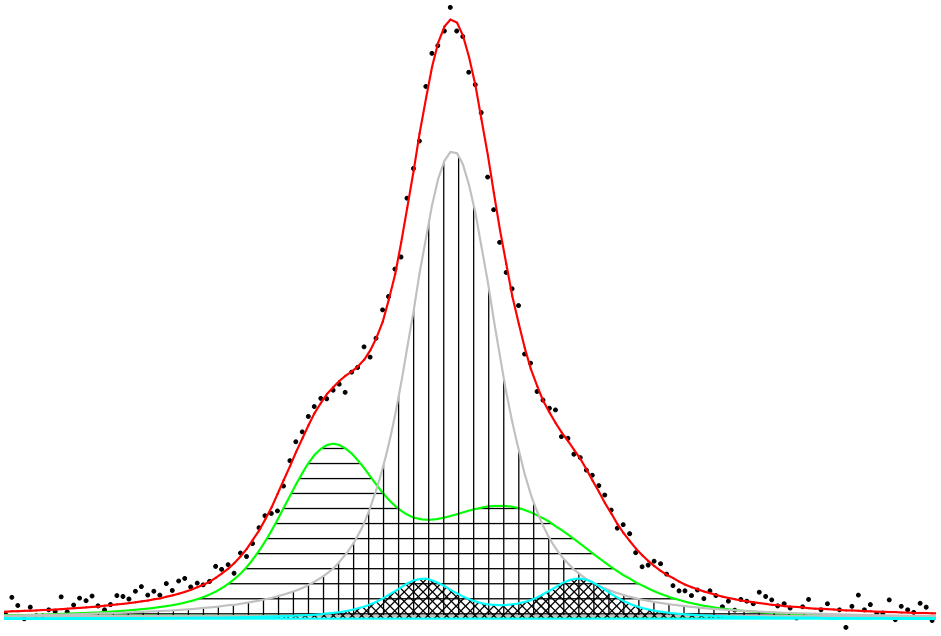


Figure 3.14: A typical Mössbauer emission spectrum fitted with 3 components for the Mössbauer nucleus in different lattice locations.

Thus, relative *f* factors and hence Debye temperatures for the different lattice sites can also be determined from implantation and annealing series of spectra.

3.3.5 Advantages of $^{57}Mn^{*}$ Mössbauer Emission Spectroscopy (MES)

Mössbauer emission spectroscopy using radioactive probe atoms presents a unique approach of utilizing the sample under study as the source of γ-rays. This technique has considerable advantages over conventional Mössbauer spectroscopy (CMS), conversion electron Mössbauer spectroscopy (CEMS) and in-beam Mössbauer spectroscopy (IBMS) using recoil implanted ^{57}Fe, which are listed below:

1. Novel technique of using the sample as source offers high sensitive measurements from which atomic level information about the 'destiny' of the daughter atoms can be determined, i.e. their lattice location and microscopic environments.
2. Radioactive beams produced at ISOLDE have high purity and intensity, and also the energy of the beam is tunable, which helps in determining the projected range of implanted ions.
3. Short-lived radioactive isotopes ($T_{½}$ = 1.5 min for $^{57}Mn^{*}$) reduces the data acquisition time by orders of magnitude with respect to standard methods. For example, it takes an average of 10-14 days to record a spectrum with good statistics using conventional Mössbauer spectroscopy with a ^{57}Co source, and approximately 24-36 hrs with IBMS, while it takes about 10 minutes to measure the same spectrum using radioactive isotopes with short half-lives like ^{57}Mn.
4. The parallel-plate avalanche counter based gas resonance detectors are more efficient in data acquisition as they have a high signal to background ratio and a relatively high time resolution in the order of nanoseconds (10^{-9} s). This efficient detection system produces exceptionally high count rates, up to 9500 counts/sec which is much superior compared to CMS and CEMS.

Mössbauer spectra can also be recorded using a resonance detector equipped with four 150 nm thick α-^{57}Fe layers. The detection efficiency and resolution coupled with the internal calibration of the spectra makes this detection method superior as compared to stainless steel resonance detector technique. However, the α-Fe

detection system results in a rather complicated six-fold emission spectrum which can be transformed into a single line emission feature. The stainless steel detector used in this work resulted in emission spectra with broad structure and the fitting of spectral components were carried out carefully by applying simultaneous analysis. The calibration procedure is outlined in the next section.

3.4 Calibration of Mössbauer Spectra

As mentioned earlier, the most common method of calibration is to use an α-Fe foil at room temperature. All line shifts are determined with respect to the centre of the α-Fe spectrum which serves a good reference. The velocity profile during a single period is shown in Figure 3.15 which results in a spectrum being recorded twice in the 512 channels of the MCA. This is illustrated in Figure 3.16.

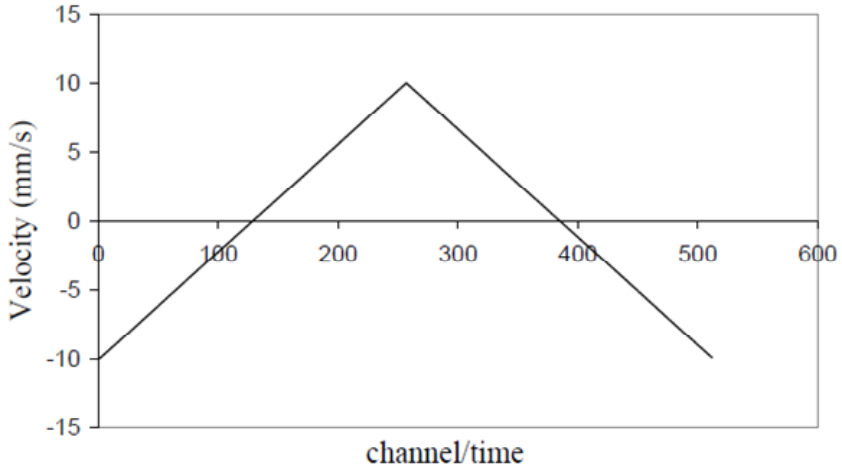


Figure 3.15: Source velocity as a function of channel number.

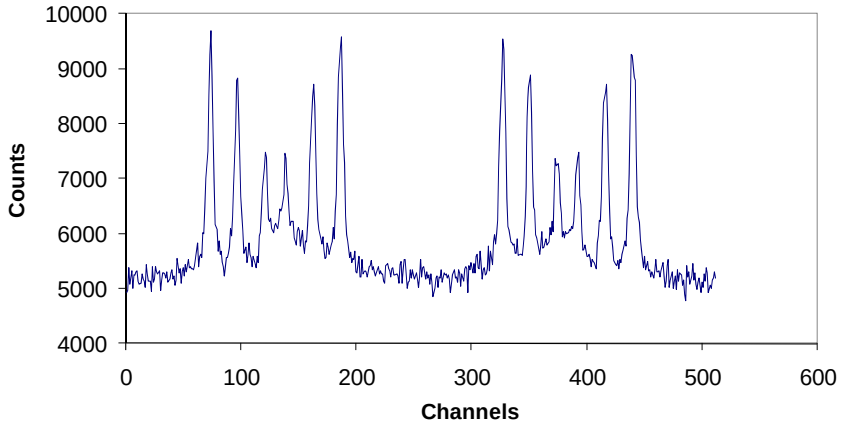


Figure 3.16: Unfolded spectrum of α-Fe.

The initial task of the calibration process was to fold the two halves of the spectrum shown in Figure 3.16 to obtain a single spectrum. Thus the number of channels is reduced to 256 and the statistical noise is then minimized. The α-Fe foil gives a six-line spectrum after folding where the centre of the spectrum is chosen as zero velocity. The rest of the calibration procedure was to find a transformation of the channel numbers to velocities. This was achieved by determining the numbers C and z so that

$$v_i = C(i - z) \tag{3.8}$$

where C is the calibration constant, z is the zero velocity and i the channel number. The final folded spectrum is depicted in Figure 3.17.

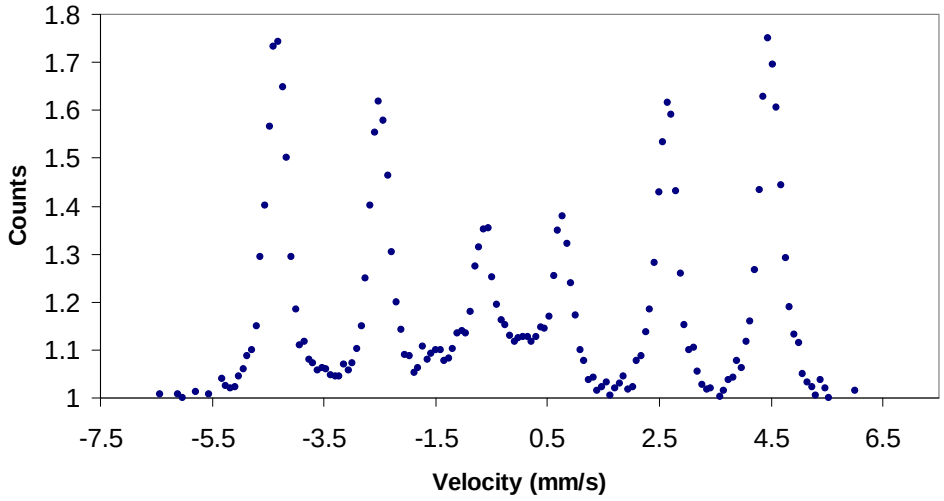


Figure 3.17: Folded spectrum of α-Fe.

These numbers are obtained so that the data fits the theoretical spectrum of α-Fe, which by definition [37] has a $\boldsymbol{B}_{hf}$ of 32.9 T, a quadrupole shift of zero and an isomer shift of zero. The isomer shift of a quadrupole doublet is known as the quadrupole shift which is obtained from the center of the peaks relative to the zero calibration.

3.5 Data analysis

In order to obtain reliable microscopic information from Mössbauer measurements, it is essential to analyze the experimental data[29]. Usually after implantation, the probe atoms are located on several lattice sites with different

hyperfine parameters resulting in very complicated spectra. The analysis involves least-square fitting procedure using Lorentzian lines or Voigt line shapes (Lorenzian line with Gaussian broadening). The fitting is eased by known constraints for the hyperfine interaction splittings and the temperature dependence of the second-order Doppler shift[17]. The experimental data obtained in this study was analyzed using software package called Vinda[53] which was developed by one of our collaborators, H. P. Gunnlaugsson. Vinda is essentially a toolbox which works in Microsoft Excel environment where all the commands are contained in a toolbar that runs Visual Basic for Applications (VBA) macros. The summary of different models applied to give reasonable and consistent results in the data analysis is presented in Appendix A while a summary of the fitting procedure using Vinda is described in Appendix B.

Chapter 4

Results and Discussion

This chapter focuses on the analysis and interpretation of the data obtained from Mössbauer spectroscopy investigations following ^{57}Mn* implantation into GaAs and GaP single crystals. The first two sections of this chapter presents the results of these materials under study with special attention given to the structural changes observed in the spectra with increasing temperature. The Mössbauer hyperfine parameters extracted from the analysis procedures are discussed within each section. Subsequent sections present similarities and differences between results obtained for GaAs and GaP, discussion on charge states and comparison with different precursor ions used for implantation in the same materials.

4.1 Data analysis and interpretation of Fe in GaAs

Figure 4.1 shows ^{57}Fe Mössbauer spectra collected after ^{57}Mn* implantation into GaAs single crystal held at temperatures between 77 – 650 K. The data over the entire temperature range were fitted simultaneously using the code Vinda with several models consisting of combinations of single lines and quadrupole split components (see Appendix C). Best acceptable fits were obtained with: (i) an asymmetrically broadened doublet (D1) which dominates the spectra at temperatures < 550 K, (ii) a single line (S1) which dominates at temperatures ≥ 550 K, (iii) a symmetric doublet (D2) present over the measured temperature range, and (iv) a single line (S2) with a low intensity only present at 77 K.

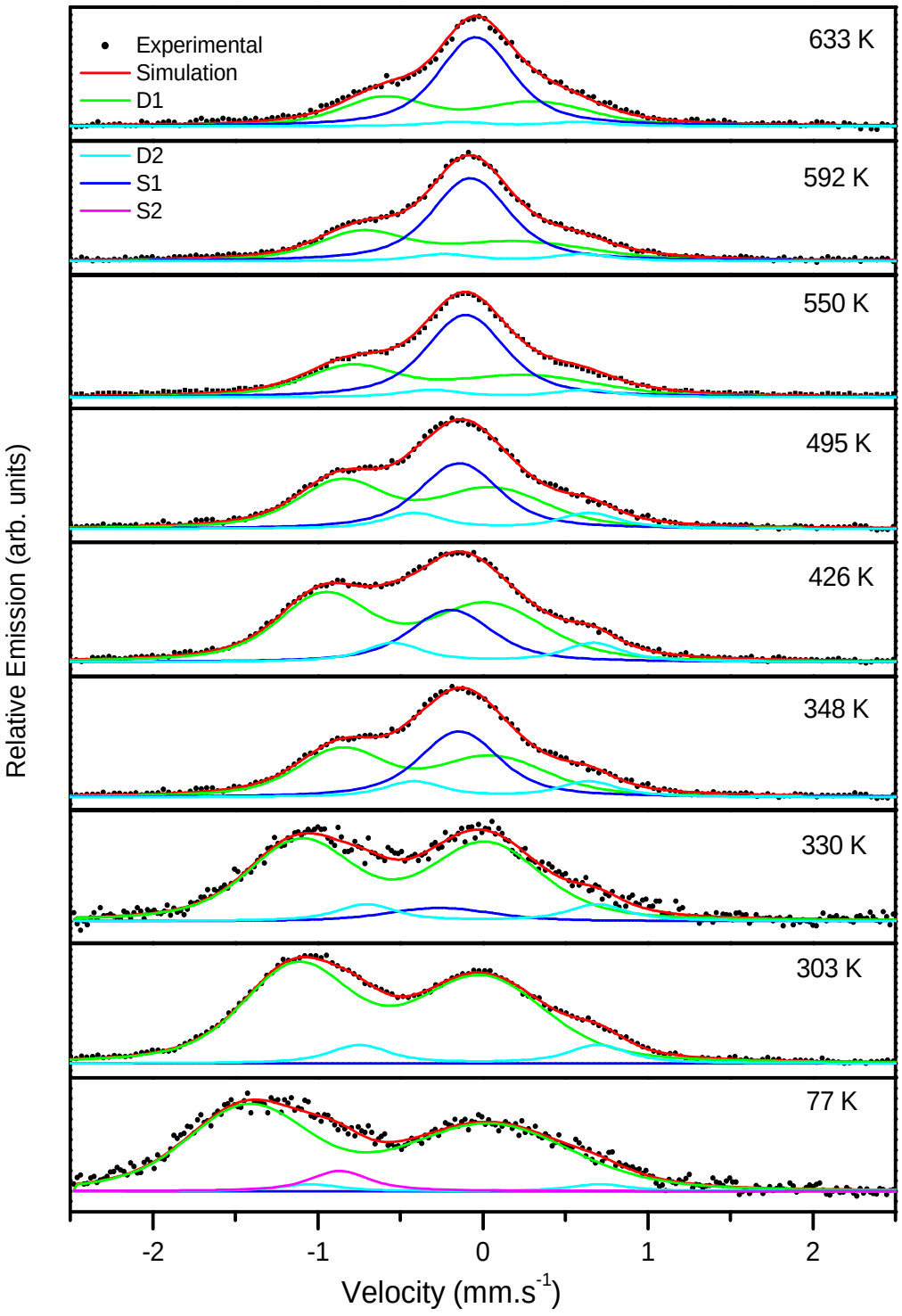


Figure 4.1: **^{57}Fe Mössbauer spectra obtained after ^{57}Mn* implantation into GaAs single crystal held at the temperatures indicated.**

Table 4.1 shows the extracted hyperfine parameters at room temperature and the Debye temperatures for the different lattice sites.

Table 4.1: Hyperfine parameters obtained at room temperature for GaAs.

	δ (mm.s^{-1})	ΔE_Q (mm.s^{-1})	$\sigma(\delta)$ (mm.s^{-1})	$\sigma_L(\delta)$ (mm.s^{-1})	$\sigma_R(\delta)$ (mm.s^{-1})	θ_D (K)
D1	0.57(5)	1.12(1)	-	0.25(5)	0.31(7)	302(32)
D2	0.02(2)	1.44(3)	0.08	-	-	268(6)
S1	0.28(4)*	-	0.23-0.13	-	-	275(4)
S2	0.87(2)+	-	0.08	-	-	-

* Determined from a higher temperature [NB: at 359 K, δ = 0.261 mm.s^{-1}]

+ Isomer shift at 77 K,

Previous ^{57}Fe Mössbauer spectroscopy utilizing ^{57}Mn* implantation has yielded a wealth of information on the behavior of Fe in different semiconductors such as Si[54-59], Ge[60], SiGe[61,62], SiC[35,63] and diamond[64,65]. Moreover, in-beam Mössbauer spectroscopy using recoil implanted ^{57}Fe, has also been applied to investigate lattice locations in semiconductors, for example in diamond[66]. Table 4.2 shows the extracted hyperfine parameters of a few group IV elemental semiconductors which were analyzed using similar components.

Table 4.2: Hyperfine parameters obtained at room temperature for diamond, Si and Ge.

	Fe_S	Fe_D		Fe_I	Fe_N	
	δ (mm.s^{-1})	δ (mm.s^{-1})	ΔE_Q (mm.s^{-1})	δ (mm.s^{-1})	δ (mm.s^{-1})	ΔE_Q (mm.s^{-1})
Diamond	-0.91 (2)	-0.20 (1)	2.10 (2)	0.22 (5)	-1.2 (2)	~ 4.3 (4)
Si	-0.06(2)	0.25 (2)	1.10 (3)	0.76 (2)	0.47 (1)	< 0.3
Ge	0.06 (2)	0.46 (2)	1.15 (3)	0.80 (2)	0.46 (1)	0.56 (2)

Fe atoms have been found to occupy substitutional (Fe_S) sites, interstitial (Fe_I) sites, and were also located in distorted environments due to radiation induced damage (Fe_D) as reflected in Table 4.2. In addition, a component assigned to Fe-substitutional or Fe-interstitial vacancy complexes was included in the analysis. The lattice site assignments of the fitted components in GaAs are

discussed in the following section with reference to the known behavior from the cited experimental work in other semiconductors[37,54-66].

4.1.1 Assignments of fitted components in GaAs.

In group III-V semiconductors, Fe has two possible substitutional sites, namely, III site or V site. Fe atoms are expected to occupy the III or Ga sites. The Ga site is preferred because Fe tends to lose three electrons to form sp^3 hybrid orbitals resulting in the similar tetrahedral coordination as in cubic III-V semiconductors. A good substitution site would have zero quadrupole splitting signifying cubic environments in the neighborhood of the Mössbauer atom. Moreover, Fe atoms can also be located in interstitial positions where they are not involved in any bonding with the host lattice atoms. There are three potential interstitial sites; namely two tetrahedral sites, either surrounded by four group III or V atoms and the hexagonal site. Generally, a relatively high isomer shift value is expected for impurity atoms in interstitial positions resulting from high electron density at the nucleus. Interstitials and a larger number of vacancies are formed when the Mn atoms collide with the lattice atoms during implantation causing displacements from their original lattice sites. Moreover, in the nuclear transition $^{57}Mn^{*} \rightarrow {}^{57}Fe^{*}$, an average recoil energy of 40 eV is imparted to the ^{57}Fe daughter atom[17], which is greater than the threshold displacement energy, E_d ~20-25 eV. This leads to the relocation of a significant fraction of the daughter Fe atoms from the initial location of the parent ^{57}Mn atoms. In addition, due to implantation radiation, Fe atoms can be found in highly distorted surroundings which are characterized by predominant quadrupole split doublets in the spectra, i.e. in sites of non-cubic point symmetry. Furthermore, Fe atoms can also be found embedded in defect structures such as substitutional or interstitial-vacancy complexes. However, fluences below 10^{12} ions/cm^2 were used to assure non-overlapping damage cascades.

The asymmetric doublet D1 is assigned to the damage site (Fe_D) attributed to Fe atoms located in small amorphous pockets, resulting from the implantation radiation damage. The single line S1 which dominates the spectra at temperatures

above 550 K, and upon annealing shows the impurity atoms are normally stable at substitutional sites. This is assigned to Fe atoms on substitutional Ga sites (Fe_S) in cubic environments as indicated by the zero quadrupole splitting. This assignment is consistent with Mössbauer measurements on ^{119}Sn implanted GaAs where the observed spectra at high temperature implantations were dominated by a single line component assigned to Sn on substitutional Ga sites[8-10]. The absence of the Fe_S component at low temperatures is probably due to the fact that this site forms upon annealing of the lattice damage, when some interstitials and/or vacancies become mobile. A higher isomer shift of the Fe_D component (δ = 0.57 mm.s^{-1}) corresponds to an increase in the electron density at the nucleus, relative to the Fe_S component (δ = 0.28 mm.s^{-1}) which suggests some relaxation of the surrounding lattice in the small amorphous pockets. An extremely high electron density is characteristic of the single line S2 (δ = 0.87 mm.s^{-1}) relative to the Fe_S component and this indicates that some Fe impurity atoms might be in interstitial positions (Fe_I) without bonding to the nearest neighboring atoms. The identity of the low electron density symmetric doublet D2 (discussed later) is associated with Fe atoms in distorted surroundings as predicted by the hyperfine parameters.

4.1.2 Debye Temperatures of lattice sites in GaAs

The areal fractions of the various sites obtained from simultaneous fitting were assumed to follow the Debye model and was used to determine the Debye temperature (θ_D) of the different lattice sites. The extracted Debye temperature value of 268(8) K for the D2 component is very similar to the value of 275(4) K obtained for the substitutional component (Fe_S). Thus the D2 is assigned to near substitutional impurity atoms associated with adjacent vacancies in impurity-vacancy complexes (Fe_N). However, the Fe atoms in the damaged sites are assigned to near substitutional Fe atoms due to their relatively close Debye temperatures (θ_D = 302 K for Fe_D and θ_D = 275 K). The large quadrupole splitting value of the Fe_D (ΔE_Q = 1.12 mm.s^{-1}) implies that the Fe_D atoms in the damaged sites are in non-cubic environments. Moreover, a similar coordination with nearest

neighbors to Fe on substitutional sites is envisaged for Fe atoms in the damaged sites.

To obtain reasonable fits without increasing the number of components, Fe_S is represented as a single line whose broadening decreased from 0.23 $mm.s^{-1}$ at 330 K to 0.14 $mm.s^{-1}$ at 633 K. Table 4.3 shows a summary of the fitting model applied in the data analysis.

Table 4.3: Summary of the fitting model.

Component	Model	δ(mm.s^{-1})	ΔE_Q (mm.s^{-1})	$\sigma(\delta)$(mm.s^{-1})	Γ(mm.s^{-1})
Fe_S	Voigt	SOD	-	0.13 - 0.23	Set to 0.34 (detector model) Global
Fe_N	Voigt	SOD	Follows $T^{3/2}$	0.08	
Fe_D	ISODam	Free	Free	$\sigma_L \neq \sigma_R$	
$^*Fe_I$	Voigt	SOD	-	0.08	

* present only at 77 K

The isomer shift values of all components followed the second-order Doppler (SOD) shift except for the damage site at high temperatures (T > 400 K). The calculated isomer shift values for the damage site are significantly higher than the experimental values and this is reflected in Figure 4.2. The quadrupole splitting of the damage site deviates from the $T^{3/2}$ variation above 426 K. Figure 4.3 shows the temperature dependence of the quadrupole splittings for Fe_D and Fe_N.

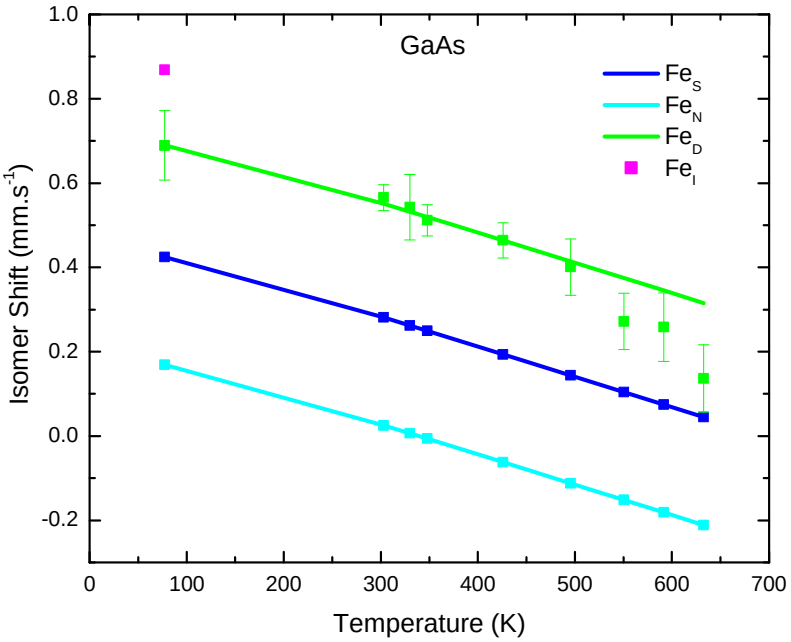


Figure 4.2: **Temperature dependence of isomer shifts observed in Mössbauer spectra for GaAs after ^{57}Mn* implantation, where the solid lines represent the calculated values and symbols represent the results extracted from the fits to the spectra.**

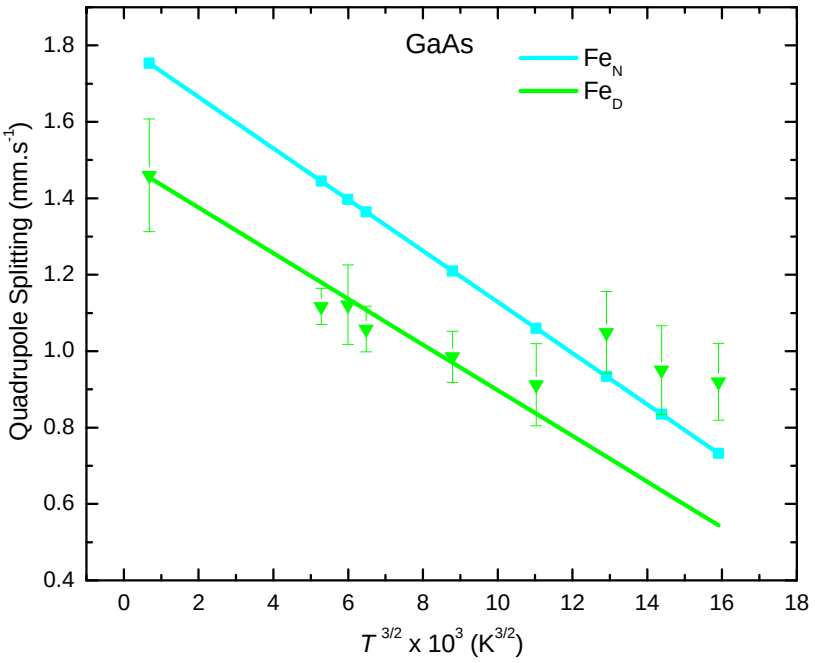


Figure 4.3: **Temperature dependence of the quadrupole splitting observed in the Mössbauer spectra for GaAs after ^{57}Mn* implantation, where the solid lines represent the calculated values and symbols represent the results extracted from the fits to the spectra.**

The changes in the isomer shift and quadrupole splitting values with respect to the expected values at high temperatures are attributed to the change in environment in the neighborhood of the impurity atoms.

4.1.3 Annealing Behavior

Figure 4.4 shows the variation in area fractions of different components with change in temperature.

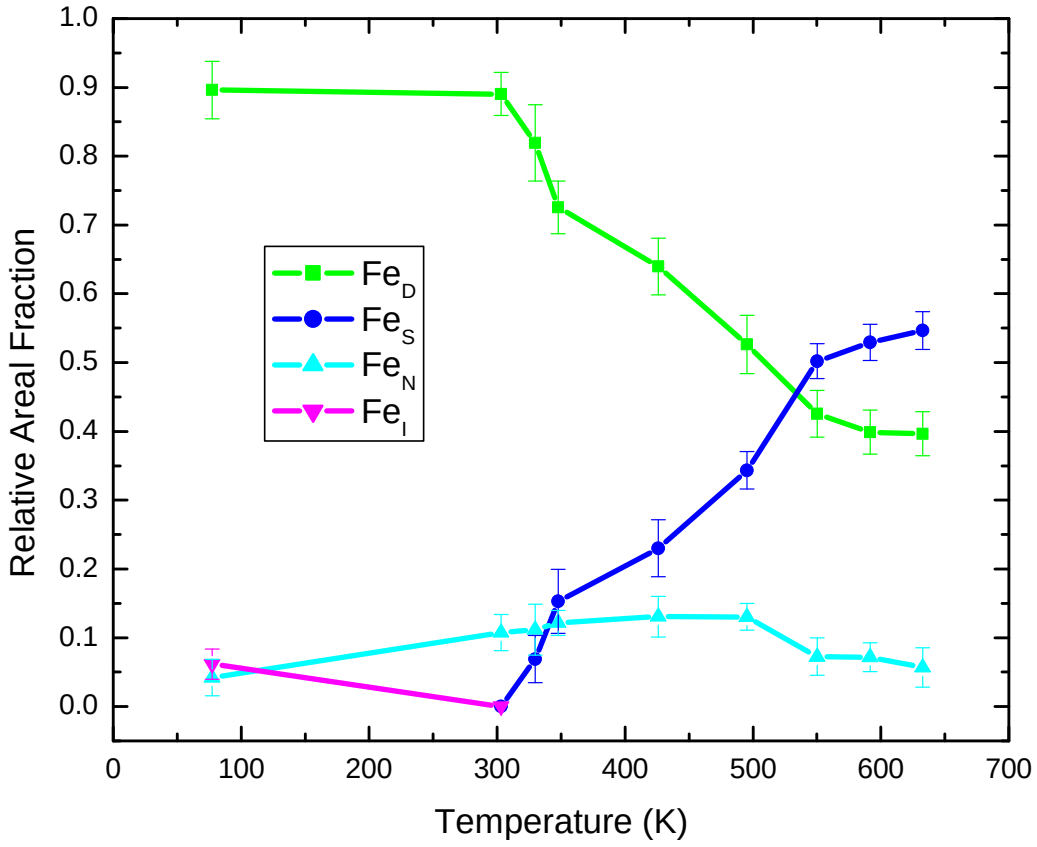


Figure 4.4: Areal fractions of components as a function of temperature, observed in the Mössbauer spectra for GaAs after ^{57}Mn* implantation.

In the temperature range 300 – 350 K, the areal fraction of the damage site decreased from approximately 90% to 73% with a corresponding increase in the substitutional Fe fraction from zero to approximately 15% around 350 K. An approximately 2% increase in the areal fraction of the Fe_N component is also observed in the same temperature range. Prominent annealing of the damaged sites is evident in the temperature range 350 – 550 K. The areal fraction of the

damaged sites decreased from 73% at 350 K to approximately 43% at 550 K. In this temperature range, the areal fraction of Fe_S increased by approximately 35% while Fe_N increased from 12% at 350 K to 13% at 495 K and then decreases to a constant value of approximately 7% at 550 K. The decrease in the areal fraction of Fe_N may be attributed to the breakdown of the impurity-vacancy complexes. The increase in Fe_S site population is attributed to the annealing of the damage sites with increasing temperature. Above 550 K, there is an increase in the areal fraction of Fe_S and a corresponding decrease of approximately 3% in the areal fraction of Fe_D, while the areal fraction of Fe_N remains constant above 550 K. The induced damage does not anneal completely at the highest measured temperature of approximately 633 K.

4.1.4 Summary of results for GaAs

Mössbauer measurements were performed after ^{57}Mn* implantation and annealing in GaAs held at temperatures between 77 and 633 K. The spectra were analyzed using four components;

1. A single line component which dominates the spectra at the high temperatures (> 550 K) is assigned to Fe atoms on Ga substitutional sites.

2. An asymmetric doublet due to radiation damage has a Debye temperature ($\boldsymbol{\theta}_D$ = 302 K) similar to the substitutional component ($\boldsymbol{\theta}_D$ = 275 K) and is assigned to Fe on near substitutional sites in non-cubic environments.

3. A low intense symmetric doublet (Fe_N) is assigned to near substitutional impurity-vacancy complex because of its similar Debye temperature ($\boldsymbol{\theta}_D$ = 268 K) as compared to the purely substitutional Fe atoms on Ga sites.

4. A single line with very low intensity only present at 77 K and a high isomer shift value (δ = 0.87 mm.s^{-1}) is assigned to Fe on interstitial sites. The Debye temperature of this component could not be calculated since there is only one data point in the measured temperature range.

A dominant annealing stage of the lattice damage is observed in the temperature range 350 K – 550 K, resulting in an appreciable increase in the substitutional fraction which is attributed to the annealing of the damage when some interstitials and/or Ga vacancies become mobile. The variation in the isomer shift and the quadrupole splitting values at high temperatures (T > 400 K) for the damage site can be attributed to the changes in bonding mechanism and environment in the neighborhood of the Mössbauer atom.

4.2 Data analysis and interpretation of Fe in GaP

The experimental data for GaP were fitted with four spectral components using the same model as GaAs for consistency and comparison purposes. Figure 4.5 shows ^{57}Fe Mössbauer spectra collected after ^{57}Mn* implantation into GaP single crystal held at temperatures between 77-700 K. The lattice site assignments used in the data analysis for GaP are the same as applied for GaAs. The spectra for GaP were fitted with an asymmetrically broadened doublet assigned to Fe atoms in the damaged sites (Fe_D) due to radiation induced damage. This component dominates the spectra in the measured temperature range 77 – 694 K. Three additional components: a single line assigned to substitutional component (Fe_S), a symmetric doublet assigned to near substitutional impurity-vacancy complexes (Fe_N), and a single line with low intensity is present at 77 K, but disappears below 320 K is assigned to Fe on interstitials sites (Fe_I). Table 4.4 shows the extracted hyperfine parameters obtained for GaP at room temperature and the Debye temperatures for the different lattice sites. The results obtained for GaP compare well with GaAs (see Tables 4.4 and 4.1, respectively). A detailed discussion of the similarities and differences in these materials is discussed later in this chapter.

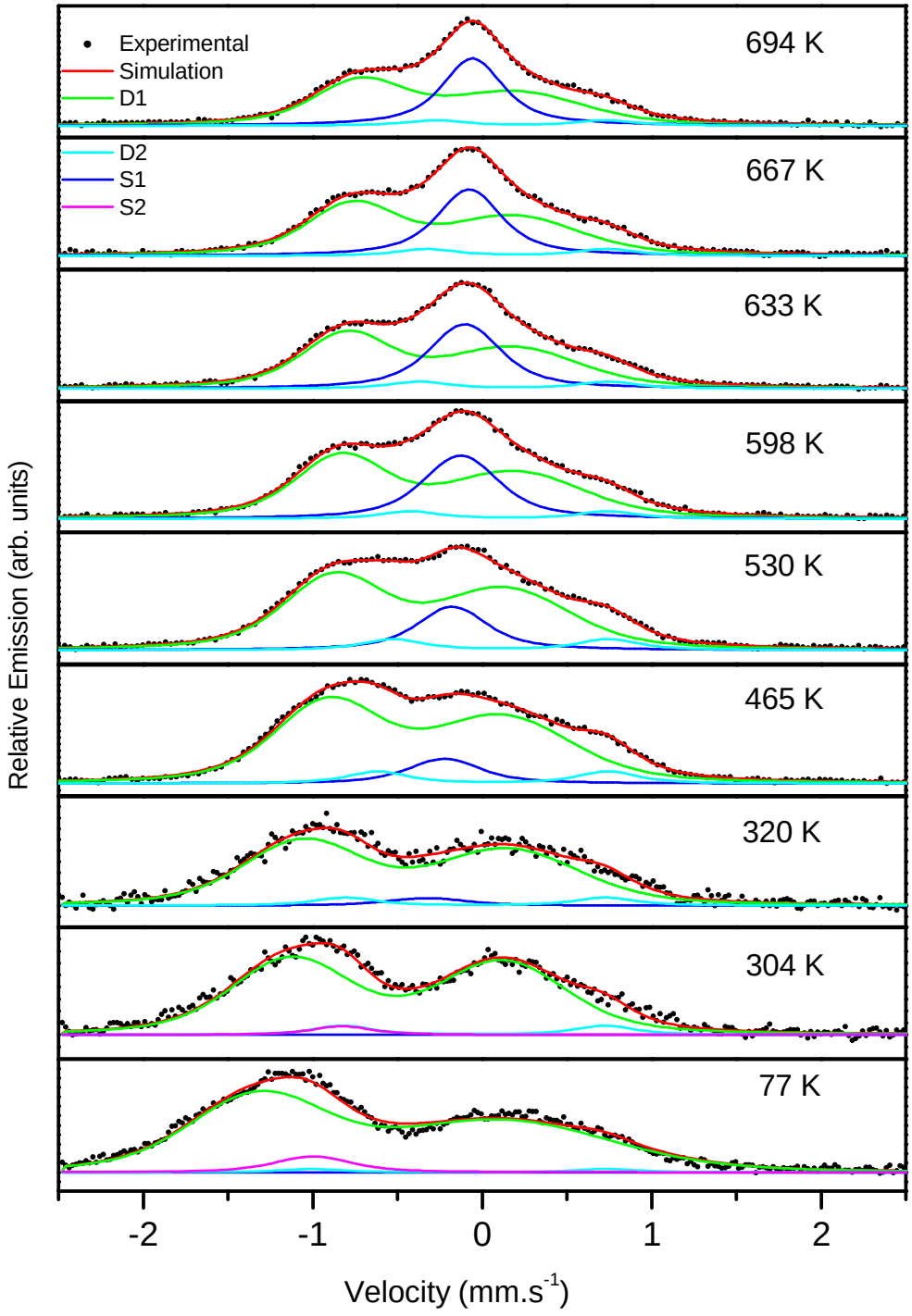


Figure 4.5: **^{57}Fe Mössbauer spectra obtained after ^{57}Mn* implantation into GaP held at the temperatures indicated.**

Table 4.4: Hyperfine parameters obtained at room temperature for GaP.

	δ (mm.s^{-1})	ΔE_Q (mm.s^{-1})	σ_R (δ) (mm.s^{-1})	σ_L(δ) (mm.s^{-1})	σ_R(δ) (mm.s^{-1})	θ_D (K)
Fe_D	0.50(3)	1.25(4)	-	0.29(4)	0.35(6)	304(40)
Fe_N	0.05(4)	1.55(1)	0.08	-	-	317(13)
Fe_S	0.34(2)	-	0.08-0.15	-	-	318(16)
Fe_I	0.83(5)	-	0.08			157(13)

Γ = 0.34 mm.s^{-1}

4.2.1 Discussion of hyperfine parameters

To obtain reasonable fits without increasing the number of components, Fe_S is represented as a single line whose broadening decreased from 0.15 mm.s^{-1} at 320 K to 0.08 mm.s^{-1} at 694 K.

The isomer shift values of all components followed the second-order Doppler shift except for the Fe atoms in small amorphous pockets at temperatures above 400 K. The calculated isomer shift values for the damaged sites are lower than the experimental values and this is reflected in Figure 4.6. The variation in the isomer shift values of the Fe_D component in GaP behaves differently in GaAs where the calculated values are higher than the experimental values. This could be attributed to the different bonding mechanism of Fe atoms in the damage sites in these materials at high temperatures.

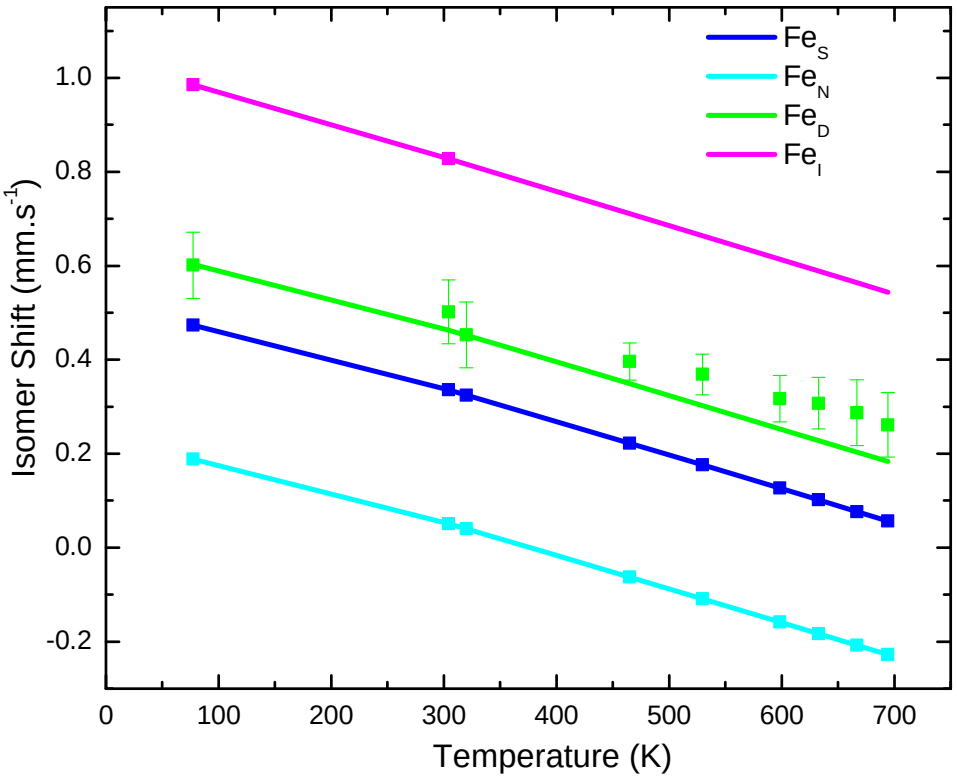


Figure 4.6: **Temperature dependence of isomer shifts observed in Mössbauer spectra for GaP after ^{57}Mn* implantation, where the solid lines represent the calculated values and symbols represent the results extracted from the fits to the spectra.**

The quadrupole splitting of the damage site deviates from the $T^{3/2}$ variation above 600 K where the calculated values are higher than the experimental values. This similar behavior is evident in GaAs above 500 K. The variations in the quadrupole splitting values at high temperatures for the damage site can be attributed to the change in environment in the neighborhood of the Mössbauer atom. This is illustrated in Figure 4.7.

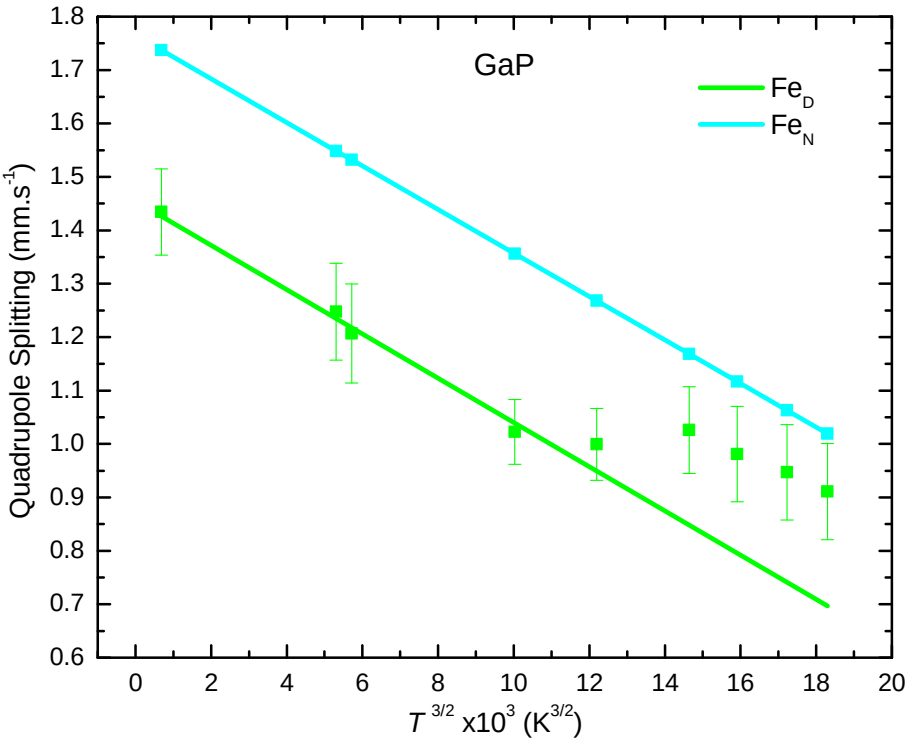


Figure 4.7: **Temperature dependence of the quadrupole splitting observed in the Mössbauer spectra for GaP after ^{57}Mn* implantation, where the solid lines represent the calculated values and symbols represent the results extracted from the fits to the spectra.**

4.2.2 Debye Temperatures of the lattice sites in GaP

The identical Debye temperatures of 318(16) K and 317(13) K for the Fe_S and Fe_N components, respectively, does not allow for a clear distinction between the two lattice sites. However, the presence of a large quadrupole splitting, (ΔE_Q = 1.55 mm.s^{-1}) implies that the nature of Fe_N component can be explained by near substitutional impurity atoms in association with adjacent vacancies. The higher isomer shift (δ = 0.83 mm.s^{-1}) and lower Debye temperature of 157(13) K for the Fe_I component compared to the Fe_S component confirms that some Fe impurity atoms are located in interstitial positions. The Fe_D components in GaP and GaAs have very similar isomer shift, quadrupole splitting and Debye temperature values at room temperature. This component may be attributed to Fe atoms in distorted environment because of the large quadrupole splitting and

possible association with some vacancies in impurity-vacancy complexes with different electronic and geometric structure compared to Fe_N is envisaged.

4.2.3 Annealing Behavior in GaP

The main annealing stage is evident in the temperature range 465 – 600 K resulting in the areal fraction of the damage site (Fe_D) decreasing by approximately 17%, with a corresponding increase of approximately 20% in the site population of Fe on substitutional Ga locations. In the same temperature range, the interstitial component disappears completely while the areal fraction of the Fe_N component decreases by 3%. The resulting decrease in the Fe_N areal fraction is attributed to the breakdown of the impurity-vacancy complexes. Above 600 K, the areal fraction of Fe_S increases by approximately 5% resulting from minor contributions of the decrease of the areal fractions in both the damaged sites and the impurity-vacancy complexes. Figure 4.8 show the annealing behavior in GaP.

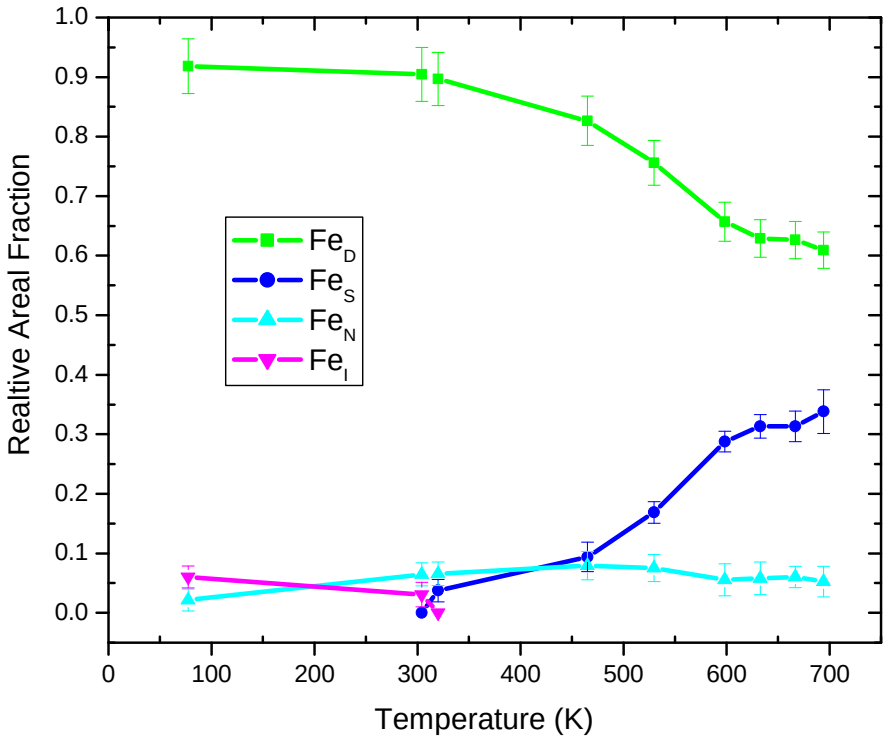


Figure 4.8: Areal fractions of components as a function of temperature, observed in the Mössbauer spectra for GaP after ^{57}Mn* implantation.

4.2.4 Summary of results for GaP

Mössbauer measurements were performed after ^{57}Mn* implantation and annealing in GaP held at temperatures between 77 and 694 K. The spectra were analyzed using four components:

a) A single line component which shows an appreciable increase of approximately 34% in site population after annealing at the highest temperature. This line is assigned to Fe atoms on Ga substitutional sites in cubic environment.

b) A low intense symmetric doublet Fe_N is assigned to near Fe substitutional impurity - vacancy complex because of its very similar Debye temperature value as compared to the purely substitutional Fe atoms on Ga sites.

c) An asymmetric doublet due to radiation damage which dominates over the whole temperature range is assigned to Fe in non-cubic environments because of the large quadrupole splitting value. The Debye temperature of 304(40) K for the Fe_D component is close to 318(16) K for the Fe_S component, which shows a possible similar coordination with the nearest neighbours as compared to the Fe_S component.

d) A single line with low intensity present below 320 K and a lower Debye temperature of 157(13) K compared to the Fe_S component is assigned to Fe on interstitial sites.

A dominant annealing stage of the lattice damage is evident in the temperature range 320 K – 633 K, resulting in an appreciable increase in the Fe_S component which is attributed to the annealing of the damage when some interstitials and/or Ga vacancies become mobile.

The variation in the isomer shift and the quadrupole splitting values at high temperatures for the damage site can be attributed to the changes in Fe-defect bonding mechanism and environment in the neighborhood of the Mössbauer atom. However, the isomer shift variation in GaP shows a different behavior as

compared to GaAs and this could be attributed to a different bonding mechanism of Fe atoms with its nearest neighbours in the damage sites in these materials at high temperatures.

4.3 Comparison of results obtained for GaAs and GaP

There are variations in the isomer shift and the quadrupole splitting values at high temperatures for the damage site in GaAs and GaP which can be attributed to the change in environment in the neighborhood of the Mössbauer atom. However, the isomer shift variation in GaP shows a different behavior as compared to GaAs. The isomer shift values obtained for GaP compare well with the calculated values showing slightly higher values; while in GaAs the determined isomer shift values are lower relative to the second order Doppler shift behavior. This could be attributed to different coordination of Fe atoms with its nearest neighbors in the damage sites at high temperatures in these materials. However, at low temperatures the hyperfine parameters show good correspondence with the second order Doppler shift variation.

In GaAs and GaP, the quadrupole splitting values of the damage site are higher than the $T^{3/2}$ dependence obtained at high temperatures. Figures 4.9 and 4.10 illustrate the low and high temperature variations of the quadrupole splitting values in these materials. Table 4.5 lists the corresponding T_k and $\Delta E_{Q,0}$ values at low and high temperatures in these materials.

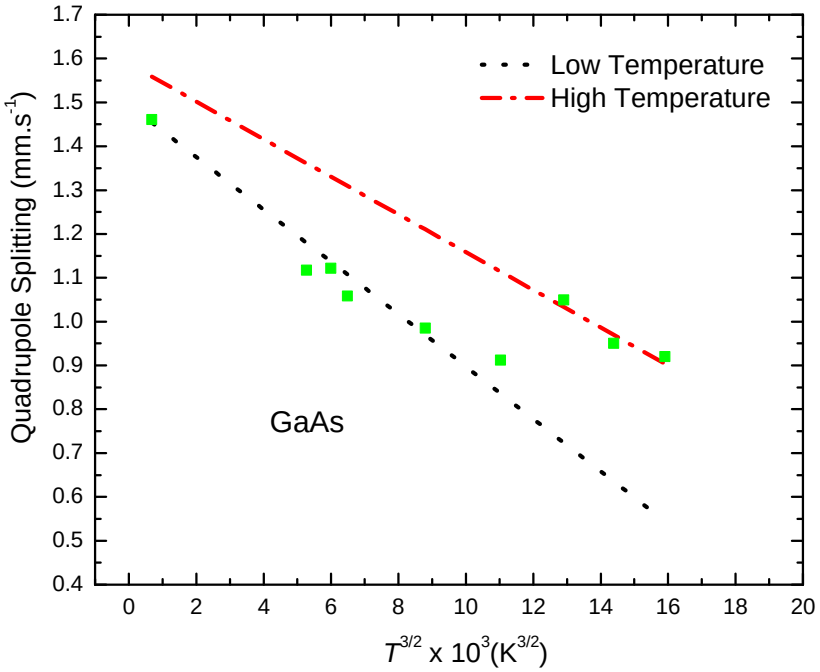


Figure 4.9: **Low and high temperature behavior of the quadrupole splitting for Fe_D in GaAs, where symbols represent the fitted data.**

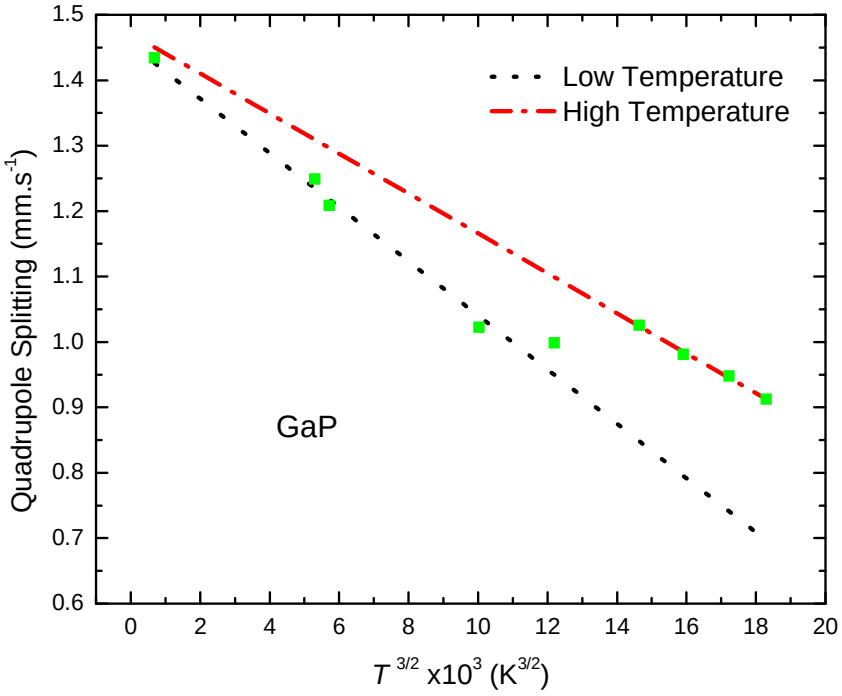


Figure 4.10: **Low and high temperature behavior of the quadrupole splitting for Fe_D in GaP, where symbols represent the fitted data.**

Table 4.5: Fitting parameters for low and high temperature quadrupole splitting behavior in GaAs and GaP.

	Low Temperature		High Temperature	
Fe_D	$\Delta E_{Q,0}$ (mm.s^{-1})	T_k (K)	$\Delta E_{Q,0}$ (mm.s^{-1})	T_k (K)
GaAs	1.49(2)	855(17)	1.58(3)	1109(20)
GaP	1.45(4)	1072(25)	1.47(4)	1323(27)

4.3.1 Comparison of annealing behavior in GaAs and GaP

A comparison of the annealing behavior in GaP and GaAs is shown in Figure 4.11.

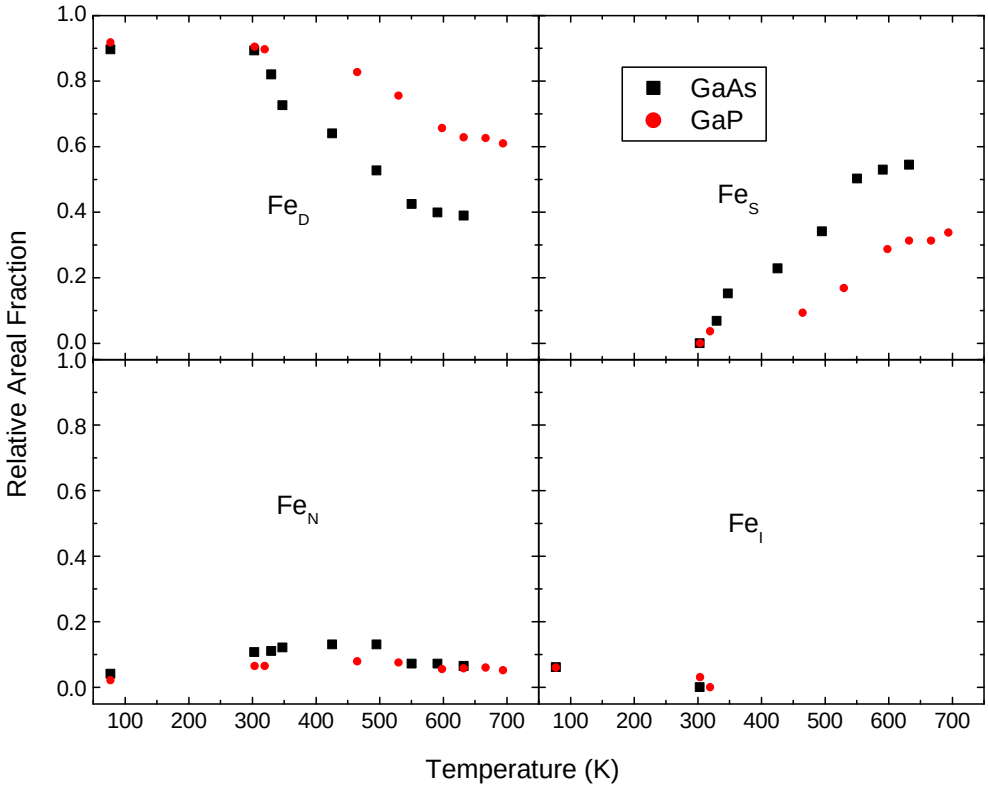


Figure 4.11: Comparison of areal fractions of the various components as a function of temperature between GaP and GaAs.

Prominent recovery of the damage site is more evident in GaAs (350 – 550 K) than in GaP (456 – 600 K) in the temperature range under study. The difference in the prominent annealing temperature ranges in GaAs as compared to GaP implies

the 'healing' of damaged bonds in GaP occur at a slower rate. This annealing behavior is attributed to the stronger Fe-P bonds in GaP (melting point ~ 1730 K) than Fe-As bonds in GaAs (melting point ~ 1335 K). This is further supported by the higher Debye temperature in GaP compared to GaAs for the Fe_S and Fe_N components. Furthermore, the purely interstitial component Fe_I which is present both in GaAs and GaP at 77 K, disappeared below 300 K in GaAs, but is present in GaP at 300 K and disappeared below 320 K.

4.3.2 Isomer shift variation of Fe_D and Fe_S with bond length in GaAs and GaP

A comparison of isomer shifts for GaP and GaAs with Si, Ge, SiGe and diamond is shown in Figure 4.12. For Si, Ge, SiGe and diamond, the graph shows a linear dependence between their bond lengths and the isomer shift values which implies they have very similar local structures.

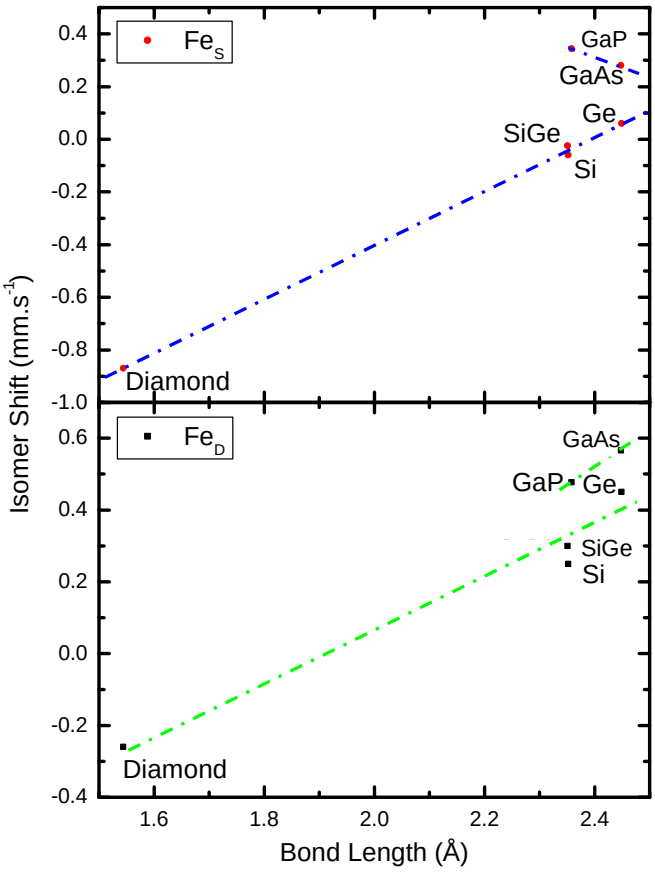


Figure 4.12: Isomer shifts of Fe_S and Fe_D in GaP and GaAs as a function of bond length. A comparison is made with other semiconductors.

The isomer shift values of Fe_S and Fe_D for Si, Ge, SiGe and diamond show a similar increase i.e. increasing *s*-electron density with increasing nearest neighbor distance. In GaP and GaAs, the isomer shift values of the Fe_D component increases with increasing bond length. This behavior was also evident for Si, Ge, SiGe, and diamond whereas the opposite behavior was observed for the Fe_S component. The *s*-electron density at the substitutional site in GaAs is larger than in GaP which can be explained by the compression of the electron shell volume of the Fe atoms in these materials. The trends of isomer shift variations of the Fe_S and Fe_D components with the bond length of the host materials were determined; however the results are inconclusive due to a limited number of cubic III-V semiconductors investigated in this project.

4.4 Discussion on 'charge states'

The extracted isomer shift and quadrupole splitting values at room temperature for both GaAs and GaP are presented in Table 4.6.

Table 4.6: Hyperfine parameters for GaAs and GaP at room temperature.

	Fe_D		Fe_N		Fe_S	Fe_I
	δ (mm.s^{-1})	ΔE_Q (mm.s^{-1})	δ (mm.s^{-1})	ΔE_Q (mm.s^{-1})	δ (mm.s^{-1})	δ (mm.s^{-1})
GaAs	0.57(5)	1.12(1)	0.02(2)	1.44(3)	0.28(4)	0.87(2)$^{+}$
GaP	0.50(3)	1.25(4)	0.05(5)	1.55(1)	0.34(2)	0.99(3)$^{+}$

Γ = 0. 34 mm.s^{-1}, $^{+}$ Isomer shift at 77 K

Figure 4.13 shows the extracted hyperfine parameters for GaAs and GaP plotted on an isomer shift versus quadrupole splitting graph obtained from the Mössbauer Effect Data Center (MEDC)[67].

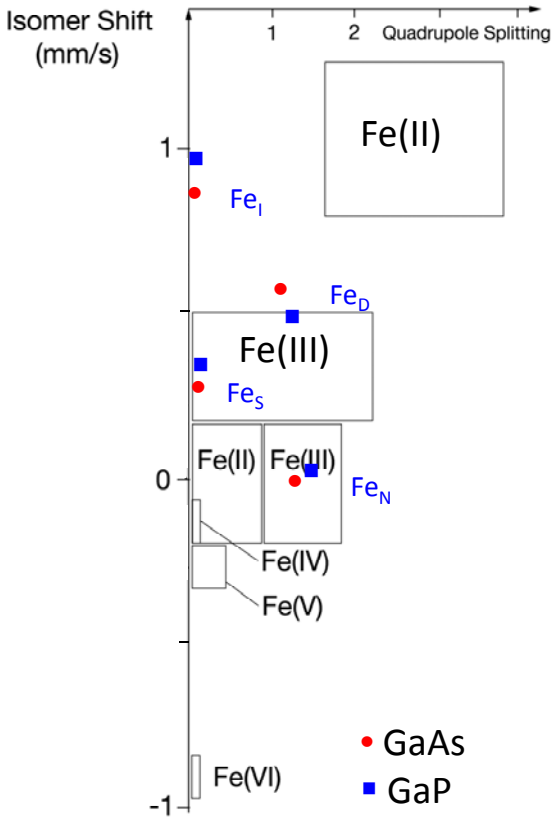


Figure 4.13: Comparison between the extracted hyperfine parameters for Fe in GaAs and GaP with values from the Mössbauer Effect Data Center.

The isomer shift and quadrupole splitting values of the Fe_S component in GaAs and GaP obtained after implantation of ^{57}Mn* correspond to the trivalent state of iron $^{57}Fe^{3+}$ with a $3d^5$ electronic configuration in cubic environments and this assignment supports the predicted substitutional Ga site location[20-23] in other studies. Thus the occupation of substitutional sites is governed by chemical effects rather than kinetic displacement mechanisms. The impurity atoms tend to form tetrahedrally coordinated sp^3 orbital with their valence electrons and this governs the selection of lattice sites. The isomer shift and quadrupole splitting values of Fe in the damage site (Fe_D) show ions associated with a near $3d^5$ configuration in distorted environments[22]. The isomer shift of the purely interstitial component present at low temperatures shows Fe with near electronic configuration of $3d^6$. Lastly, the Fe_N component which is tentatively assigned to Fe with a $3d^5$ electronic configuration due to its complex nature.

4.5 Comparison of ^{57}Mn* and ^{119m}Sn, $^{119}In^{+}$and $^{119}Sb^{+}$ implantations in GaP and GaAs

Mössbauer studies of Sn in GaP, have identified three components, (i) Sn in Ga substitutional sites using ^{119m}Sn and $^{119}In^{+}$ implantations, (ii) while with $^{119}Sb^{+}$ implantations Sn is incorporated on the P site, a low intense impurity-vacancy (I–V) complex associated with divacancies, and (iii) a third component ascribed to vacancies – with associated substitutional Sn atoms. Tables 4.7 and 4.8 shows the comparison between isomer shift values for the different components using different precursor isotopes for Sn and Fe implanted in GaP and GaAs.

Table 4.7: Isomer shift values of different components for various Mössbauer probes in GaP[9,10].

Probe/Site	I - V_1	Substitutional	I - V_2	Interstitial	Damage site
^{119m}Sn	-	1.65(3)	2.82(5)		-
$^{119}In^{+}$	1.25(10)	1.59(3)	2.81(6)	-	-
$^{119}Sb^{+}$	1.2(1)	1.82(3)*	2.64(4)		
^{57}Mn*	0.05(5)	0.34(2)	-	0.83(5)	0.50(3)

* on P site, Isomer shifts in $mm.s^{-1}$

Table 4.8: Isomer shift values of different components for various Mössbauer probes in GaAs[8,11,12].

Probe/Site	I - V_1	Substitutional	I - V_2	Interstitial	Damage site
^{119m}Sn	1.26(15)	1.76(6)	2.86(15)	3.50(30)	-
$^{119}In^{+}$	-	1.72(2)	2.76(4)	-	-
^{57}Mn*	0.02(2)	0.28(4)	-	0.87(2)	0.57(5)

Isomer shifts in $mm.s^{-1}$

In GaAs, Mössbauer studies have identified four components in the spectra assigned to; (i) Sn in substitutional Ga sites, (ii) two impurity-vacancy complexes (I-V_1 and I-V_2) of different electronic and geometric structure, and (iii) a small fraction to interstitial impurity atoms[8-10].

The isomer shift values of ^{57}Mn* implantations are very small compared to ^{119m}Sn, $^{119}Sb^{+}$ and $^{119}In^{+}$ implantations in GaAs and GaP. This significant difference in the isomer shift values may be explained in terms of the relaxation in the bonds formed between Sn and the lattice atoms in these materials as compared to Fe. The weaker bonds in Sn may be interpreted by the greater shielding of outer electrons from the nucleus by inner atomic shells and a larger atomic radius of Sn compared to Fe.

Chapter 5

Conclusions and Recommendations

Mössbauer studies were conducted to investigate the site location and nature of Fe impurities in GaAs and GaP single crystals following $^{57}Mn^{*}$ implantation and annealing at temperatures between 77 – 700 K. The spectra was analyzed using four components, an asymmetric doublet due to radiation damage (Fe_D) assigned to Fe atoms in small amorphous pockets, two single lines, one attributed to Fe at substitutional Ga sites (Fe_S) and the other to a purely Fe interstitial site (Fe_I) only present below 320 K, and a low intense symmetric doublet (Fe_N) attributed to substitutional Fe-vacancy complex which results in the formation of a dangling bond as illustrated in Figure 5.1.

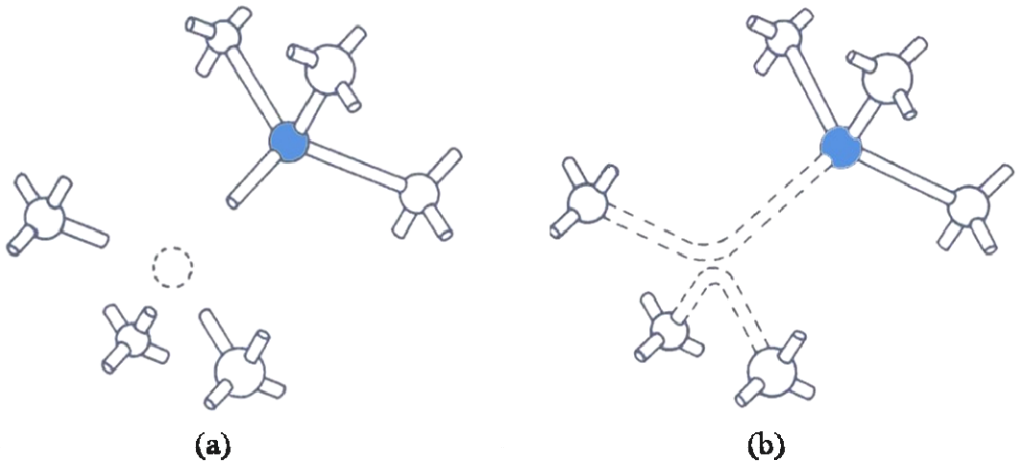


Figure 5.1: Vacancy in zinc-blende lattice. (a) Four bonds are broken in order to form a vacancy. (b) resulting dangling bond[68].

The calculated Debye temperatures for the different lattice sites and hyperfine parameters reflect Fe atoms on substitutional Ga sites in cubic environments with a possible near $3d^5$ electronic configuration. Near $3d^5$ and $3d^6$ electronic configurations are envisaged from hyperfine parameters and Debye temperatures for Fe atoms in distorted environments and interstitial sites, respectively.

Moreover, Fe atoms in small amorphous pockets may be explained in terms of their association with impurity-vacancy complexes with different geometric and electronic configuration to the Fe_N component. Lastly, a $3d^5$ electronic configuration is tentatively assigned for the Fe_N component because of its complex nature.

The variation in the hyperfine parameters in GaAs and GaP at high temperatures for the damage site can be attributed to the changes in the impurity-defect bonding mechanism and environment in the surroundings of the Mössbauer atom. However, a different coordination to the nearest neighbors in GaAs and GaP is predicted due to the different isomer shift variations with respect to the second-order Doppler shift behavior.

Different annealing stages of the induced damage are evident in GaAs and GaP, resulting in a significant increase in the Fe_S site population which is due to mobile Ga vacancies and/or interstitials. However, prominent recovery of the damage is more evident in GaAs than in GaP which is attributed to Fe forming stronger bonds with P than As. Moreover, the slow recovery of the radiation damage in GaP with increasing annealing temperature compared with GaAs confirms stronger Fe-P bonds in GaP relative to Fe-As bonds in GaAs. This is further supported by the higher Debye temperature values extracted for the different lattice sites in GaP as compared to GaAs. In addition, minor variations in the areal fraction of the Fe_N component relative to other components show the stability of Fe atoms in the impurity-vacancy complexes. However, the Fe_N component is more stable in GaP compared to GaAs at temperatures > 300 K as reflected by an approximately constant areal fraction with increasing temperature.

Isomer shift variations with bond length for Fe atoms in the damage sites shows similar trends with diamond, Ge, Si and SiGe which show an increase with increasing bond length. However, there exists inconsistent behavior in the variations of isomer shift values with bond length for Fe atoms in substitutional sites compared with the semiconductors listed above. Thus, well-defined trends of the isomer shift variations with the bond length could not be fully established for the Fe_s component. However, a complete picture of the behavior will materialize

once results of InP and InAs are published by W.B. Dlamini (University of KwaZulu-Natal) dissertation unpublished.

It is well known that Fe atoms located on substitutional III sites in cubic III-V compound semiconductors act as deep centers[69,70] either as neutral Fe^{3+} or singly[71] charged Fe^{2+}. Deep centers, located in the middle of the energy gap commonly affect the optical properties of semiconductors and further studies to investigate this resulting effect will be discussed in the next section.

5.1 Recommendations

The electronic properties of a semiconductor are determined by the presence of impurity atoms and lattice distortions which dictate the feasibility and functionality of a device. Semiconductors have a wide range of applications such as photorefractive sensor devices, radiation and particle detectors, and substrates for high speed electronic and optoelectronic integrated circuits[72]. The usefulness of a semiconductor in one field or the other is strongly affected by the energy levels associated with the dopants or related defects. The associated defects are classified as shallow or deep defects, depending on the location of the introduced electronic states to the edge of valence band or conduction band within the band gap. Figure 5.2 shows the difference between the shallow and deep defects.

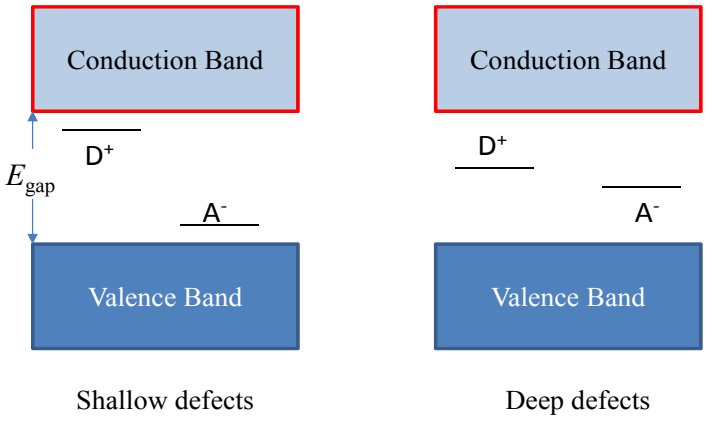


Figure 5.2: Difference between shallow and deep defects.

To determine the specific change in electrical and optical characteristics caused by the presence of these impurities, further studies are proposed. The most obvious

quantity characterizing a semiconductor is the electrical conductivity which is determined by the presence of majority charge carriers, their concentration, and mobility. This can be achieved by performing electrical transport (Hall Effect and conductivity) measurements as function of temperature[3,4,73]. Shallow states generate free charge carriers at ambient temperatures which directly control the conductivity of semiconductors. Deep electronic states however, act as recombination centers for free charge carriers and even in small concentrations, reduce their lifetime either in a beneficial way, as for fast-switching devices, or in a detrimental way, for example in solar cells and lasers diodes[74]. Thus, a particular defect is useful for a given application and may be 'harmful' for another application. Deep level transient spectroscopy (DLTS) can be used to characterize these deep defects i.e. to identify the deep level centers, measure the energy levels and correlate the charge carrier lifetimes. However, Photoluminescence spectroscopy (PL) is sensitive to both shallow and deep centers. In PL measurements, free electron and hole pairs are created if the energy of the incident photons is higher than the band gap of the semiconductor. The subsequently emitted PL light arises from the recombination of the electrons and holes via different channels, while the energy of emitted photons reflects the electronic states introduced by the different impurities or related defects[75]. In this way, information on the energy levels of the impurity centers is obtained. Further investigations on antisite and other related defects can be conducted.

Perturbed angular correlation (PAC) and emission channeling (EC) can be used to complement Mössbauer emission spectroscopy (MES) studies. PAC is well suited for investigations on the structural, dynamical and electronic properties of single impurities, inter-impurity and impurity-defect complexes on an atomic scale[73] through hyperfine interactions as in MES. However, as mentioned earlier, the isomer shift is only accessible to MES. EC can be used to locate the lattice site of probe atoms which utilizes the channeling or blocking effect of charge particles emitted from radioactive isotopes in a single crystal[73,76,77]. The α- and β-particles are detected in different directions with respect to the crystal lattice, the angular dependence of the count rate indicates whether the impurity atoms are situated on an interstitial or substitutional lattice site[73,77].

Appendix A: Summary of Fitting Models Applied

The following models were applied for data analysis using the code Vinda in order to give consistent fits.

Model 1. 4 Components: Asymmetric Doublet → Damage site using ISODamSS
Single line → Substitutional using Voigt with $\Delta E_Q = 0$
Symmetric doublet → impurity-vacancy complexes
Doublet → pure interstitial using Voigt with $\Delta E_Q \neq 0$

Model 2. 4 Components: Two asymmetric Doublets → Two damage sites using ISODamSS
Single line → substitutional using Voigt with $\Delta E_Q = 0$
Symmetric Doublet → impurity-vacancy complexes

Model 3. 3 Components: Asymmetric Doublet → Damage site using DISTQ
Single line → substitutional using Voigt with $\Delta E_Q = 0$
Symmetric Doublet → impurity-vacancy complexes

Model 4. 3 Components: Asymmetric Doublet → Damage site using DISTQ
Double line → substitutional using Voigt with $\Delta E_Q < 2.6$
Symmetric Doublet → impurity-vacancy complexes

Model 5. 4 Components: Asymmetric Doublet → Damage site using DISTQ
Double line → substitutional using Voigt with $\Delta E_Q < 2.5$
Two Doublets → impurity-vacancy complexes or an interstitial using Voigt with $\Delta E_Q < 2.5$

Model 6. 4 Components: Asymmetric Doublet → Damage sites using ISODamSS
Single line → substitutional using Voigt with $\Delta E_Q = 0$
Symmetric doublet → impurity-vacancy complexes
Single line → purely interstitials using Voigt with $\Delta E_Q = 0$

Models 1 – 5 did not give satisfactory fits for the temperature range under study however Model 6 gave reasonable fits and is reported in this document.

Appendix B: Fitting using Vinda

B.1 Single Spectrum Fitting

The fitting of the first spectrum is initially performed manually by varying the fitting parameters to obtain a desired fit from the different components selected. The components and corresponding models are chosen based on the expected lattice sites and defects for different impurity atoms. When a close approximation is obtained, the Solver tool in Microsoft Excel is applied to obtain a better approximation. The chi-square cell (always F30) is the target cell and all other cells with appropriate parameters are selected to be minimized. These include the background, hyperfine parameters, line-widths and areas. Figure B.1 show the dialog box for the solver parameters.

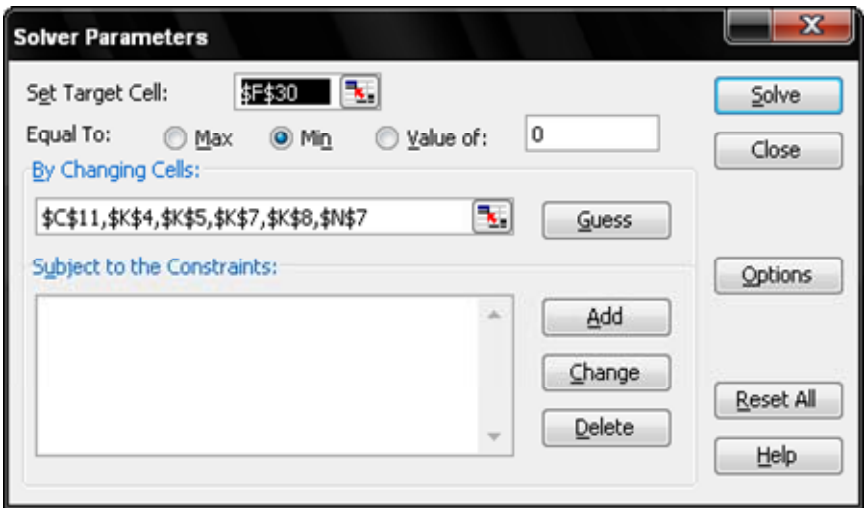


Figure B1: Dialog box for the solver parameters.

The next spectrum is then fitted using the fitting parameters of the previous spectrum as starting values. The preceding spectrum sheet is then copied and the new experimental data for the next corresponding temperature is read in after which the file name changes automatically. The Solver is then used to find a solution and after converging, a dialog box appears (see Figure B.2) requesting to keep the result or restore original values.

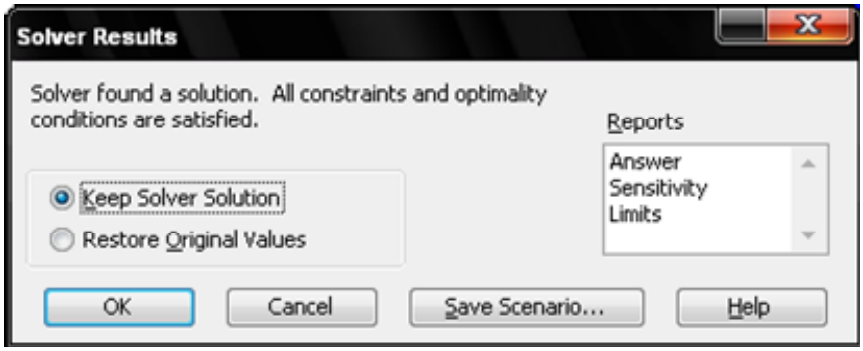


Figure B2: Dialog box for solver results.

The obtained solution after a fitting a single spectrum is illustrated in Figure B.3.

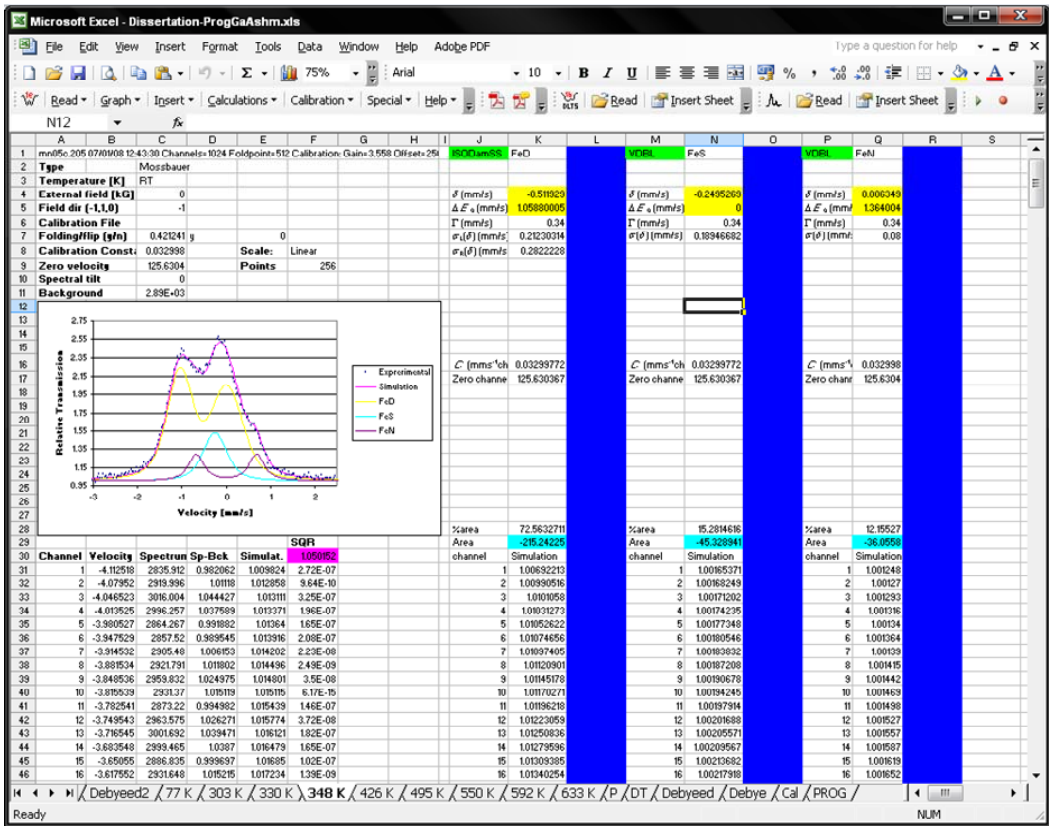


Figure B3: Spectrum sheet after fitting.

B.2 Simultaneous Fitting

Simultaneous analysis can be done in Vinda, where all model parameters for different spectrum sheets (signifying different temperature measurements) are linked to one main sheet known as the Prog sheet. The fitting is done on the Prog

sheet where a reference chi-square value for each Spectrum sheet has to be constructed. A typical Prog sheet is shown in Figure B4.

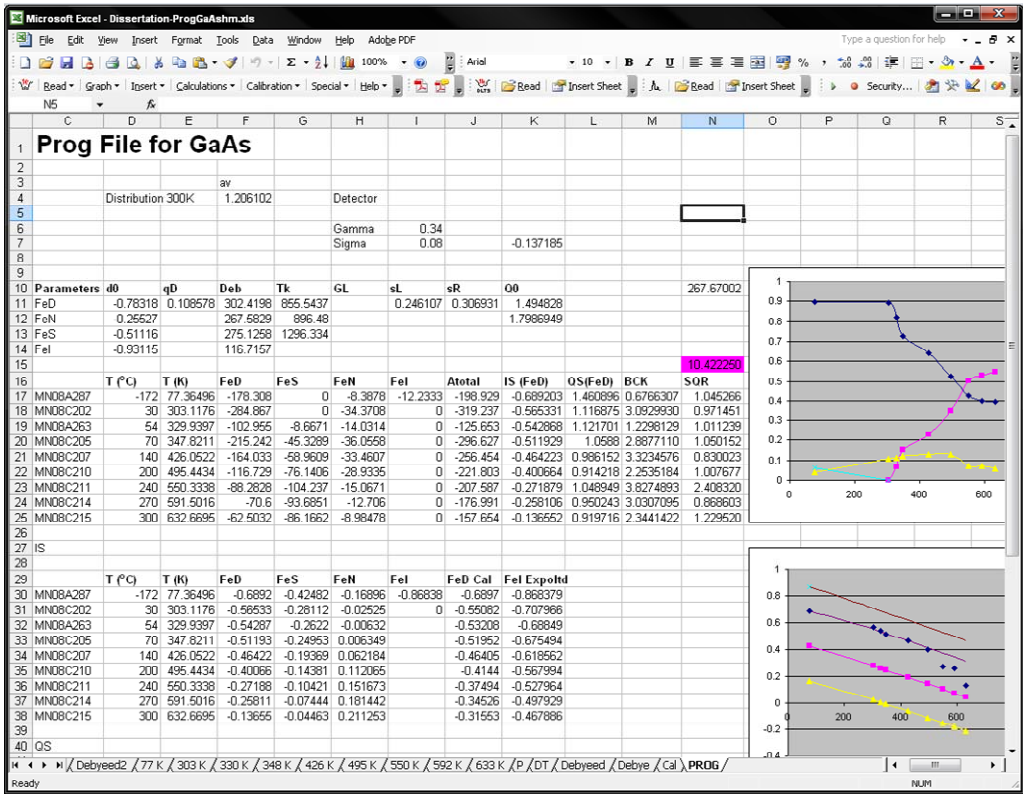


Figure B4: Typical Prog sheet for simultaneous fitting.

Simultaneous fitting allows temperature dependent parameters to be calculated and monitored using built-in functions for the second-order Doppler shift (δ_{SOD}) and the recoil-free fraction, f known as **ffac** and **sod**, respectively. These functions are based on equations (2.10) and (2.13), respectively. The calculation routine utilizes numerical integration, thus it is slow but very accurate over all practical temperatures. Figure B5 shows the **sod** function used to calculate the isomer shift of a component based on equation (2.20).

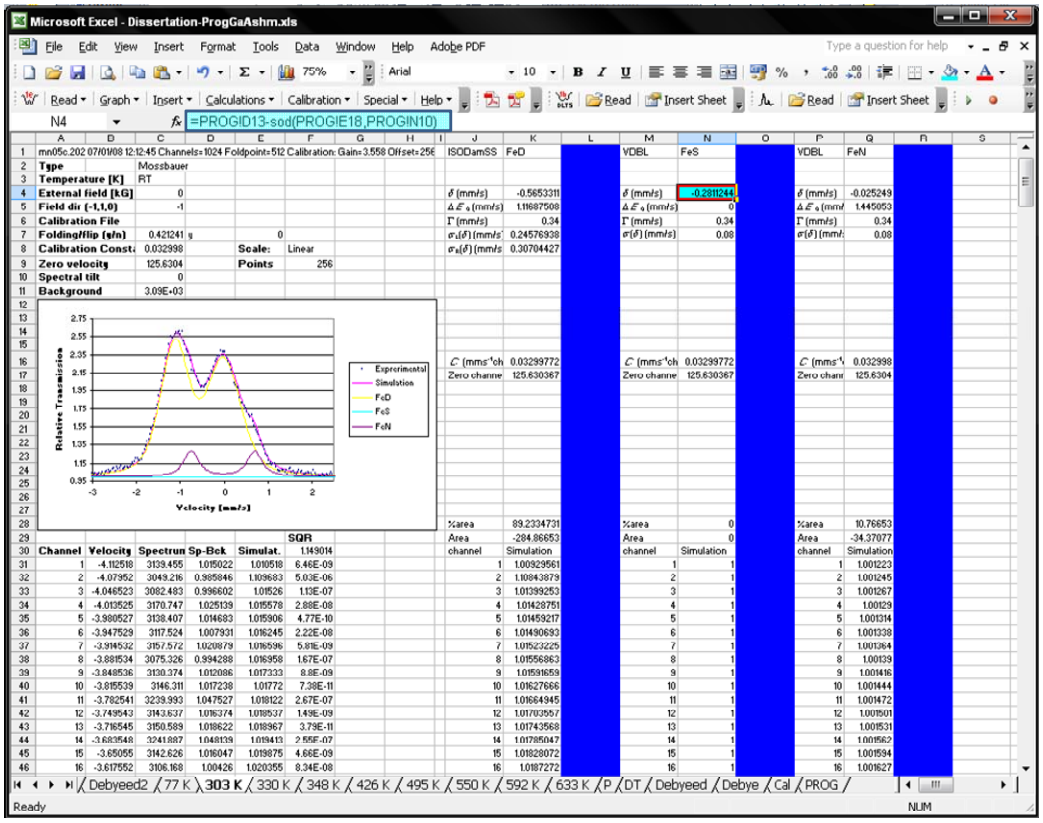


Figure B5: Built-in sod function used for calculating the isomer shift.

B.3 Error analysis

Errors in the calculated values are determined from the chi-squared value χ^2 which is defined by the equation

$$\chi^2 = \sum_{i=1}^{N} \frac{(Data_i - Simulation_i)^2}{Data_i}$$

The chi-squared value displayed in cell F30 in Figure B6 is normalized by the number of points. This is convenient as χ^2=1 signifies a perfect fit. Thus, the number of points should be supplied to the Error Analysis dialog box shown in Figure B6.

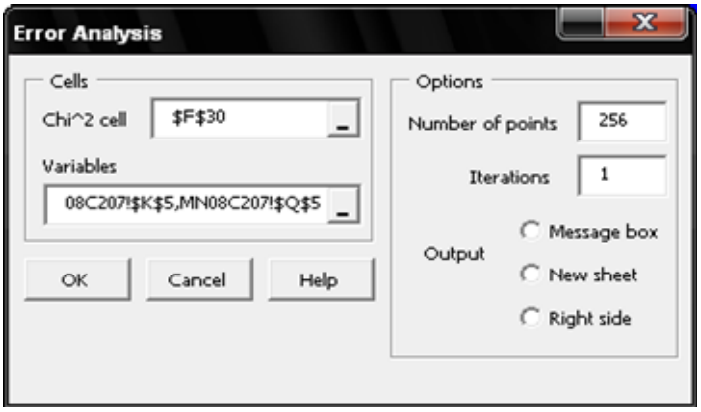
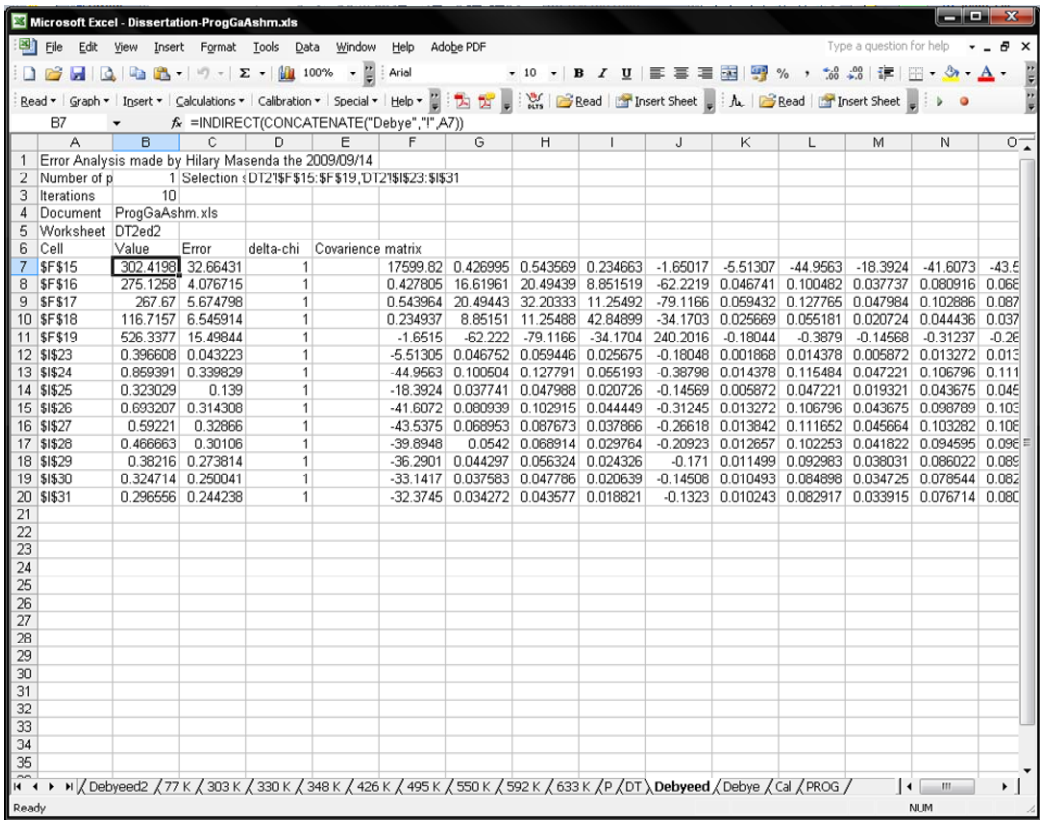


Figure B6: Error Analysis dialog box.

The number of iterations for a parameter in the dialog box shown above should be set higher than 1 so that a more accurate calculation can be carried out for the necessary change. Figure B7 shows a typical error analysis result obtain for Debye temperatures.



	A	B	C	D	E	F	G	H	I	J	K	L	M	N	O
1	Error Analysis made by Hilary Masenda the 2009/09/14														
2	Number of p	1	Selection	('DT2'!$F$15:$F$19,'DT2'!$I$23:$I$31											
3	Iterations	10													
4	Document	ProgGaAshm.xls													
5	Worksheet	DT2ed2													
6	Cell	Value	Error	delta-chi	Covarience matrix										
7	$F$15	302.4198	32.66431	1		17599.82	0.426995	0.543569	0.234663	-1.65017	-5.51307	-44.9563	-18.3924	-41.6073	-43.5
8	$F$16	275.1258	4.076715	1		0.427805	16.61961	20.49439	8.851519	-62.2219	0.046741	0.100482	0.037737	0.080916	0.068
9	$F$17	267.67	5.674798	1		0.543964	20.49443	32.20333	11.25492	-79.1166	0.059432	0.127765	0.047984	0.102886	0.087
10	$F$18	116.7157	6.545914	1		0.234937	8.85151	11.25488	42.84899	-34.1703	0.025669	0.055181	0.020724	0.044436	0.037
11	$F$19	526.3377	15.49844	1		-1.6515	-62.222	-79.1166	-34.1704	240.2016	-0.18044	-0.3879	-0.14568	-0.31237	-0.28
12	$I$23	0.396608	0.043223	1		-5.51305	0.046752	0.059446	0.025675	-0.18048	0.001868	0.014378	0.005872	0.013272	0.013
13	$I$24	0.859391	0.339829	1		-44.9563	0.100504	0.127791	0.055193	-0.38798	0.014378	0.115484	0.047221	0.106796	0.111
14	$I$25	0.323029	0.139	1		-18.3924	0.037741	0.047988	0.020726	-0.14569	0.005872	0.047221	0.019321	0.043675	0.045
15	$I$26	0.693207	0.314308	1		-41.6072	0.080939	0.102915	0.044449	-0.31245	0.013272	0.106796	0.043675	0.098789	0.103
16	$I$27	0.59221	0.32866	1		-43.5375	0.068953	0.087673	0.037866	-0.26618	0.013842	0.111652	0.045664	0.103282	0.108
17	$I$28	0.466663	0.30106	1		-39.8948	0.0542	0.068914	0.029764	-0.20923	0.012657	0.102253	0.041822	0.094595	0.098
18	$I$29	0.38216	0.273814	1		-36.2901	0.044297	0.056324	0.024326	-0.171	0.011499	0.092983	0.038031	0.086022	0.089
19	$I$30	0.324714	0.250041	1		-33.1417	0.037583	0.047786	0.020639	-0.14508	0.010493	0.084898	0.034725	0.078544	0.082
20	$I$31	0.296556	0.244238	1		-32.3745	0.034272	0.043577	0.018821	-0.1323	0.010243	0.082917	0.033915	0.076714	0.080

Figure B7: Typical Error Analysis worksheet.

REFERENCES

[1] Bardeen, J., *Nobel Lecture*, (1956) 318-341.

[2] Fischer-Cripps, A. C., *The Electronics Companion*, IOP Publishing, (2005).

[3] Deicher, M., and the ISOLDE collaboration, *Eur. Phys. J.* **A 15**, (2002) 275-280.

[4] Deicher, M., Weyer, G., Wichert, Th., and the ISOLDE collaboration, *Hyp. Int* **151/152**, (2003) 105-123.

[5] Bosi, M. and Pelosi, C., *Prog. Photovolt: Res. Appl.* **15**, (2007), 51-68.

[6] Held, G., *Introduction to Light Emitting Diode Technology and Applications*, CRC Press, (2008) pp.7.

[7] Sibilia, C., Benson. T. M., Marcinial, M., and Szoplik, T. (Eds), *Photonic Crystals: Physics and Technology*, Springer, (2008) pp 135.

[8] Holm, N.E., Nylandsted, A., Deutch, B.I., and Weyer, G., *Inst. Phys. Conf. Ser. No.* **46**, (1979) p 735.

[9] Weyer, G., Damgaard, S., Petersen, J.W., and Heinemeier, J.*, Phys. Stat. Sol. (B)* **98**, (1980) K147.

[10] Weyer, G., Petersen, J.W., and Damgaard, S., *Hyp. Int.* **15/16,** (1983) 495-498.

[11] Holm, N.E. and Weyer, G., *J. Phys. C: Solid St. Phys.,* **13,** (1980) 1109-20.

[12] Weyer, G., Damgaard, S., Petersen, J.W. and Heinemeier, J., *J. Phys. C: Solid St. Phys.,* **13** (1980) L181-3.

[13] Weyer, G., Petersen, J.W., Damgaard, S., Nielsen, H.L., and Heinemeier, J, *Phys. Rev. Lett.* **Vol 44, No 3**, (1980) 155-7.

[14] Weyer, G., Petersen, J.W. and Damgaard, S., *Physica* **116B**, (1983) 470-3.

[15] Nielsen, O.H., Larsen, F.K., Damgaard, S., Petersen, J.W. and Weyer, G., *Z. Phys.* **B 52**, (1983) 99-109.

[16] Weyer, G., Petersen, J.W. and Damgaard, S., *Physica* **117 B & 118 B**, (1983) 523-5.

[17] Weyer, G. and the ISOLDE Collaboration, *Hyp. Int.* **129**, (2000) 371-390.

[18] Lannoo, M., Svane, A., Overhof, H. and Katayama-Yoshida, H., *Theory* in *Hyperfine Interaction of Defects in Semiconductors,* ed. Langouche, G., Elsevier, (1992) 379.

[19] Seregin, P.P., Nasredinov, F.S., and Bakhtiyarov, A. Sh. *Phys. Stat. Sol*. (*b*) **91**, (1979) 35.

[20] Seregin, P.P., Stepanova, T.R, Kozhanova, Yu.V., and Volkov, V.P., *Semiconductors* **Vol. 37 No. 8**, (2003) 889-93.

[21] De Wit, M., and Estle, T.L., *Phys. Rev.*, **Vol 132. No. 1**, (1963) 195-201.

[22] Albanese, G., Fabri, G., Lamborizio, C., Musci, M., and Ortalli, I., *IL Nuove Cimento* **Vol L.B**, **N.1**, (1967).

[23] Demidov, E.S., Karzanov, V.V., Gromoglasova, A.B., and Morozkin, O.N., *Semiconductors* **Vol 33. No. 4**, (1999) 377-9.

[24] Mössbauer, R.L., *Nobel Lecture*, (1961) 584-601.

[25] Kolk, B., *S. Afr. J. Sci.*, **83**, (1987) 480-486.

[26] Williamson, D.L., Niesen, L., Weyer, G., Sielemann, R. and Langouche, G., *Mössbauer spectroscopy* in *Hyperfine Interaction of Defects in Semiconductors,* ed. Langouche, G., Elsevier, (1992) 1.

[27] Gutlich, P., Link, R. and Trautwein, A., *Mössbauer Spectroscopy and Transition Metal Chemistry,* Springer-Verlag, (1978) 4-12.

[28] Gunther K. W., *Mössbauer Effect: Principles and Applications,* Academic Press*,* (1964) 1-17.

[29] Chen, Y. and Yang, D., *Mössbauer Effect in Lattice Dynamics-Experimental Techniques and Applications*, Willey-VCH, (2007).

[30] Lin, C.M., and Lin, S.T., *J. Phys. Condens. Matter* **5**, (1993) L247-L250.

[31] Kuzmann, E., Nagy, S. and Vertes, A., *Pure Appl. Chem*., IUPAC **Vol 75**, **No 6**, (2003) 801-858.

[32] Takele, S., PhD Thesis, *University of Witwatersrand, School of Physics,* (2001).

[33] Kaufmann, E. N., and Vianden, R. J., *Rev. Mod. Phys.*, **51**, (1979) 161.

[34] Dyar, M.D., Agresti, D.G., Schaefer, M.W., Grant, C.A. and Sklute, E.C., *Annu. Rev.Earth Planet. Sci.*, (2006) 83-95.

[35] Gunnlaugsson, H. P., Bharuth-Ram, K., Dietrich, D., Fanciulli, M., Fynbo, H. O. U. and Weyer, G., *Hyp. Int.* **169**, (2006) 1319-1323.

[36] Cadogan, J.M. and Ryan, D.H., *Mössbauer Spectroscopy* in *Handbook of Applied Solid State Spectroscopy,* ed. Vij, D.R. Springer US, (2006) 201-256.

[37] Gunnlaugsson, H. P., Lecture Notes, *Magnetism and Mössbauer spectroscopy on Mars*, *Aarhus University*, 2008.

[38] Rubin, L., and Poate, J., *The Industrial Physicist*, **Vol 9. No 3**, (2003) 12-15.

[39] Dézsi, I., *Hyp. Int.* **24-26**, (1985) 1051-1067.

[40] Wesch, W., *Nucl. Instr. and Meth.* **B 68**, (1992) 342-354.

[41] Mayer, J. W., Eriksson, L., and Davies, J. A., *Ion Implantation in Semiconductors*, Academic Press Inc., New York, (1970).

[42] Machaka, R. *Master's Dissertation*, University of Witwatersrand, School of Physics, (2006).

[43] Ziegler, J. F., *Ion Implantation Physics*, in *Handbook of Ion Implantation*, ed. by Ziegler, J. F., Chapter 1, 1–68, North Holland, (1992).

[44] Wendler, E., *Nucl. Instr. and Meth.* **B 267**, (2009) 2680-2689.

[45] Weyer, G., *Hyp. Int.* **27,** (1986) 249 – 262.

[46] Dézsi, I., *J. Radioanal. Nucl. Chem.* **Vol. 190 No. 2**, (1995) 225 – 235.

[47] Ziegler, J. SRIM & TRIM, http://www.srim.org

[48] Gao, W., and Sammes, N.M., *An Introduction to Electronic and Ionic Materials*, (1999) 84-85.

[49] Weyer, G., *Hyp. Int*. **177,** (2007) 1-13.

[50] Fedoseyev, V.N., Btitzner, K., Catherall, R., Evensen, A.H.M., Forkel-Wirthb, D., Jonsson, O.C., Kugler, E., Lettry, J., Mishin, V.I., Ravn, H.L., Weyer, G. and the ISOLDE Collaboration *Nucl. Instrum. Meth*. **B 126**, (1997) 88-91.

[51] Mantovan, R., Gunnlaugsson, H.P., Weyer, G., Sielemann, R., Naidoo, D., Bharuth-Ram, K., Olafsson, S., Langouche, G. and Johnston, K., *CERN-INTC-2006-005; INTC-P-203*.

[52] Weyer, G., *Mössbauer Effect Methodology*, ed in Gruverman, I.J., Plenum, New York, **Vol 6**, (1971).

[53] Gunnlaugsson, H.P., *Personal Communication*. (2008 and 2009).

[54] Weyer, G., Gunnlaugsson, H.P., Dietrich, M., Fanciulli, M., Bharuth-Ram, K., Sielemann, R., and the ISOLDE Collaboration., *Nucl. Instrum. Methods* B **206**, (2003) 90.

[55] Weyer, G., Burchard, A., Fanciulli, M., Fedoseyev, V.N., Gunnlaugsson, H.P., Mishin, V.I., Sielemann, R., and the ISOLDE Collaboration., *Physica* **B 273-274**, (1999) 363.

[56] Gunnlaugsson, H.P., Fanciulli, M., Dietrich, M., Bharuth-Ram, K., Sielemann, R., Weyer, G., and the ISOLDE Collaboration., *Nucl. Instrum. Methods* **B 168**, (2002) 55.

[57] Gunnlaugsson, H.P., Dietrich, M., Fanciulli, M., Bharuth-Ram, K., Sielemann, R., Weyer, G., and the ISOLDE Collaboration., *Phys. Scr.* **T101**, (2002) 82.

[58] Gunnlaugsson, H.P., Weyer, G., Christensen, N.E., Dietrich, M., Fanciulli, M., Bharuth-Ram, K., Sielemann, R., Svane, A., and the ISOLDE Collaboration., (ICDS-22), *Physica* **B 340-342**, (2004).

[59] Gunnlaugsson, H.P., Weyer, G., Dietrich, M., Fanciulli, M., Bharuth-Ram, K., Sielemann, R., and the ISOLDE Collaboration., *Appl. Phys. Lett.* **80**, (2002) 2657.

[60] Gunnlaugsson, H.P., Weyer, G., Dietrich, M., Fanciulli, M., Bharuth-Ram, K., Sielemann, and the ISOLDE Collaboration., *Physica* **B 340-342**, (2004) 537-540.

[61] Weyer, G., Gunnlaugsson, H.P., Bharuth-Ram, K., Dietrich, M., Mantovan, R., Naicker, V., Naidoo, D., and Sielemann, R., *Hyp. Int.* **158**, (2004) 417-421.

[62] Naidoo, D., Gunnlaugsson, H.P., Bharuth-Ram, K., Naicker, V., Weyer, G., Sielemann, R., Mantovan, R., Fanciulli, M., and the ISOLDE Collaboration., *Hyp. Int.* **188**, (2009) 11-17.

[63] Bharuth-Ram, K., Gunnlaugsson, H.P., Mantovan, R., Naicker, V.V., Naidoo, D., Sielemann, R., Weyer, G., Aigne, Th., and the ISOLDE Collaboration., *Hyp. Int.* **184**, (2008) 207-211.

[64] Bharuth-Ram, K., Naicker, V.V., Naidoo, D., Gunnlaugsson, H.P., Mantovan, R., Weyer, G., Dietrich, M., Butler, J.E., and the ISOLDE Collaboration., *Hyp. Int.* **179**, (2007) 17-22.

[65] Weyer, G., Gunnlaugsson, H.P., Dietrich, M., Fynbo, H., Bharuth-Ram, and the ISOLDE Collaboration., *Eur. Phys. J. Appl. Phys.* **27**, (2004) 317-320.

[66] Bharuth-Ram, K., Hartick, M., Kankeleit, E., Dorn, C., Held, P., Sielemann, R., Wende, L. *Phys. Rev.* **B 58**, (1998) 8955–8961.

[67] Mössbauer Effect Data Center http://orgs.unca.edu/medc/Resources-isotopes/Resource-Fe.html.

[68] Lannoo, M. and Bourgoin, J., *Point Defects in semiconductors Vol 1 – Theoretical Aspects*, Springer, (1981).

[69] Bishop, S.G., in *Deep Centers in Semiconductors*, ed Pantelides, S. Gordon and Breach, New York, (1985).

[70] Wahl, U., Vantomme, A., Langouche, G., Correia, J. G., Petralta, L. and The ISOLDE Collaboration, *Appl. Phys. Lett.*, **Vol 78**, **No. 21**, (2001) 3217-3219.

[71] Cesca, T., Verna, A., Mattei, G., Gasparotto, A., Fraboni, B., Impellizzeri, G., Priolo, F., Tarricone, L. and Longo, M. *Physics of Semiconductors, 28th International Conference*, ed. Jantsch, W. and Schäffler, F.

[72] Longeaud, C., Kleider, J. P., Kaminski, P., Kozlowski, R., Pawlowski, M. and Cwirko, J., *Semicond. Sci. Technol.* **14**., (1999) 747-756.

[73] Forkel-Wirth, D., *Phil. Trans. R. Soc. Lond.* **A 356**, (1998) 2137-2162.

[74] Wichert, Th. *Hyp. Int.* **97/98**, (1996) 135-170.

[75] Wichert, T., *Physica* **B 326**, (2003) 105-112.

[76] Wahl, U., *Hyp. Int.* **129**, (2000) 349-370.

[77] Hofsass, H. and Linder, G. *Phys. Rep.* **201,** (1991) 121-182.

Wits, Johannesburg
March 2010